Investigation of the excitonic properties of hybrid and fully inorganic perovskite using magneto-spectroscopy

Zhuo Yang

Université de Toulouse

THÈSE

En vue de l'obtention du

DOCTORAT DE L'UNIVERSITÉ DE TOULOUSE

Délivré par : *l'Institut National des Sciences Appliquées de Toulouse (INSA de Toulouse)*

Présentée et soutenue le *30 Mars 2018* **par :**

Zhuo YANG

Investigation of the excitonic properties of hybrid and fully inorganic perovskite using magneto-spectroscopy

-

Étude des propriétés excitoniques de la perovskite hybride et entièrement inorganique par magnéto-spectroscopie

---

JURY

Adnen MLAYAH	Professor	Président du Jury
Tom J. SAVENIJE	Assistant professor	Membre du Jury
Lukasz KLOPOTOWSKI	Assistant professor	Membre du Jury
Mark-Oliver GOERBIG	Directeur de Recherche	Membre du Jury
Paulina PLOCHOCKA	Directeur de Recherche	Membre du Jury
Duncan MAUDE	Directeur de Recherche	Membre du Jury

École doctorale et spécialité :
SDM : Nano-physique, nano-composants, nano-mesures - COP 00

Unité de Recherche :
Laboratoire National des Champs Magnétiques Intenses (UPR 3228)

Directeur(s) de Thèse :
Paulina PLOCHOCKA et *Duncan MAUDE*

Rapporteurs :
Mark-Oliver GOERBIG et *Tom J. SAVENIJE*

THÈSE

En vue de l'obtention du

DOCTORAT DE L'UNIVERSITÉ DE TOULOUSE

délivré par Institut national des sciences appliquées de Toulouse
Spécialité : Nano physique

Présentée et soutenue par
Zhuo YANG

Investigation of the excitonic properties of hybrid and fully inorganic perovskite using magneto-spectroscopy

---

Ecole doctorale : Science de la Matière
Unité de recherche : Laboratoire National des Champs Magnétiques Intenses
Directeurs de Thèse : Paulina PLOCHOCKA et Duncan MAUDE

Investigation of the excitonic properties of hybrid and fully inorganic perovskite using magneto-spectroscopy

Abstract: In recent years, hybrid organic-inorganic perovskite materials have been employed as a light harvesters due to their excellent optical and electronic properties, such as broad band absorption, long diffusion length, and long carrier lifetime. The photon conversion efficiency of hybrid perovskite based solar cells has increased from 6.9% to 23.6% within the last few years. Moreover, compared to traditional photovoltaic materials (e.g. GaAs, Si), the hybrid perovskite materials are inexpensive and easy to synthesize.

The aim of this thesis is to investigate the optical and electronic properties of perovskite materials using magneto-optical techniques. We have investigated the relationship between the excitonic properties and the microstructure of hybrid perovskites. We have performed magneto-transmission measurement on $MAPbI_3$ polycrystalline thin films and magneto-reflectivity measurement on a $MAPbI_3$ single crystal. We find that, at low temperature, the exciton binding energy and reduced mass are the same for all $MAPbI_3$ samples with a variety of crystal grain sizes. To generalize our finding for $MAPbI_3$ to other perovskite compositions, we also performed magneto transmission measurement on state of the art triple cation perovskites $Cs_{0.05}(MA_{0.17}FA_{0.83})_{0.95}Pb(I_{0.83}Br_{0.17})_3$ polycrystalline thin films with two considerably different crystal grain sizes. The reduced mass and binding energy of excitons in these two samples are identical. Thus, we conclude that the microstructure plays a negligible role in the exciton properties of hybrid perovskites, regardless of the thin film deposition technique and final morphology.

Finally, we have investigated the electronic properties of the fully inorganic perovskites, namely $CsPbX_3$ compounds (X = I or Br or a mixture of those). We have performed temperature dependent transmission and magneto transmission measurements on a range of $CsPbX_3$ compounds. The temperature dependent measurement of all the Cs based perovskites shows a continuous increase of the band gap energy with the increasing temperature, indicating that $CsPbX_3$ does not undergo a structural phase transition in the temperature range from 4 K to 270 K. By performing the magneto-transmission measurement on $CsPbX_3$, we have determined the exciton binding energies and reduced mass with high accuracy. A comparison of the values of dielectric constant for the fully inorganic and the hybrid organic-inorganic perovskites indicates that, at low temperature when the organic cations are frozen, the dominant contribution to the dielectric screening is related to the relative motion within the lead halide cage.

Keywords: hybrid perovskites, photovoltaics, phase transition, exciton binding energy, effective mass

Etudé des propriétés excitoniques de la perovskite hybride et entièrement inorganique par magnéto-spectroscopie

Abstract: Au cours des dernières années, les perovskites hybrides organiques-inorganiques ont été employées en tant qu'absorbeurs de lumière, en raison de leures excellentes propriétés optiques et électroniques, comme par exemple une absorption sur une large bande spectrale, une grande longueur de diffusion et longue durée de vie des porteurs de charge photo-excités. L'efficacité de conversion des photons des cellules solaires hybrides à base de pérovskites a augmenté de 6,9% à 23,6% au cours des dernières années. De plus, par rapport aux matériaux photovoltaïques traditionnels (comme par exemple le GaAs ou le silicium), les perovskites hybrides sont peu coûteuses et faciles à synthétiser.
Le but de cette thèse est d'étudier les propriétés optiques et électroniques des perovskites à l'aide de spectroscopie magnéto-optique. Nous avons étudié la relation entre les propriétés excitoniques et la microstructure des perovskites hybrides. Nous avons effectué des mesures de magnéto-transmission sur des couches minces polycristallines de $MAPbI_3$ et des mesures de magnéto-réflectivité sur un monocristal de $MAPbI_3$. Nous avons monté que, à basse température, l'énergie de liaison de l'exciton et sa masse réduite sont les mêmes pour tous les échantillons de $MAPbI_3$ indépendamment de la taille des cristaux. Pour généraliser nos résultats obtenus sur le $MAPbI_3$ à d'autres composés ayant une structure de perovskite, nous avons également effectué des mesures de magnétotransmission sur des pérovskites à cation triple de dernière génération, $Cs_{0,05}(MA_{0,17}FA_{0,83})_{0,95}Pb(I_{0,83}Br_{0,17})_3$, en couches minces polycristallines avec deux tailles de grains différentes. La masse réduite et l'énergie de liaison des excitons dans ces deux échantillons sont identiques. Ainsi, nous concluons que la microstructure joue un rôle négligeable dans les propriétés excitoniques des pérovskites hybrides, indépendamment de la technique de dépôt de la couche mince et de la morphologie finale.
Enfin, nous avons étudié les propriétés électroniques des pérovskites entièrement inorganiques, à savoir les composés $CsPbX_3$ (X = I ou Br ou un mélange de ceux-ci). Nous avons effectué des mesures de transmission en fonction de la température et de magnétotransmission sur une gamme de composés $CsPbX_3$. Les mesures en fonction de la température de toutes les pérovskites à base de Cs montre une augmentation monotonique de l'énergie de bande interdite avec la température, ce qui indique que ces composés ne subissent pas de transition de phase structurale dans la plage de température de 4 K à 270 K. En effectuant des mesures de magnéto-transmission sur $CsPbX_3$, nous avons déterminé les énergies de liaison de l'exciton et la masse réduite avec une grande précision. Une comparaison des valeurs de constante diélectrique des pérovskites inorganiques et inorganiques montre que, à basse température lorsque les mouvements des cations organiques sont interdits, la contribution dominante à l'écrantage diélectrique est liée au mouvement relatif dans la cage à base de halogénures de plomb.

Mots-clés: perovskites hybrides, photovoltaïque, transition de phase, én-

ergie de liaison de l'exciton, masse effective

Acknowledgements

First of all, I would like to express my gratitude to my supervisors Paulina Plochocka and Duncan Maude, for their guiding and patience during my PhD research. Their serious attitude toward science strongly influences me. Their sense of humor makes a comfortable atmosphere for the work in the lab. I would also like to thank the members of the jury for their valuable comments on this research.

I would also like to acknowledge all my amiable collaborators, Robin J. Nicolas and Rebecca J. Sutton (University of Oxford), Sam Stranks and Baodan Zhao (University of Cambridge), Arman M. Soufiani (University of New South Wales), Anna Fontcuberta i Morral and Gozde Tutuncuoglu (École Polytechnique Fédérale de Lausanne), Lukasz Klopotowski (Polish Academy of Sciences), for their excellent experimental work and enjoyable discussion. A special thank to Sam Stranks for hosting me one month in Cavendish Laboratory, the University of Cambridge.

I would also like to thank my colleagues in the Laboratoire National des Champs Magnétiques Intenses (LNCMI-Toulouse), who were always very kind and helpful. As older scientific brothers, Anatolie Mitioglu, Atsuhiko Miyata, Alessandro Surrente, Michal Baranowski and Krzysztof Galkowski help me a lot with solving the problems in experiments, data analysis and paper writing. Thank to Joanna Urban, Armelle Poux, Florian Vigneau for helping me deal with French administrative work. Thank to Nan Zhang for cooking delicious dinners so many times. A special thank to Nicolas Bruyant, Sylvie George and Marc Nardone for their kind help with the probe, synchronization system and cryostat. I would also like to acknowledge, the director and deputy director of the LNCMI, Geert Rikken and Oliver Portugall.

My acknowledgements are extended to my parents, who created a comfortable circumstance for my study, and always encourage me to chase my dream. I would also like to thank my friends in Toulouse, Rui Wang, Yu Zheng, Ming Yang and my girlfriend Yanian Zou, for the nice moments we had together outside of the lab.

A great thank to China Scholarship Council for awarding a 42 months scholarship, which allows me to pursue my study in France as a PhD student.

Zhuo Yang
Toulouse, April 2018

Contents

Chapter 1

Introduction

Contents

1.1 Perovskite structure

Perovskites form a wide class of materials having the same crystal structure as calcium titanate ($CaTiO_3$), named after the Russian mineralogist Lev Perovski in 1839 [Wenk 2016]. Perovskites are interesting for their flexibility of chemical substitution and have a wide range of industrial applications. For example, $BaTiO_3$ is a well recognized material for applications in ferroelectrics [Megaw 1945], $YBa_2Cu_3O_7$ opened a new approach to high-temperature superconductivity [Wu 1987], and

$Ba(Zn_{1/3}Ta_{2/3})O_3$, with a high dielectric constant, is widely used as frequency filters in wireless communications [Tamura 1986].

The general chemical formula of a perovskite structure is ABX_3. The unit cell consists of a large cation A, a small cation B and three anions X. A schematic view of the unit cell of a perovskite structure in the cubic phase is presented in Fig. 1.1(a). The A cation sits at the corner positions, the B cation is located at the body center, and the X anions are located at the center of the cubic face. In a perovskite structure, one B cation and six X anions form an octahedra (BX_6 octahedra), where the B cation is located at the center of the octahedra and X anions are located at the corners around the B cation (6-fold coordination). In fact, the perovskite structure can be described as follows, the BX_6 octahedra forms a three dimensional network by connecting all the corners, while the A cations fill the holes among the octahedra (12-fold coordination), as shown in Fig. 1.1(b).

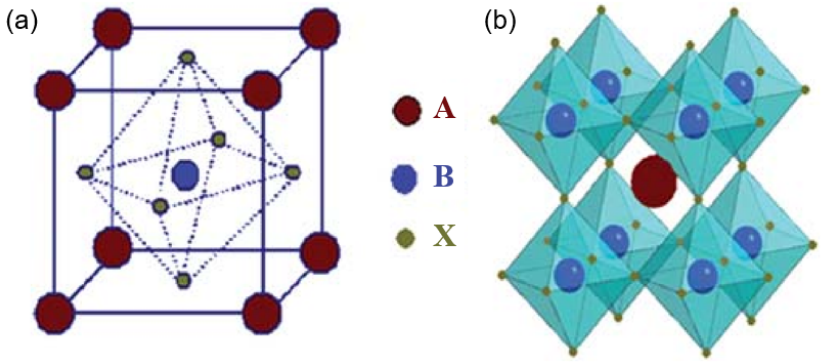

Figure 1.1: (a) Perovskite structure with the chemical formula ABX_3. (b) the extended network structure connected by BX_6 octahedra. Red, blue, green spheres represent the A, B cations and X anion. Figure reprinted after reference [Cheng 2010].

1.1.1 Tolerance factor

The ideal cubic perovskite structure is quite rare and can be found only in a few compounds, such as $CaRbF_3$ or $SrTiO_3$ [Johnsson 2007]. In an ideal cubic perovskite structure, the length of the unit cell (a) is related to the ionic radii by:

$$a = \sqrt{2}(r_A + r_X) = 2(r_B + r_X), \tag{1.1}$$

where r_A, r_B and r_X are the ionic radii of the A, B cations and the X anion.

For the majority of perovskite compounds, the ionic radii of the A and B cations and the X anion do not fulfill Eq. 1.1. In this case, the BX_6 octahedron are distorted (tilted or rotated), and the symmetry of the crystal is lower than the ideal cubic structure. In order to describe the degree of the distortion, Goldschmidt's tolerance factor t is introduced:

$$t = \frac{r_A + r_X}{\sqrt{2}(r_B + r_X)}, \tag{1.2}$$

Due to the different degrees of distortion, perovskite structures can be loosely classified in the following way: (i) Orthorhombic, with the highest distortion and lowest symmetry, characterized by a tolerance factor $t < 0.87$. (e.g. $CaTiO_3$, $GdFeO_3$) [Johnsson 2007, Sachdev 2006]. (ii) Tetragonal, with less distortion and a higher tolerance factor being in the range of $0.81 < t < 0.87$. (iii) Cubic, which is expected to be stable in the range of $0.89 < t \leq 1$ (e.g. $SrTiO_3$, $BaTiO_3$) [Buttner 1992, Johnsson 2007], and (iv) Hexagonal, which occurs for $t > 1$ (e.g $BaNiO_3$) [Johnsson 2007]. Since the tolerance factor mainly considers the ionic bonds, such a classification of the perovskite structure using this parameter alone is only a rough approximation.

1.2 Hybrid perovskite

In recent years, a large family of the hybrid organic-inorganic perovskites have gained considerable attention due to their potential applications, for example light-emitting diodes (LED) [Cho 2015], lasers [Xing 2014] and perhaps most importantly, high efficiency photovoltaic devices [Kojima 2009, Liu 2013].

Hybrid organic-inorganic perovskites are formed when the inorganic A cation is replaced by an organic one. Due to the limited space between the inorganic octahedra, only small organic cations, consisting of three or less C-C or C-N bonds, can fit inside the perovskite structure. The most common organic A cations are Methylammonium (MA: $CH_3NH_3^+$) or Formamidinium (FA: $CH(NH_2)_2^+$). The B cations are usually Pb^{2+} or Sn^{2+}, while X anions come from the group VII halides (Br^-, Cl^-, I^-, or a mixed composition of those).

It has been suggested, that hybrid perovskites have a strong self-assembling character during the crystal formation; (i) the inorganic ions are favorable to form the octahedral network, and (ii) the organic molecules are favorable to occupy the vacancies between the octahedra [Cheng 2010]. This character make this kind of materials easy to synthesize through a variety of fabrication methods, such as sequential deposition [Burschka 2013], solution-processed [Yang 2015b], vapor-assisted deposition [Chen 2013], and vacuum evaporation techniques [Liu 2013].

Another property of the hybrid perovskites is that it is relatively easy to substitute A, B cations or halide ions by other elements. Using chemical substitution, one can tune the band gap energy over a wide range from 1.1 eV to 3.1 eV [Suarez 2014, Hoke 2015, Zhao 2017], which covers the entire visible, and part of the near infrared range of the spectrum.

In addition to the properties described above, hybrid perovskites are also characterized by their strong broad band absorption, long diffusion length [Dong 2015] and long carrier life time [Stranks 2013]. All these properties make hybrid perovskite very promising as light harvesters for low-cost and high-efficiency solar cells. $MAPbI_3$, as a prototype of this family, was first used as an active layer in the solar cell devices in 2009 [Kojima 2009].

1.2.1 Tuning the band gap

The band gap of the perovskites can be easily tuned by chemical substitution. In hybrid perovskite material, the conduction band minimum (CBM) and valence

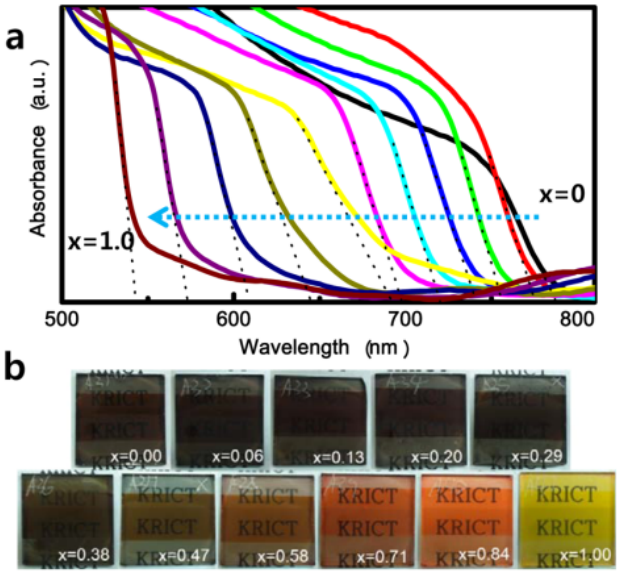

Figure 1.2: (a) UV-visible absorption spectra of $MAPb(I_{1-x}Br_x)_3$ measured with an integral sphere. (b) Photographs of $MAPb(I_{1-x}Br_x)_3$ deposited on glass substrate. After [Noh 2013].

band maximum (VBM) are mainly made up from the p or s orbital of the B cation and X anions. The organic cations mainly contribute to the flat bands in the band structure, which are far from the CBM and VBM [Borriello 2008, Jin 2012]. Thus, the inorganic octahedra cage play an essential role in determining the band gap energy. Although the organic cation does not directly contribute to the band gap, their steric effect (size and symmetry) influences the inorganic octahedra, and therefore influences the band gap [Katan 2015, Amat 2014].

1.2.1.1 Influence of the halide ions

By mixing the composition of the halogen atoms in $MAPbX_3$, it has been shown that the bandgap can be tuned to cover the entire visible spectral range [Noh 2013, Hoke 2015, Huang 2014]. For example, at room temperature, $MAPbI_3$ has a bandgap $E_g \approx 1.6\,\text{eV}$, while $MAPbBr_3$ has a bandgap $E_g \approx 2.2\,\text{eV}$ [Hoke 2015]. Using a mixture of the I and Br atoms gives a tunable bandgap from 1.6 eV to 2.2 eV, which is shown in Fig. 1.2 [Noh 2013]. Panel (a) shows the UV-visible absorption spectra of $MAPb(I_{1-x}Br_x)_3$ for the pure tri-iodide, via mixed iodide and bromide, to pure tri-bromide. With the increasing bromide compositions, the absorption energies of $MAPb(I_{1-x}Br_x)_3$ shift toward higher energy. Panel (b) shows photographs of the $MAPb(I_{1-x}Br_x)_3$ with 11 different halide compositions. With

increasing bromine composition, the color of the $MAPb(I_{1-x}Br_x)_3$ changes from a dark brown ($MAPbI_3$) to a light yellow ($MAPbBr_3$), which simply reflects the change of the band gap. By incorporating lighter chlorine ions, it is even possible to tune the band gap to the UV range ($E_g \approx 3.1$ eV for $MAPbCl_3$) [Suarez 2014]. Similar phenomenon of band gap tuning by changing the halide composition are observed for FA based perovskite compounds [Eperon 2014].

1.2.1.2 Influence of the B cation

The band gap of $MAPbX_3$ only varies from 1.6 eV ($MAPbI_3$) to 3.1 eV ($MAPbCl_3$), corresponding to the spectra range from 540 nm to 780 nm. To extend the band gap toward the mid-infrared range, we have to modify the chemical composition of the B cations. $MASnI_3$ compound is reported to exhibit a band gap around 1.2 eV [Noel 2014]. Several reports suggest that substituting partially Pb^{2+} by Sn^{2+}

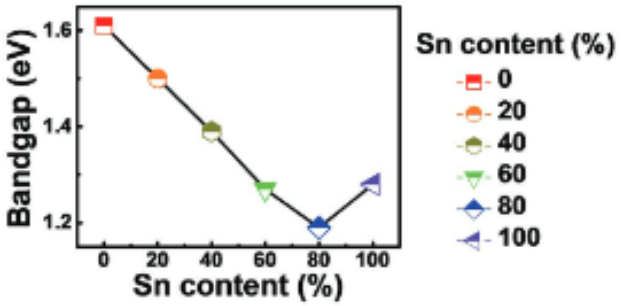

Figure 1.3: Band gap energy of $MA(Sn_xPb_{1-x})I_3$ as a function of Sn content After [Zhao 2017].

in $MAPbI_3$ can substantially change the band gap [Hao 2014a, Ke 2017, Zhao 2017]. Zhao et al. [Zhao 2017] have reported a band gap tuning for $MA(Sn_xPb_{1-x})I_3$ in the Sn composition range $0 < x < 1$. The band gap energy of $MA(Sn_xPb_{1-x})I_3$ as a function of Sn content is shown in Fig. 1.3. With higher Sn content, the band gap shifts toward lower energy. In contrast to the band gap tuning by the halide composition, which exhibits a monotonic change in the band gap, the alloy of B cation in $MA(Sn_xPb_{1-x})I_3$ shows a band gap bowing with a local minimum. The lowest band gap (1.19 eV) is obtained when Sn content reaches 80% [Zhao 2017]. Similar band gap bowing behavior is observed by Hao et al [Hao 2014b]. However, they reported a minimal band gap of $MA(Sn_xPb_{1-x})I_3$ occurs at 50% Sn composition. It is worth mentioning here that the Sn/Pb mixed perovskites are not always stable and sometimes undergo a phase separation. The difference in Sn composition for the minimum bandgap may arise from the way of the sample is prepared and the chemical composition. Various sample preparation procedures have been used. Hao et al. [Hao 2014b] first mixed MAI and MX_2 (M = Sn, Pb) in an aqueous HI/H_3PO_2 solvent at 373 K, and then slowly cool down the solution to room temperature to form the polycrystalline thin film. Zhao et al. [Zhao 2017] first prepared the pure lead and tin precursor solution. The $MA(Pb_xSn_{1-x})I_3$ perovskite was prepared by

mixing the corresponding ratio of pure lead and tin perovskite precursor solutions. In addition to the differences in the thin film preparation procedure, the chemical composition is also slightly different. Zhao et al. dissolved PbI_2 and MACl to form a pure lead precursor solution. However, this inevitably induces Cl^- in the $MA(Pb_xSn_{1-x})I_3$ perovskites. On the other hand, Hao et al. used pure I^- as the halide anions.

1.2.1.3 Influence of the organic cation

With different A-cations, hybrid perovskite exhibit a different band gap. For example, at room temperature, the band gap of $FAPbI_3$ is 1.5 eV [Eperon 2014], while the band gap of $MAPbI_3$ is 1.64 eV. Pellet et al. [Pellet 2014] demonstrated a linear dependence of the band gap with FA compositions in mixed cation $MA_xFA_{1-x}PbI_3$. Moreover, the organic cations do not directly influence the band gap. Borriello et al. [Borriello 2008] suggest that the band gap is influenced by the size of the embedded organic cation. They claim that the band gap is very sensitive to any modification of the octahedra. The effective ionic radii of FA is higher than that of MA. The size of the organic cation influences the volume, tilting angle and deformation of the inorganic cage, and therefore, influences the band gap energy [Borriello 2008].

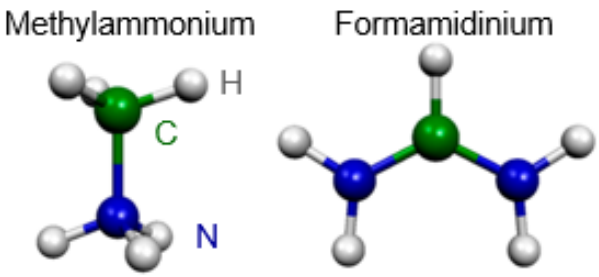

Figure 1.4: Atomic structure of methylammonium (MA) and formamidinium (FA). Figure reprinted from [Amat 2014].

In a more complete study, Amat et al. [Amat 2014] take the exact form of the structural phase and spin-orbital coupling into consideration to investigate the influence of the A-cations on the band gap. The organic cation usually has a non-spherical geometry and rotates constantly in the lattice. Fig. 1.4 shows the schematic representations of MA and FA [Amat 2014]. Compared to the MA molecule, the FA molecule has a higher number of hydrogen bonds. As a consequence, $FAPbI_3$ exhibits a trigonal/pseudocubic crystal structure at room temperature, while $MAPbI_3$ exhibits a tetragonal crystal structure [Amat 2014]. The trigonal structure amplifies the ionic character of Pb-I bonds, which enhances the Pb character of the conduction band, and thus increases the effect of spin-orbit coupling, which lower the band gap energy of $FAPbI_3$ [Amat 2014]

1.2.2 Structural phase transition

As described in Section 1.1.1, perovskite structures are classified into different phases due to the degree of distortion, namely orthorhombic, tetragonal, cubic and hexagonal structures. The classification according to the tolerance factor described in Section 1.1.1 is highly inaccurate for hybrid perovskites [Kieslich 2014, Kieslich 2014]. The tolerance factor was essentially developed for inorganic oxide perovskites, and mainly consider the ionic bonds [Li 2016]. When organic cations are incorporated into the perovskite structure, their polar character leads to an interaction between the organic cations and the inorganic cage, resulting in additional disorder [Amat 2014].

Table 1.1: Temperature dependence of the crystal structure of $MAPbX_3$ (X=Cl, Br or I). Data after the reference [Oku 2015].

Matrial	Cubic	Tetragonal	Orthorhombic
$MAPbI_3$	$> 330\,K$	$161\,K$ to $330\,K$	$< 161\,K$
$MAPbBr_3$	$> 236\,K$	$154\,K$ to $236\,K$	$< 149\,K$
$MAPbCl_3$	$> 177\,K$	$172\,K$ to $177\,K$	$< 172\,K$

The structural phase of the hybrid perovskite material depends mainly on the temperature induced distortion. At different temperatures, perovskite material exhibit a different lattice constant, degree of distortion, and thus, different structural phases. For example, $MAPbX_3$ can be in three different structural phases. When the temperature increases, they undergo structural phase transitions (second order) from orthorhombic to the tetragonal phase, and then to the cubic phase. The phase transition temperature varies for different chemical compositions. Table 1.1 summarizes the temperature dependence of the crystal structure of $MAPbX_3$.

To understand the behavior of organic cation and inorganic octahedra in different phases, we show in Fig. 1.5 the crystal structure of (a) orthorhombic, (b) tetragonal, and (c) cubic structure of $MAPbI_3$ [Brivio 2015]. $MAPbI_3$ perovskite crystals exhibit a orthorhombic phase at low temperature up to 161 K. In the orthorhombic phase, the PbI_6 octahedra are strongly deformed (as shown in Fig. 1.5(a)), which restricts the rotational degrees of freedom of MA [Motta 2015]. In this case, the organic cation is fully ordered. The ordering may be sensitive to the material preparation or cooling rate into this phase [Brivio 2015]. Around 160 K, the orthorhombic structure is transformed to the tetragonal phase. In the tetragonal structure, the MA cations are partially ordered [Whitfield 2016] and start to have the freedom to rotate. The PbI_6 octahedra are less distorted and tilted, as shown in Fig. 1.5(b). Above 330 K, $MAPbI_3$ exhibits a cubic symmetry. In the cubic phase, the MA cations are fully disordered and free to rotate between the octahedra. NMR measurements have shown that the exact location of the MA cations cannot be determined [Knop 1990].

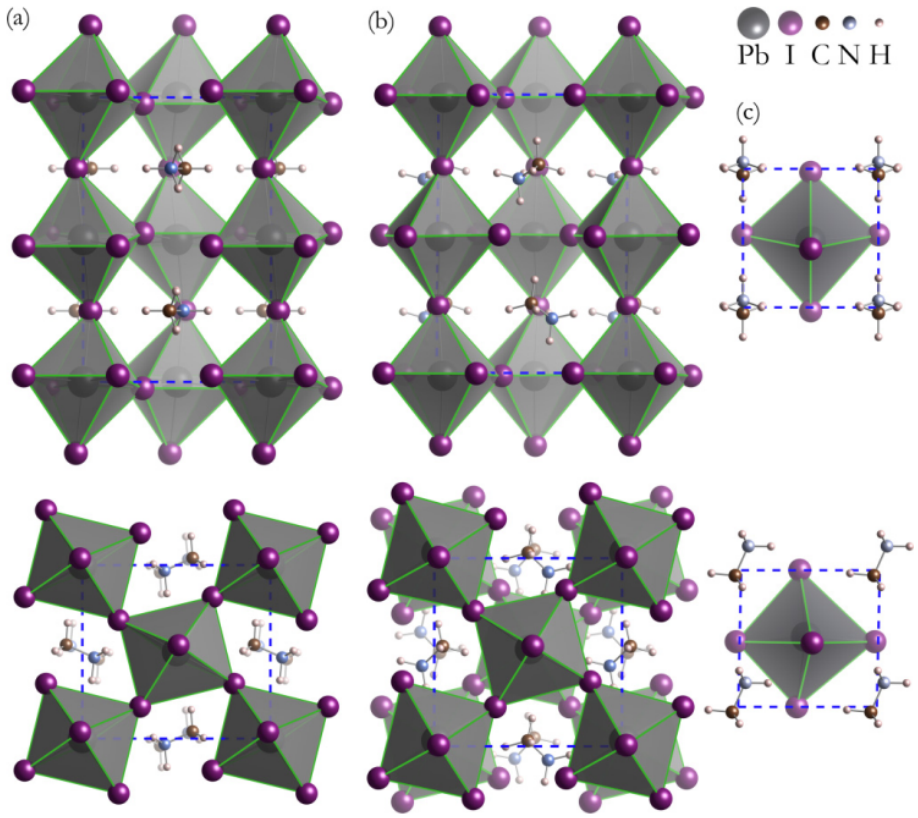

Figure 1.5: The crystal structure of (a) orthorhombic, (b) tetragonal, and (c) cubic phase of $MAPbI_3$. The upper and lower panels are oriented though <100> and <001>, respectively.The PbI_6 octahedra are shaded grey. After [Brivio 2015].

The structural phase transitions influence the electronic properties of hybrid perovskites. The most straightforward influence is the change of the band gap. Depending on the compound, the phase transition from the orthorhombic to the tetragonal phase can be accompanied by tens of meV decrease of the band gap energy [Yamada 2015, Kunugita 2015]. Another influence of the structural phase transition is the dielectric screening. In the orthorhombic phase, the organic cations are frozen and cannot rotate, while the organic cations start to move and rotate in the tetragonal phase. The movement of the organic cations increases the dielectric screening, which should result in a lower exciton binding energy in the tetragonal phase. This phenomenon was proposed by Even et al [Even 2014b, Poglitsch 1987, Onoda-Yamamuro 1992], and confirmed by the magneto-optical measurements of Miyata et al. [Miyata 2015].

In polycrystalline perovskite films, it is worth to mention that the orthorhombic/tetragonal phase transition does not happen uniformly over the whole film. It has been reported that part of the polycrystalline film remains in the tetragonal phase at temperatures even below the phase transition. Indeed, rem-

nants of the tetragonal phase can be found at temperatures as low as $T = 4\,\mathrm{K}$ [Wehrenfennig 2014, Galkowski 2017]. In addition, it is also reported that the phase transition temperature strongly depends on the size of the crystalline grains, when the crystalline grain size is below 500 nm [Li 2016].

1.2.3 Morphology

Nowadays, a variety of fabrication methods are employed to prepare the perovskite materials, such as single-step [Kim 2016], sequential deposition [Burschka 2013] or gas assisted techniques [Huang 2014]. This leads to a variety of morphologies for perovskite materials. For the polycrystalline thin films, the crystal grain size can vary from tens of nanometers to microns. With a low temperature supersaturated solution approach, it is even possible to obtain millimeter size single crystals [Dong 2015, Shi 2015]. The morphology plays a very important role in perovskite materials, since it can influence the diffusion length or carrier lifetime and in consequence the efficiency of the solar cells.

Several reports have shown that the crystal grain size play a non-negligible role for the carrier diffusion length. For example, Xiao et al. [Xiao 2014] have shown that the the carrier diffusion length in $MAPbI_3$ thin film can increase to $1\,\mu$m, when the annealing procedure enlarges the crystal grain size. Indeed, Dong et al. show that the carrier diffusion length $> 175\,\mu$m are obtained in a $MAPbI_3$ single crystal [Dong 2015].

The morphology also has an influence on the carrier life time. Due to the inhomogeneous character of the thin films, the emission does not occur uniformly over the film. Vorphl et al. [Vorpahl 2015] have demonstrated that the $MAPbI_3$(Cl) thin films are composed of dark and bright regions. A confocal PL image of a $3\,\mu$m by $3\,\mu$m region of $MAPbI_3$(Cl) is shown in Fig. 1.6(A). The image clearly demonstrate that bright and dark regions co-exist in the same film. The PL spectra from dark and bright region are shown in Fig. 1.6(B). The PL intensity from a dark region is significantly lower than that of a bright region. Fig. 1.6(C-E) shows the PL decay of the indicated dark and bright region at low, medium and high excitation fluences, respectively. The PL decay curve from the bright region clearly show a single, long decay, while the dark region show a double exponential PL decay curve, composed of a short and a long decays. This is mainly due to the fact that, compared to the bright regions, dark regions have a higher density of deep trap states, resulting in a shorter carrier life time and low PL intensity [Vorpahl 2015]. These results point out that perovskite material have significant nonradiative losses due to the inhomogeneity, which are detrimental for the overall performance of the perovskite devices. Therefore, it is essential to remove these nonradiative pathways to obtain uniform perovskite film with only bright grains.

In addition to the parameters discussed above, it was also suggested, by Grancini et al. [Grancini 2015], that the film morphology has an influence on the Coulomb interaction between the electron and holes. Analyzing the results of temperature dependent time resolved transmission spectra, they claim that the exciton binding

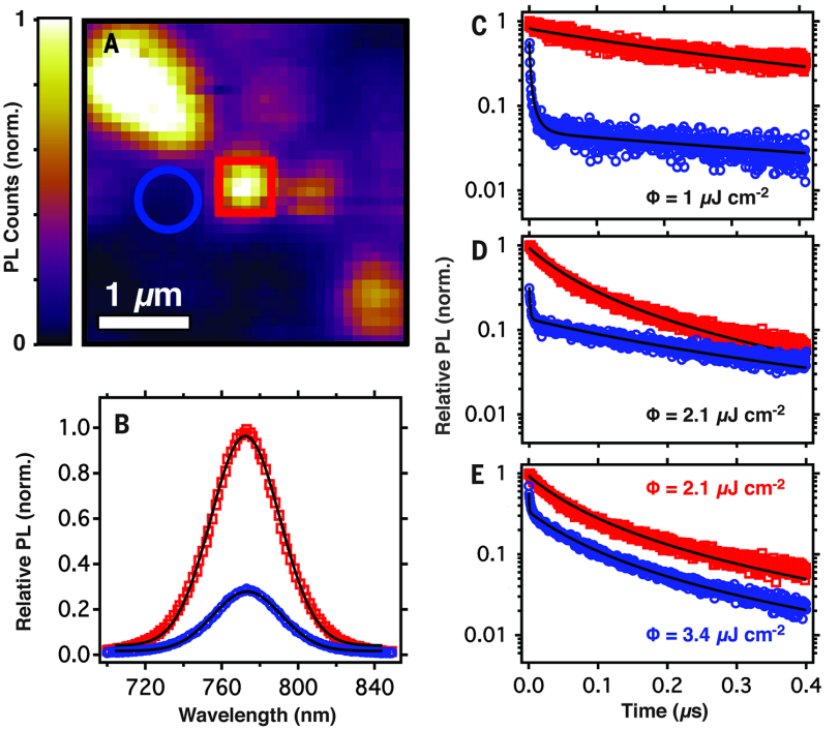

Figure 1.6: (A) A 3 μm-3 μm fluorescence image of the $MAPbI_3(Cl)$ perovskite film. (B) PL spectra of bright (red square) and dark (blue circle) regions. (C)-(E) Time -resolved PL decay curves of bright (red square) and dark (blue circle) regions, measured at indicated excitation power. After [Vorpahl 2015].

energy can vary depending upon the microstructure of the perovskite film. As we will see, the results presented in this thesis clearly demonstrate that this is not the case.

1.3 Electronic properties of hybrid perovskite

To further improve the performance of the hybrid perovskite material in solar cells, a deep understanding of the fundamental properties is important. Here, we summarize the known electronic properties of the hybrid perovskite materials.

1.3.1 Band structure

The calculation of the band structure of hybrid perovskites is mainly performed by using density functional theory (DFT) [Even 2012, Even 2013, Even 2014b]. Here, the DFT simulation of $MAPbI_3$ in the cubic phase, performed by Even et al. [Even 2015], is taken as an example to illustrate the band structure in hybrid perovskites. The cubic phase of $MAPbI_3$ has a $Pm3m$ space group symmetry, and the space group $I4/mcm$ is used to describe the tetragonal phase [Whitfield 2016].

The space group $I4/mcm$ is a subgroup of $Pm3m$, in other words, tetragonal and cubic structure obey a group-subgroup relation [Even 2015].

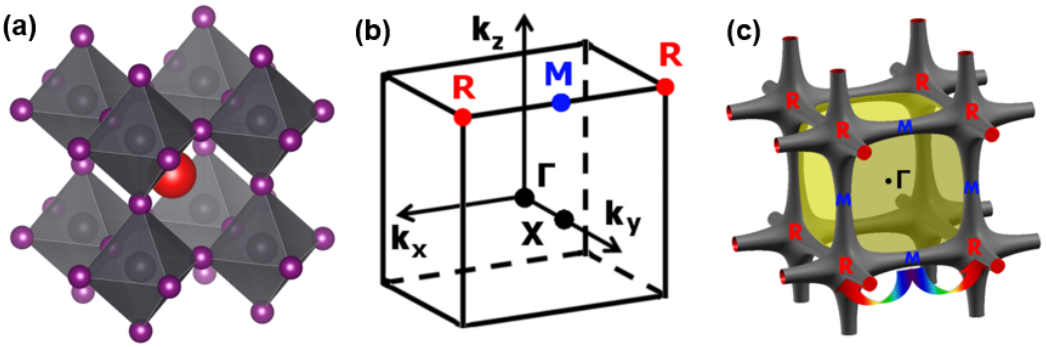

Figure 1.7: (a) Real space 3D view of cubic crystal structure of the hybrid perovksite. (b) Reciprocal-space 3D view showing the first Brillouin zone. (c) Fermi surface (E = -0.5 eV) in the first Brillouin zone. Points R and M are connected along the edges. After [Even 2015].

The ideal cubic structure in real space and corresponding first Brillouin zone of hybrid perovskites are shown in Fig. 1.7(a-b). In the Brillouin zone, we can distinguish a number of important high symmetry points: The Γ-point, which is located in the center, the X-point at the face center of the Brillouin zone boundary, the M-point at the center of the cube edge, and the R-points are vertices of the cube. Fig. 1.7(c) shows the Fermi surface (isoenergy surface below the valence band maximum at -0.5 eV) of $MAPbI_3$ in the first Brillouin zone. R and M points are connected along the edge. Here, the M points are the saddle points.

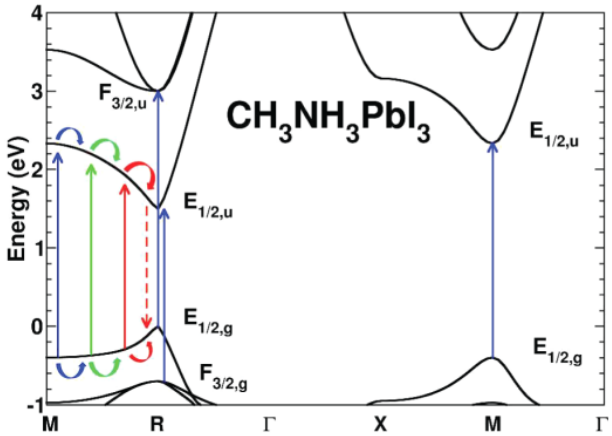

Figure 1.8: Electronic band structure for the cubic phase of $MAPbI_3$. Vertical arrows show various possible optical transitions close to the band gap energy. Optical transitions along the line between the M and R points generate carriers that easily relax toward the R point. After [Even 2015]

The calculated band structure for the cubic phase of $MAPbI_3$ is shown in Fig. 1.8. The theoretical calculation for $MAPbI_3$, based on DFT, indicates that optical absorptions are related to two high symmetry points, namely R and M [Even 2014a]. The direct band gap at the R point is the primary band gap. A second direct band gap occurs at the M point. Near the R point, various possible optical transitions are dipole allowed, as shown by vertical solid colored arrows in Fig. 1.8. The transition between $E_{1/2g}$ valence band and $E_{1/2u}$ conduction band at the M point is also optically allowed. As discussed before, the M points have a saddle-like nature. The carriers created in optical absorption process at the M point will relax towards the R point along the $R \rightarrow M$ path, as schematically shown with the colored curved arrows in Fig. 1.8. This relaxation process is assisted by acoustic phonons or coupling to collective molecular rotations [Even 2014b, Even 2015].

The ground state optical transition is predicted to be at the R point between the $E_{1/2g}$ valence band and $E_{1/2u}$ conduction band states. Several other transitions at the R point are also optical allowed. Among them, $F_{3/2g} \rightarrow E_{1/2u}$ and $E_{1/2g} \rightarrow F_{3/2u}$ are the transition with the lowest energy. One may expect that the photo-created carriers at R point are trapped in $F_{3/2u}$ and $F_{3/2g}$ states. However, due to the optical phonon assisted relaxation, the carriers further relax through the path $F_{3/2u} \rightarrow E_{1/2u}$ (holes) and $F_{3/2g} \rightarrow E_{1/2g}$ (electrons) [Even 2014b]. Thus, the hybrid perovskites are characterized by broad band absorption, due to the numerous optical allowed transitions discussed above.

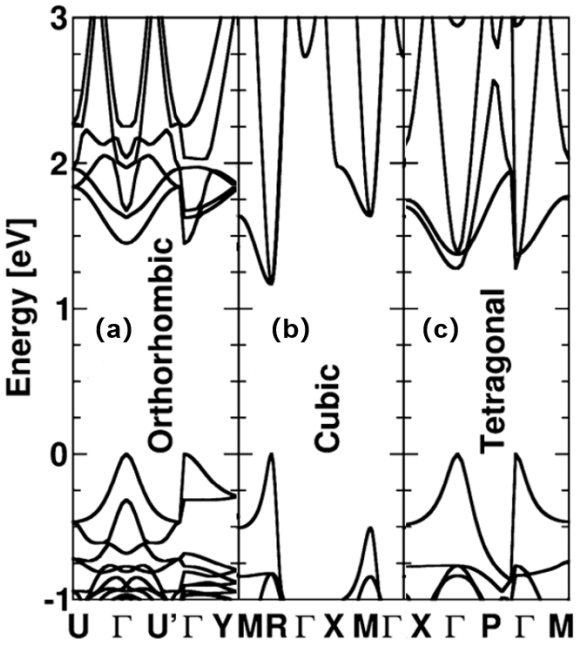

Figure 1.9: Electronic band structures for the (a) orthorhombic (b) cubic (c) tetragonal phase of $MAPbI_3$. After [Even 2015]

From high temperature to low temperature, the $MAPbI_3$ transforms from cubic

structure to tetragonal structure, then to orthorhombic structure. The electronic band structures for the orthorhombic, cubic and tetragonal phase of $MAPbI_3$ are shown in Fig. 1.9(a)-(c) [Even 2015]. In the orthorhombic and tetragonal phase, the tilts of inorganic octahedra and the reduced symmetry result in an increased band gap. Moreover, the ground state transitions are of a direct type at the Γ-point instead of R-point and M-point. The electronic states from R and M-points in the Brillouin zone of cubic structure are folded back to Γ-point in the Brillouin zone of tetragonal and orthorhombic structure. It is worth mentioning that the spin-orbital coupling effect is not taken into account in Fig. 1.9.

1.3.2 Spin-orbital coupling

In hybrid perovskites, the bandgap is dominated by a strong spin-orbit coupling (SOC) effect, particularly in the conduction band. In the band structure of hybrid perovskites, reported by Papavassiliou et al. [Papavassiliou 1994], the conduction band is constructed mainly from the *p*-orbitals of the B cations, whereas the valence band arises from the *p*-orbitals of the halide atom and the *s*-orbital of the B cations. The hybridization of the *p*-orbital of the B cations and the halide induces spin-orbit split conduction and valence bands in perovskite materials [Katan 2015].

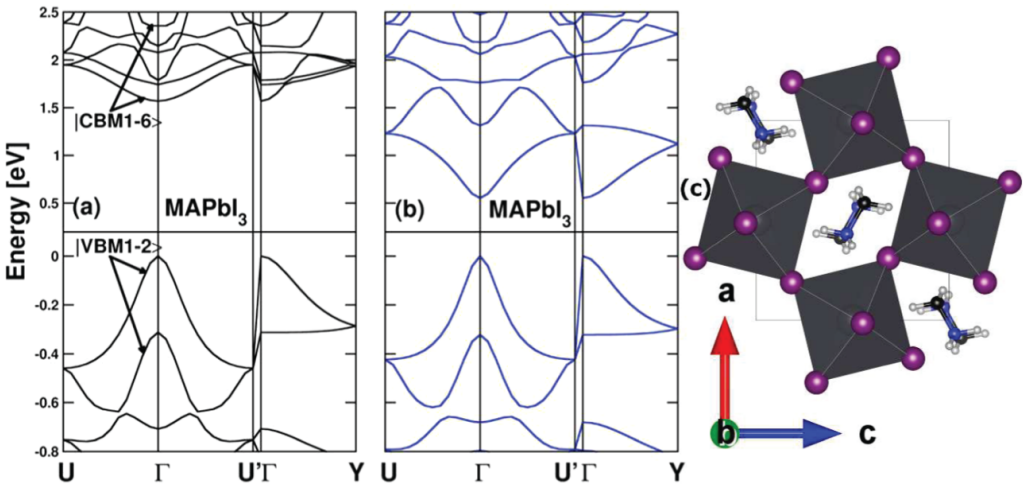

Figure 1.10: Electronic band structure of $MAPbI_3$ in the low-temperature orthorhombic phase without (a) and with (b) spin-orbit coupling interaction. The origin of the energy scale is taken at the top of the valence band. (c) Overview of the orthorhombic phase crystal structure. After [Even 2013].

The major role of the SOC is that it significantly reduces the band gap by inducing a large splitting of the lowest degenerate levels in the conduction band. As an example, Fig. 1.10(a), (b) shows the band structure of $MAPbI_3$ in the low-temperature orthorhombic phase with and without the SOC interaction [Even 2013]. As mentioned in previous section, unlike the cubic phase, the ground state transitions are of a direct type at the Γ-point for the orthorhombic phase. They mainly

involve eight active Bloch levels: two levels for the valence band maximum and six levels for the conduction band minimum. Comparing Fig. 1.10(a) and (b), it is clear that the SOC induces a large band gap correction of $MAPbI_3$, namely, the conduction band undergo a dramatic splitting, while the valence band are nearly unaffected.

Due to the SOC effect, the band gap of perovskite materials exhibits a blue shift with the increasing temperature. This is quite counterintuitive, since majority of semiconductor materials shows a red shift with the increasing temperature [Varshni 1967]. The underlying reason is that, when the temperature increases, the unit cell expand, resulting in a larger B-X distance. As a consequence, the strength of the SOC is reduced, resulting in a smaller splitting and therefore larger band gap [Katan 2015].

The optical absorption in semiconductors is mainly related to the formation of the exciton and transitions involving free carriers. The simulation based on DFT only deal with the band structure, and therefore describes only the transitions of free carriers.

1.3.3 Rashba effect

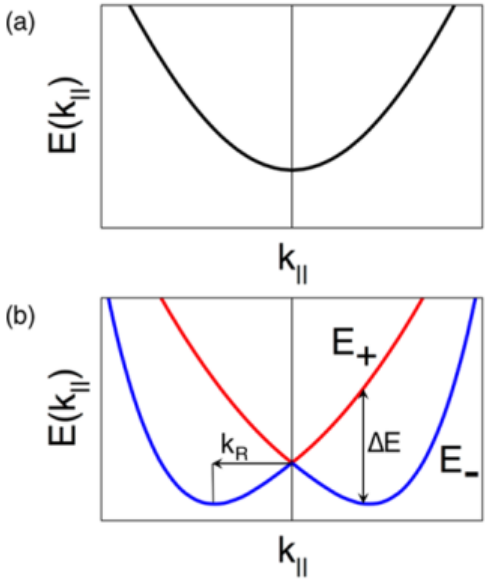

Figure 1.11: Schematic view of band dispersion in the absence of Rashba effect (a), and band dispersion including the Rashba effect. After [Kepenekian 2017]

In semiconductors, when the spin-orbit coupling effect is combined with the loss of centrosymmetry, it results in a k-dependent spin splitting of the band structure, namely, the Rashba effect. Several theoretical reports have predicted a Rashba effect in the hybrid perovskites [Even 2014b, Brivio 2014, Katan 2015]. By combining *ab initio* molecular dynamics, DFT and relativistic quasi-particle GW theory,

McKechnie et al. [McKechnie 2017] investigated the electronic band structure of $MAPbI_3$ and $CsPbI_3$. They claim that the Rashba effect may arise from the local asymmetry induced by the lead halide octahedra distortion.

The hybrid perovskites are characterized by a large density of defects at the surface or grain boundaries [Shkrob 2014]. In principle, these defects are supposed to act as a carrier trap center, which will significantly reduce the carrier life time. However, hybrid perovskites exhibit an extremely long carrier life time [Stranks 2013], which is quite surprising. The Rashba effect is proposed to be one of the explanations for the long carrier life time in the hybrid perovskites [Kepenekian 2017]. To understand the influence of Rashba effect on the carrier life time, we show in Fig. 1.11 the schematic view of band dispersion with (a) and without (b) the Rashba effect. Originally, the band is doubly degenerate, as shown in Fig. 1.11(a) [Kepenekian 2017]. When the Rashba effect is induced, the degeneracy in momentum is lifted, the original parabolic band split into two branches, as shown in Fig. 1.11(b). When the Rashba effect is observed in the valence band or the conduction band, it result in a direct to indirect band gap transition. The indirect band gap suppresses the momentum conserving carrier recombination, thus enhancing the carrier life time.

To date, the Rashba effect has only been observed in $MAPbBr_3$ single crystal by Niesner et al. using angle-resolved photo emission spectroscopy (ARPES) [Niesner 2016]. The ARPES technique only probes the surface of the sample and is mainly used to investigate the states in valence band [Dil 2009]. However, the hybrid perovskites exhibit a strong SOC in the conduction band [Even 2014b]. Moreover, to date, no other group has managed to repeat the ARPES observation of the Rashba effect. Therefore, the Rashba effect in perovskite materials is still under debate, and more detailed experimental investigations are needed.

1.4 Fully inorganic perovskite

$MAPbI_3$, although it has many advantages, has limited practical use due to its unstable character under ambient conditions. For example, it can easily dissociate into PbI_2 and MAI under environmental stress (moisture or temperature) [Wang 2016, Philippe 2015]. $FAPbI_3$ has a lower band gap than $MAPbI_3$, resulting in a higher efficiency of the solar cell devices. However, due to the large ionic radii of FA^+, $FAPbI_3$, it is favorable to form a photo-inactive phase at room temperature [Eperon 2014]. Although the photo-inactive and photo-active phase transition of $FAPbI_3$ can be reversed by annealing, the long term stability still limit the application of $FAPbI_3$ in photovoltaic devices.

To overcome the instability problems of hybrid perovskites, cesium can be incorporated to form mixed cation perovskites, which show better stability and higher efficiency. In this mixed cation perovskites, Cs^+ plays an essential role due to its smaller size. Before discussing the mixed cation perovskites, we first summarize the electronic properties and stability of $CsPbX_3$.

1.4.1 $CsPbI_3$

Of the fully inorganic perovskites, $CsPbI_3$ has received most attention due to the fact that cubic $CsPbI_3$ exhibits a band gap around 1.7 eV, which is very close to the optimal band gap energy for the top cell of tandem solar cell structure [Shah 1999]. Nevertheless, the $CsPbI_3$ compound also has stability problems, which limit its

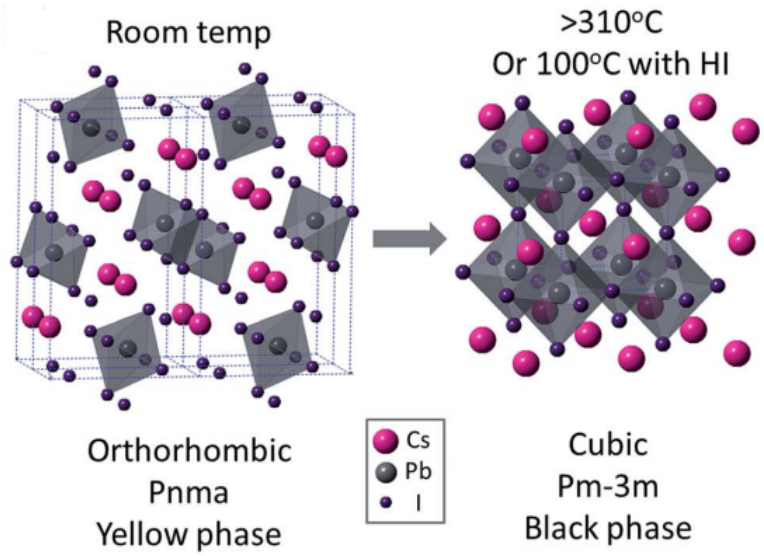

Figure 1.12: Two morphologies of $CsPbI_3$: non-perovskite "yellow" phase (left) and "black" perovskite cubic phase (right). After [Eperon 2015].

practical applications. The ionic radius of the Cs^+ cation (1.73 Å) is comparable to that of the I^- anion, which results in a rather low values of Goldschmidt's tolerance factor. The cubic structure are formed at the temperature much higher than the temperature of operational conditions. That is, in $CsPbI_3$ it is favorable to form a cubic perovskite structure above 583 K as shown in Fig. 1.12(b). The cubic phase has a black color with band gap around 1.7 eV, thus, it is also called "black" phase. At room temperature, $CsPbI_3$ compounds reveal a high level of structural distortion, with a non-perovskite, orthorhombic "yellow" phase with band gap around 2.8 eV, as shown in Fig. 1.12 [Eperon 2015]. Under ambient conditions, the black phase of $CsPbI_3$ transforms to the yellow phase almost immediately [Beal 2016].

1.4.1.1 Band structure of $CsPbI_3$

The density of states of $CsPbI_3$ shows that the origin of its band gap is largely the same as $MAPbI_3$. That is, the p-orbitals of I^- forms the valence band maximum, and the p-orbitals of Pb^{2+} forms the conduction band minimum [Brgoch 2014]. The band structure of the yellow and black phases of $CsPbI_3$ are presented in Fig. 1.13(a) and (b) [Brgoch 2014]. The red solid and the black dashed lines represent the band structure with and without the SOC effect. It is clear that SOC significantly reduces

the band gap of $CsPbI_3$, as for $MAPbI_3$. In the yellow phase of $CsPbI_3$, the PbI_6 octahedra network shows a low degree of connectivity (see Fig. 1.12(a)), leading to an extremely flat band, as shown in Fig. 1.13(a) [Brgoch 2014]. On the other hand, the band structure of the black phase $CsPbI_3$ (see Fig. 1.13) is similar to that of cubic $MAPbI_3$. The direct band gap is related to the R point. This similarity is due to the fact that the band gap of $APbI_3$ is comprised only of the states from the PbI_6 octahedra. Moreover, the black phase $CsPbI_3$ shows a higher band dispersion compared to the yellow phase $CsPbI_3$, resulting in a lower band gap [Brgoch 2014]. As discussed above, only the lower band gap of $CsPbI_3$ (black phase) is suitable for photovoltaic devices.

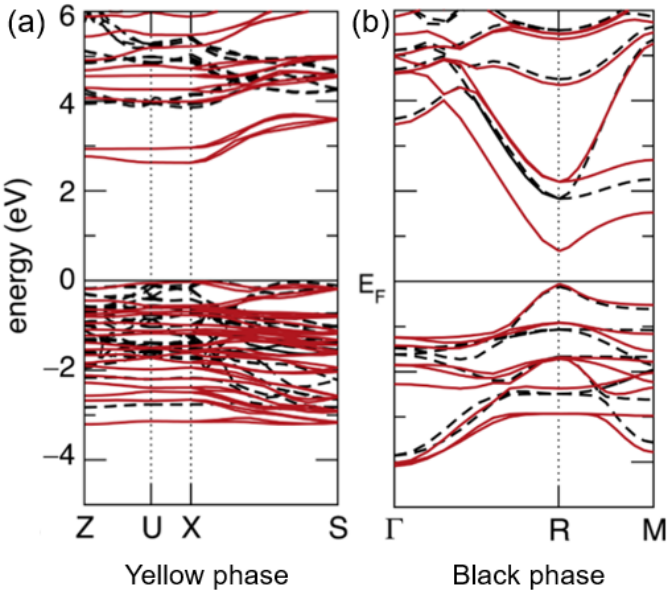

Figure 1.13: Band structure of (a) yellow and (b) black phase of $CsPbI_3$ with (red solid lines) and without (black dashed lines) SOC. Horizontal lines represent the energy level of the VBM. After [Brgoch 2014].

The main challenge of $CsPbI_3$ for applications is to maintain the black cubic perovskite phase at room temperature. Recent reports suggests that, with a large surface-to-volume ratio, the $CsPbI_3$ nanocrystals can remain in the black cubic phase under ambient conditions [Swarnkar 2016, Lai 2017, Waleed 2017]. Swarnkar et al. [Swarnkar 2016] have fabricated the $CsPbI_3$ quantum dots with size varies from 3.4 nm to 12.5 nm. Due to the quantum confinement effect, the band gap shifts toward high energy with decreasing crystal size. Notably, the $CsPbI_3$ quantum dots with ≈9 nm size remain in the cubic phase for more than 60 days [Swarnkar 2016]. Moreover, Waleed et al. and Lai et al. [Lai 2017, Waleed 2017] demonstrated that $CsPbI_3$ nanowires are also able to maintain the black cubic phase under ambient condition. The underlying reason for maintaining the black cubic phase of $CsPbI_3$ nanocrystals is still under debate. One possibility is that nanocrystals have a larger surface energy due to the high surface-volume ratio. This surface energy com-

pensates the required energy difference when going from the yellow to the black phase [Ahmad 2017]. Using $CsPbI_3$ quantum dots films as the photoative material, Swarnkar et al. fabricated a stable photovoltaic device with a photon conversion efficiency of 10.7% [Swarnkar 2016].

1.4.2 $CsPbBr_3$

$CsPbBr_3$ remains in a cubic phase at temperatures above 403 K. When the temperature is lower than 403 K, it transforms to a tetragonal phase before transforming to an orthorhombic phase at 361 K. However, all three morphologies of $CsPbBr_3$ have a perovskite structure with a similar band gap in the range of 2.3-2.4 eV [Kulbak 2015]. $MAPbBr_3$ have a similar band gap as $CsPbBr_3$ (E_g of $MAPbBr_3$: 2.32 eV). By using a variety of characterization methods, Kulbak et al. [Kulbak 2015] have shown that $CsPbBr_3$ shows a high thermal stability of the perovskite structure and enhanced device life time. Despite these advantages, $CsPbBr_3$ is limited for the photovoltaic applications due to its large band gap.

Although several approaches have been investigated to enhance the phase stability for $CsPbX_3$ compounds, the long term stability still remains a problem for the photo-active phase of $CsPbX_3$ compounds. Moreover, the PCE of $CsPbX_3$ is relatively low, compare to the hybrid perovskites (to date, 11.8% with $CsPbI_2Br$ films [Chen 2017]). Thus, it is desirable to investigate a more stable perovskite material. In next section, we summarize the recent development on the mixed cation perovskite material with a higher efficiency, which exhibit higher efficiency and stability than their pure A cation counterpart.

1.5 Evolution of the mixed cation perovskite

The Goldschmidt tolerance factor is an empirical index for predicting stable crystal structures of the perovskite materials [Li 2015, Correa-Baena 2017]. We recall that a value of the tolerance factor between 0.8 and 1.0 is favorable for the cubic perovskite. Fig. 1.14 shows the correlation between the tolerance factor and the A cation of $APbI_3$ perovskite materials. The inset images show the cation structures. Only $APbI_3$ with Cs, MA, FA cations have a tolerance factor between 0.8 and 1.0, and can form a cubic structure. The size of Na, K, Rb cation is too small, and the imidazolium (IA), ethylamine (EA), guanidinium (GA) are too large for $APbI_3$ to form a cubic structure. Although $CsPbI_3$ and $FAPbI_3$ can form a cubic structure (cubic $FAPbI_3$ above 333 K [Eperon 2014], cubic $CsPbI_3$ above 583 K [Eperon 2015]), they favor the formation of a photoinactive polymorph at room temperature, which limit the their application for the photovoltaic devices. $MAPbI_3$ degrades easily in the presence of moisture or at high temperature. In general, even when these materials are incorporated into a full solar cell architecture, they degrade within days to weeks [Leijtens 2015].

As discussed above, the pure perovskite compounds suitable for PV applications exhibit a variety of instability problems. It has been suggested that sub-

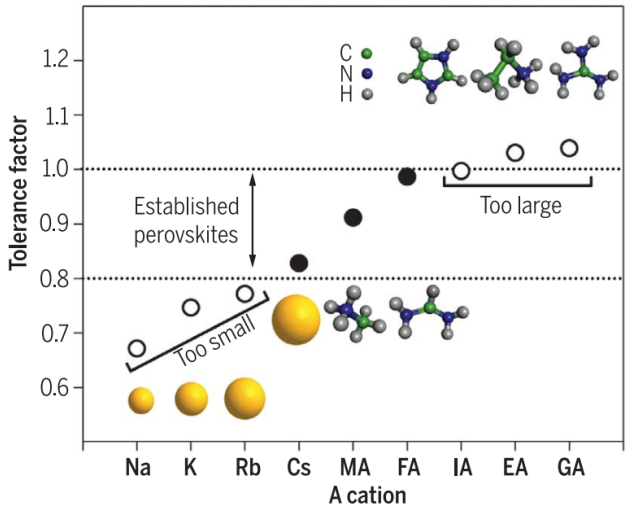

Figure 1.14: Tolerance factor of $APbI_3$ perovskites as a function of A cations. The perovskites with a tolerance factor between 0.8 and 1.0 show a photo-active cubic phase (solid circles). The cation structures are depicted in the inset images. After [Correa-Baena 2017]

stituting a small amount of I^- by Br^- is highly beneficial for the stability of mixed halide perovskites [Jacobsson 2016]. However, when large amount of Br^- (about 50%) are incorporated in the mixed halide perovskites, it results in a partial phase segregation, leading to the formation of a small amount of an iodine rich phase [Correa-Baena 2017]. This iodine rich phase has a lower band gap and acts as an efficient recombination center, which is detrimental for the device performance [Jacobsson 2016].

Since solid-state alloying is a common tool for tailoring the optical absorption and chemical stability of perovskite material, one way to solve these stability problems is to mix FA based perovskite compounds with some smaller A-cations (MA, Cs or Rb) to reduce the tolerance factor.

1.5.1 Mixed cation compounds in single junction solar cells

Since different solar cell structure have different requirements for the band gaps, we divide the discussion of the evolution of mixed cation perovskite material into two parts, according to the solar cell structure. In this section, we discuss the recent achievement (stability, efficient et al.) using mixed cation perovskites in the single junction solar cells.

$(FAPbI_3)_{1-x}(MAPbBr_3)_x$. It has been reported that mixing $FAPbI_3$ with $MAPbBr_3$ can enhance the stability of the photo-active perovskite phase of $FAPbI_3$. The PCE and structural stability of $(FAPbI_3)_{1-x}(MAPbBr_3)_x$ has been investigated with the ratio x ranging from 0 to 0.3 [Jeon 2015]. In this work, $(FAPbI_3)_{0.87}(MAPbBr_3)_{0.13}$, with a PCE of 18%, was reported to be the optimal

composition for the stabilization of the photo-active perovskite phase [Jeon 2015, Baena 2015]. Moreover, $(FAPbI_3)_{1-x}(MAPbBr_3)_x$ compounds exhibit improved crystal morphology comparing to $FAPbI_3$, revealed in smoother surface with reduced voids between the grain boundaries [Jeon 2015] .

$Cs_{0.05}(FA_{0.83}MA_{0.17})_{0.95}Pb(I_{0.83}Br_{0.17})_3$. Although the perovskite materials with MA/FA mixed cation exhibit a higher stability than $FAPbX_3$ in the photoative phase, the presence of MA does not prevent this MA/FA mixed cation material from turning into the yellow phase occasionally [Pellet 2014]. Saliba et al. have started to investigate triple Cs/MA/FA cation mixture, where Cs is used to improve the stability of MA/FA perovskite compounds [Saliba 2016b]. They found that a small amount of Cs is sufficient to effectively suppress the yellow phase and induces highly uniform perovskite grains. $Cs_x(FA_{0.83}MA_{0.17})_{1-x}Pb(I_{0.83}Br_{0.17})_3$ with cesium content at $x = 0.05$ is proposed to be the optimal composition. The perovskite solar cells using this compounds have a PCE as high as 21.1% and an output at 18% under operational condition after 250 hours.

RbCsMAFA compounds. The ionic radii of Rb^+ is slightly smaller than Cs^+, resulting in a lower tolerance factor for $RbPbI_3$ than $CsPbI_3$. The $RbPbI_3$ cannot form a black perovskite phase at any temperature [Saliba 2016a]. However, Saliba et al. has demonstrated that the incorporation of Rb cations in the triple cation perovskite can significantly improve the solar cell performance [Saliba 2016a]. The RbCsMAFA compound based devices have a PCE up to 21.6% on small areas (average value: 20.2%) [Saliba 2016a]. By adjusting the halide composition, the RbCsMAFA compound based devices can reach a PCE of 22.1% (highest PCE to date) [Yang 2017a]. In addition, compounds incorporating Rb also exhibit better stability. After 500 hours at 358 K under the continuous illumination, the PCE of the devices only decreases by 5%.

1.5.2 Mixed cation compounds in Si/perovskite tandem solar cells

Due to the Shockley-Queisser limit, traditional single junction solar cells have a maximum theoretical efficiency of 30% [Shockley 1961]. To overcome this limitation, multi junction solar cells are used. Theoretically, an infinite number of junctions with different band gaps would have a limiting efficiency of 86.8% under highly concentrated sunlight [Green 2001]. Recently, the concept of perovskite based tandem solar cells was proposed to fully exploit the excellent absorption properties of perovskite materials [Bailie 2015, Sivaram 2015]. The tandem architecture is a two junction solar cell, which is composed of a rear subcell, and a front subcell. A schematic view of tandem solar cell architecture is represented in Fig. 1.15. The rear subcell has a narrow band gap, to absorb the low energy range of the solar spectrum, while front subcell has a wide band gap, to absorb the high energy range of the solar spectrum.

The perovskite based tandem solar cells are mainly divided into two types, namely, Si/perovskite and perovskite/perovskite. In this section, we first discuss the Si/perovskite tandem solar cell. In this kind of tandem solar cell, the front

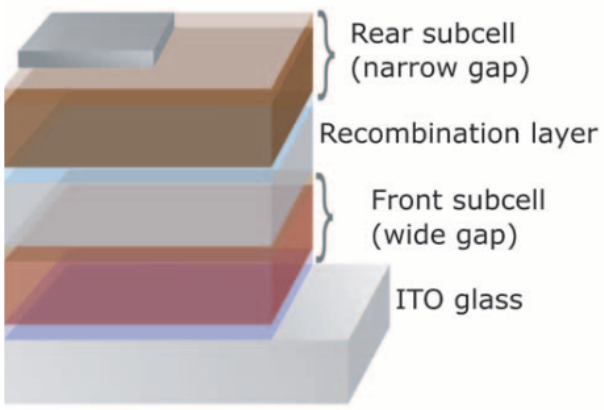

Figure 1.15: Schematics view of two-terminal and four-terminal tandem solar cell structure. After [Eperon 2016].

subcell is made of perovskite material, while the rear subcell is made by silicon with a band gap of 1.1 eV [Sivaram 2015]. The optimal band gap energy of front subcell is proposed to be 1.75 eV [Shah 1999].

It is possible to tune the band gap by changing the halide composition of $FAPb(I_{1-x}Br_x)_3$ or $MAPb(I_{1-x}Br_x)_3$. $FAPb(I_{1-x}Br_x)_3$ compounds have a problem with a photo-inactive phase, while, for $MAPb(I_{1-x}Br_x)_3$, soaking it with light induces a halide segregation within the perovskite [Hoke 2015]. To fulfill the requirements of band gap tuning and stability, Cs/FA based perovskite compounds have been developed [McMeekin 2016, Beal 2016, Lee 2015]. McMeekin et al. [McMeekin 2016] have reported a mixed cation perovskite with composition of $CsFAPb(I_xBr_{1-x})_3$. They have shown that partially substituting the FA cation with Cs leads to the result that the phase instability was entirely eliminated in the iodide to bromide compositional range. Moreover, by tuning the composition of alloyed Cs and Br, it is possible to obtain a perovskite material with an optical band gap around 1.74 eV. The optimal composition is reported to be $Cs_{0.17}FA_{0.83}Pb(I_{0.6}Br_{0.4})_3$ [McMeekin 2016]. Based on this building block, Bush et al. [Bush 2017] reported Si/perovskite tandems with a PCE up to 23.6% by optimizing the interfaces and the band gap of the top cell.

1.5.3 Mixed cation compounds in perovskite/perovskite tandem solar cells

As mentioned above, another strategy for the perovskite tandem solar cells is to use perovskite/perovskite structure. As the name suggests, for the perovskite/perovskite tandem solar cells, both the front subcell and rear subcell are made of perovskite material. Eperon et al. [Eperon 2016] has fabricated monolithic tandem solar cells with two mixed cation perovskites. The SEM of the monolithic perovskite/perovskite tandem solar cell is shown in Fig. 1.16. In this structure, the top cell is made of $FA_{0.75}Cs_{0.25}Sn_{0.5}Pb_{0.5}I_3$ with a band gap around 1.2 eV,

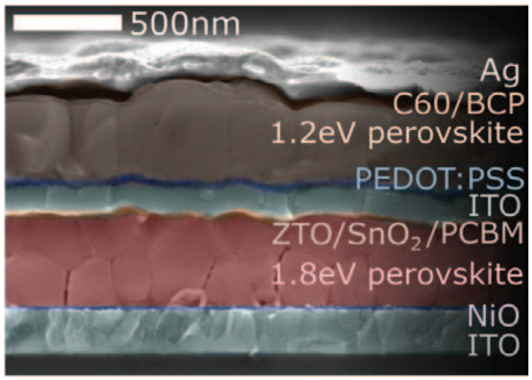

Figure 1.16: SEM of the monolithic perovskite/perovskite tandem solar cell. After [Eperon 2016].

while the bottom cell is made of $FA_{0.83}Cs_{0.17}Pb(I_{0.5}Br_{0.5})_3$ with a band gap around 1.8 eV. This solar cell exhibit a PEC of 17% with >1.65-volt open-circuit voltage [Eperon 2016]. Although the PEC of perovskite/perovskite tandem is still lower than that of the Si/perovskite tandem, this kind of architecture has the advantage of the simple bandgap tuning of perovskite absorbers and the use of inexpensive materials [Eperon 2016].

1.6 Absorption in semiconductors

In this thesis, we mainly show and discuss the results of magneto-absorption measurement on different perovskite materials. The optical absorption in semiconductors are mainly related to the formation of the excitons and the transition of free carriers. In this section, we introduce a short summary of the main features of excitons. Then, we discuss the influence of a magnetic field on the free carriers and the free excitons in the perovskite materials.

1.6.1 Excitons in semiconductors

In a semiconductor material, the absorption of a photon creates an electron in the conduction band and a hole in the valence band. With opposite charge, the electron and hole attract each other via the coulomb interaction, and form a quasi particle, known as an exciton. Excitons were predicted in 1931 by Yakov Frenkel [Frenkel 1931] and observed for the first time in 1950 by Hayashi and Katsuki in the absorption spectra of CuO_2 [Hayashi 1950].

Excitons are well described by the hydrogen atom-like model. A hydrogen atom is composed of a proton with positive charge and an electron with negative charge, which are used as an analogy for the hole and the electron in the exciton. The energy levels in hydrogen atom are described by,

$$E_n = -\frac{-me^4}{2\hbar^2 n^2} = -\frac{R_y}{n^2}, \tag{1.3}$$

where $R_y = me^4/2\hbar^2 = 13.6\,eV$ is the Rydberg constant. Here, n is the principle quantum number. R_y indicates the ionization energy of the ground state ($n = 1$) of the hydrogen atom, which is also called the binding energy. The principle quantum number is related to the radial quantum number k and azimuthal quantum number l by,

$$n = k + l + 1, \tag{1.4}$$

For each principle quantum number n, the allowed values of l are $l = 0, 1, ..., n - 2, n-1,$. The states with $l = 0, 1, 2, 3, 4, ...$ are commonly referred as $s, p, d, f, g, h, ...$ states. For instance, $1s$ denotes the state ($n = 1$, $l = 0$); 2s and 2p denote the $l = 0$ and $l = 1$ states at $n = 2$; $3s$, $3p$ and $3d$ denote the $l = 0, 1, 2$ states at $n = 3$, and so on.

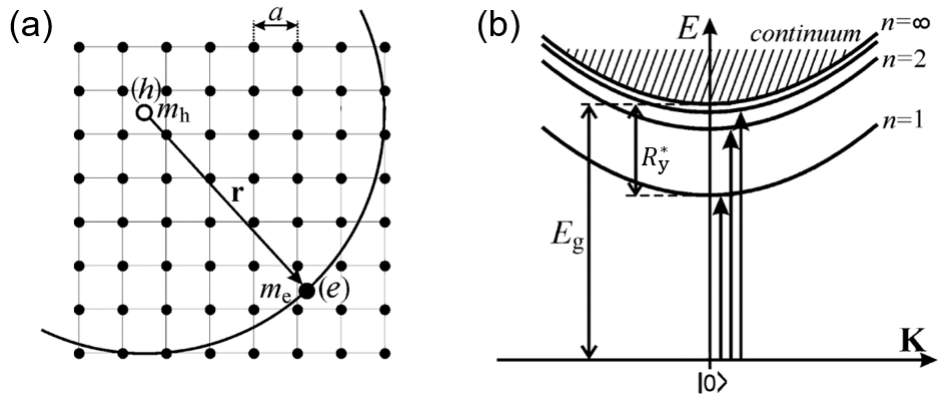

Figure 1.17: (a) Schematic of the free exciton in a two-dimensional crystal lattice with lattice constant a. (b) The energy states of a free exciton showing its bound states and the continuum states. E_g is the bandgap and Ry^* the effective binding energy. After [Pelant 2012].

One of the differences between a hydrogen atom and an exciton is the dielectric screening. For the hydrogen atom, the relative dielectric constant is $\epsilon_r = 1$. However, for the excitons in a semiconductor, the Coulomb interaction between the electron and hole pair is screened by the presence of the mobile charges in the crystal, thus the relative dielectric constant ϵ_r is larger than 1. Another differences is the reduced mass. The mass of the proton in hydrogen atoms is much higher than the mass of electron. In this case, the reduced mass of hydrogen atom is similar to the mass of a free electron. However, as the hole and electron effective masses are both smaller than the free carrier mass, the reduced mass of exciton $\mu = (1/m_e^* + 1/m_h^*)^{-1}$ is much smaller than the mass of an electron. These two differences result in a lower binding energy and larger Bohr radius for the exciton in comparison to the hydrogen atom. In this case, $R_y^* = \mu e^4/2\hbar^2\epsilon_r^2$ is the energy difference of exciton between ground states ($n = 1$) and the continuum states ($n = \infty$, free carriers), which is the effective binding energy of the exciton. Thus, the energy

levels in an exciton are given by,

$$E_n^X = -\frac{R_y^*}{n^2}, \tag{1.5}$$

In perovskites, the excitons are Wannier-Mott excitons with the electron and hole separated over many unit cells, which can move freely through the crystal. In Fig. 1.17(a), we show a schematic view of the free exciton in a two-dimensional crystal lattice. The distance between the electron and hole is several times larger than the crystal lattice constant, and is given by

$$r = n^2 a^*, \tag{1.6}$$

where $a^* = \hbar^2 \epsilon_r / \mu e^2$ is the effective Bohr radius, which denotes the distance between electron and hole in the ground state ($n = 1$). In Fig. 1.17(b), we show schematically the energy states of the exciton.

In addition to the Wannier-Mott exciton, there is another kind of excitons called Frenkel excitons. For a Frenkel exciton, the Bohr radius is approximately restricted to a single unit cell. These excitons mainly occur in molecular crystals and are localized at a specific atom or molecule [Pelant 2012].

1.6.2 Free carriers in a magnetic field

Let us consider a free carrier moving in an external magnetic field. Due to the magnetic field, a free carrier experiences a Lorentz force. The Peierl's substitution $\hat{p} \longrightarrow \hat{p} - q\hat{A}$ can be used to express the Lorentz force acting on the carrier. The Hamiltonian of the free carrier moving in a magnetic field can then be written as:

$$\hat{H} = \frac{1}{2m}(\hat{p} - q\hat{A})^2, \tag{1.7}$$

where q and m are the charge and mass of the free carrier, $\hat{p} = -i\hbar\nabla$ is the momentum operator, while $\hat{A}$ is the magnetic vector potential related to the magnetic field $\vec{B} = \nabla \times \hat{A}$. Assuming the magnetic field is applied along the z-axis, $\vec{B} = (0, 0, B)$, we choose the Landau gauge:

$$\hat{A} = \begin{bmatrix} 0 \\ Bx \\ 0 \end{bmatrix}, \tag{1.8}$$

Then, the resulting Hamiltonian is expressed as:

$$\hat{H} = \frac{\hat{p}_x^2}{2m} + \frac{1}{2m}(\hat{p}_y - qBx)^2 + \frac{\hat{p}_z^2}{2m}, \tag{1.9}$$

Considering that $\hat{H}$ is independent of the y and z coordinates component of the position operator, it commutes with the $\hat{p}_y$ and $\hat{p}_z$ operators. In other words, $\hat{p}_y$ and $\hat{p}_z$ can be replaced by their eigenvalues, resulting in:

$$\hat{H} = \frac{\hat{p}_x^2}{2m} + \frac{(\hbar k_y - qBx)^2}{2m} + \frac{\hbar^2 k_z^2}{2m}, \tag{1.10}$$

Subsequently, the Hamiltonian can be written in the form describing a harmonic oscillator along the x-axis and a free motion along the z-axis:

$$\hat{H} = \frac{\hat{p}_x^2}{2m} + \frac{m\omega_c}{2}(\hat{x} - \frac{\hbar k_y}{m\omega_c})^2 + \frac{\hbar^2 k_z^2}{2m}, \tag{1.11}$$

Here, the cyclotron frequency of the free carrier, $\omega_c = qB/m$, is introduced to simplify the expression. By solving the eigenvalue problem, we obtain:

$$E_N = \hbar\omega_c \left(N + \frac{1}{2}\right) + \frac{\hbar^2 k_z^2}{2m}, \tag{1.12}$$

where $N = 0, 1, 2, 3...$ is the orbital quantum number. $\hbar\omega_c(N + \frac{1}{2})$ presents the discrete energy levels in two dimensional plane ($x-y$ plane), while $\hbar^2 k_z^2/2m$ results from the kinetic energy dispersion along z-axis. The combination of these two leads to a density of states with van Hove singularities (the density of states diverges) at energies:

$$E_N = \hbar\omega_c \left(N + \frac{1}{2}\right), \tag{1.13}$$

where the states E_N are called Landau levels.

The movement of the carrier in semiconductors, in the presence of the magnetic field, can be described by the same formula as Eq. 1.13. The Landau levels for the holes in the valence band and the electrons in the conduction band in a semiconductor can be calculated based on Eq. 1.13, replacing m by the effective mass of the hole m_h^* and electron m_e^*, respectively.

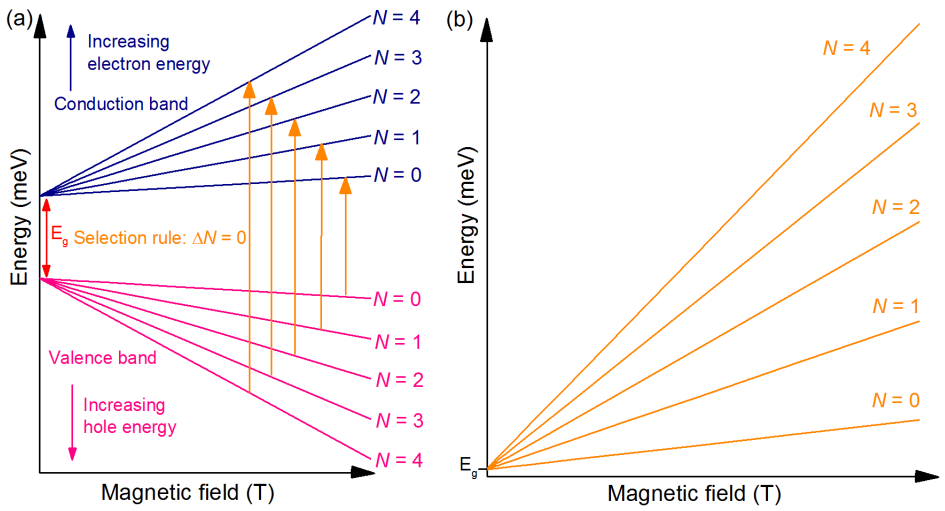

Figure 1.18: (a) Schematic figure of the Landau levels in the conduction and valence band. (b) Energy of Landau levels interband transitions as a function of magnetic filed.

A schematic view of the Landau levels for $N \leqslant 4$ in the conduction and valence bands is represented in Fig. 1.18(a). In this work, we measure the interband transitions of the electron from the Landau levels in the valence band to the conduction band, as marked by the orange arrows in Fig. 1.18(a). For perovskite material, the optical selection rule for dipole allowed transitions is $\Delta N = 0$ [Even 2012]. Using equation 1.13, the calculated energy of the interband transition is given by,

$$\Delta E_N = E_g + E_N^e + E_N^h = E_g + \hbar(\frac{qB}{m_e^*} + \frac{qB}{m_h^*})(N + \frac{1}{2}) = E_g + \hbar\omega_c^r(N + \frac{1}{2}) \quad (1.14)$$

where $\omega_c^r = qB/\mu$ with $1/\mu = 1/m_h^* + 1/m_e^*$, here μ is nothing other than the usual reduced exciton mass. Fig. 1.18(b) shows the energy of the Landau level interband transition as a function magnetic field.

1.6.3 Free excitons in a magnetic field

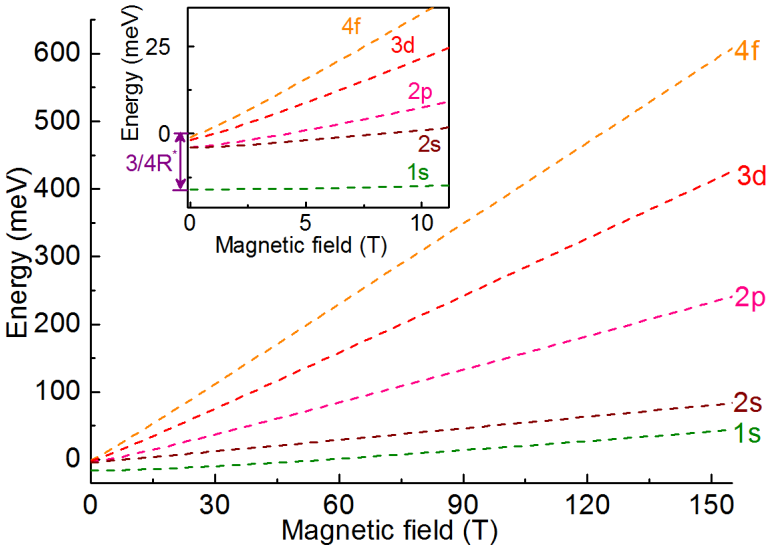

Figure 1.19: The calculated transition energies of hydrogen-like excitonic states as a function of magnetic field for $R^* = 16\,\text{meV}$ and $m^* = 0.1\,\text{m}_0$. Inset: a close-up view of excitonic transition at low magnetic field.

Compared to the Hamiltonian of the free carriers in a magnetic field, the Hamiltonian of the free excitons in magnetic field has an additional term corresponding to the Coulomb potential:

$$\hat{H} = \frac{1}{2\mu}(\hat{p}^2 - e\hat{A})^2 - \frac{e^2}{\epsilon_r \hat{r}}, \quad (1.15)$$

where $\hat{r}$ is the distance between the electron and hole. Here, by choosing the cylindrical polar coordinates (ρ, ϕ, z) and the cylindrical gauge $\hat{A} = \frac{1}{2}(\vec{B} \times \vec{r})$, the

magnetic field is along the z direction and $\vec{r} = (\rho^2 + z^2)^{1/2}$. Then the Hamiltonian can be written as:

$$\hat{H} = -\nabla^2 - \frac{2}{r} - i\gamma\frac{\partial}{\partial\phi} + \frac{1}{4}\gamma^2\rho^2, \tag{1.16}$$

where $\gamma = \hbar\omega_c/2R_y^*$ is a dimensionless parameter, indicating the ratio between cyclotron frequency ω_c and the effective binding energy R_y^*. In 1986, Makado and McGill calculated the energy eigenvalues $E_n(\gamma)$ using a numerical solution for values of γ in the range 0 to 10 and n up to 4 [Makado 1986]. $E_n(\gamma)$ are the energies of the excitonic states, given as the energy shifts with respect to the band gap energy E_g, in the effective Rydberg units.

In Fig. 1.19, we present the calculated excitonic transition energies $E_n(B)$ as a function of magnetic field using the solutions of Makado and McGill. The 1s, 2s, 2p, 3d and 4f excitonic state energies are calculated using $R^* = 16\,\text{meV}$ and $m^* = 0.1\,\text{m}_0$ with the band gap $E_g = 0\,\text{meV}$. The inset of Fig. 1.19 shows an expanded view of the excitonic transition energies at low magnetic field. It is worth to mention that, at zero magnetic field, the energy between the 1s transition and the 2s transition is three quarters of the binding energy. This follows from Eq. 1.5,

$$E_{2s}^X - E_{1s}^X = -\frac{R_y^*}{4} + R_y^* = \frac{3}{4}R_y^*, \tag{1.17}$$

Chapter 2

Experimental Techniques

Contents

This chapter presents the experimental techniques used in this thesis. A brief introduction of the pulsed magnetic field generation in LNCMI-T is followed by a detailed description of the magneto transmission and reflectivity techniques.

2.1 Magnetic field generation

Currently, the high magnetic field generation techniques for research can be divided into two categories, steady state (typical duration of several hours) and pulsed magnetic field techniques (typical duration of $\leqslant$1 s). Steady state magnetic field can be generated by immersing a superconducting coil in liquid helium, which maintains the temperature of the superconducting coil blow the critical temperature T_c. In commercially available systems, the value of the magnetic field in the superconducting coil is limited to 22 T by the critical current of the superconducting wire. Further increase of the magnetic field can be achieved using resistive coils. In this case, magnetic fields of $\simeq$ 38 T can be reached today, limited by the thermal (cooling) and mechanical constraints. A hybrid magnet, a combination of an outer superconducting and an inner resistive coil, generates a magnetic field beyond the limitation of a purely resistive coil, up to 45 T [Miller 1994].

To reach magnetic fields above 45 T, we have to turn to pulsed magnetic field techniques. The principle of the pulse magnetic field is relatively simple. A capacitor bank is charged to a certain voltage and then discharged into the resistive coil. The electrical energy is transfered from the capacitors to the coils, which creates

a current pulse in the resistive coil. The maximum magnetic field of the pulse proportional to the voltage to which the capacitor bank was charged.

The Laboratoire National des Champs Magnétiques Intenses-Toulouse (LNCMI-T) is one of the world leading laboratories, which provides up to 90 T non-destructive long pulse ($\leqslant$ 1 s) and up to 150 T semi-destructive, ultrashort ($\leqslant$ 10 μs), pulsed magnetic field. LNCMI-T serves as a user facility providing open access to researchers from all over the world. During this thesis, all the spectroscopy measurements in high magnetic field have been performed at LNCMI-T.

2.1.1 Generator

The energy required to energize the resistive coils is stored in three different capacitor banks (14 MJ, 6 MJ, 1.15 MJ). All capacitor banks can be charged up to 24 kV. Fig. 2.1(a) shows a panoramic view of the 14 MJ capacitor bank. It consists of 14 capacitor units. Each unit stores energy up to 1 MJ, with total capacitance of 48 mF. The 6 MJ capacitor bank consists of two 3 MJ units, with total capacitance of 21 mF. In addition, there is a 1.15 MJ mobile capacitor bank with a capacitance of 4 mF. These three capacitor banks can be combined with different resistive coils, resulting in a different duration and value of the magnetic field pulse.

2.1.2 Resistive coils

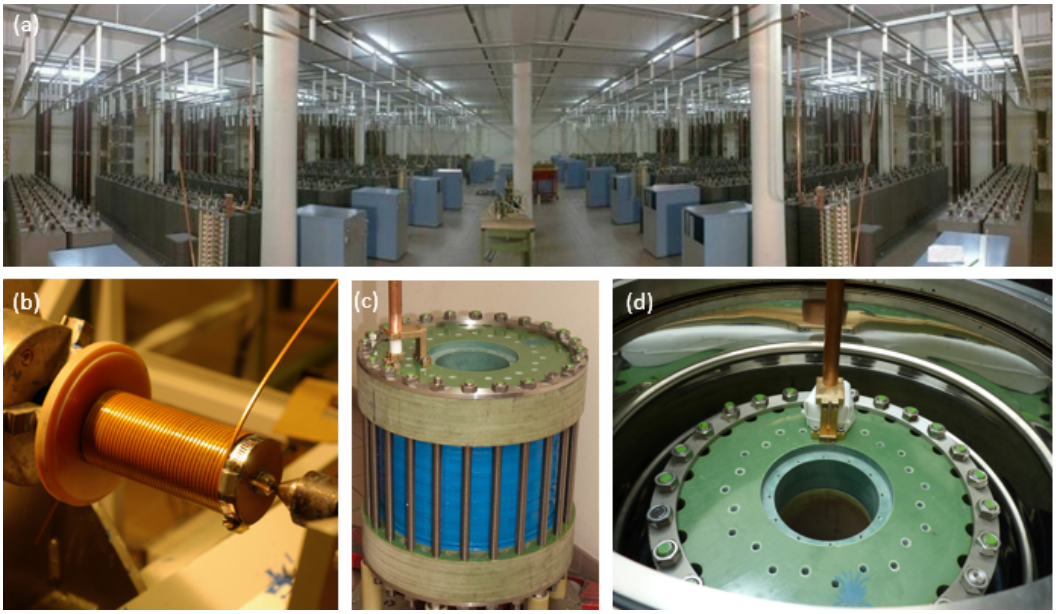

Figure 2.1: (a) Panoramic view of 14 MJ capacitor bank; (b) copper wires for the coil; (c) photo of a complete 70 T coil; (d) a standard coil mounted in a liquid nitrogen cryostat.

The resistive coils are designed, and manufactured in house in the LNCMI-T

technical workshop. In order to sustain the high magnetic field pressure originating from the Lorentz force and to minimize coil heating, the material of the coil has to fulfill three important condition, (i) high intrinsic strength, (ii) high ductility and (iii) high electrical conductivity. However, high strength conductors usually have a low ductility and a reduced electrical conductivity. To overcome this problem, special reinforcement of the copper stainless steel-(CuSS) wires with Zylon is used. The CuSS wires are used to wind the coil with approximately 1000 turns, as shown in Fig. 2.1(b). Afterwards, additional protection and contacts are made on the winding wires to form a complete resistive coil. A complete 70 T coil is shown in Fig. 2.1(c).

To avoid overheating during the pulse of the magnetic field, the resistive coils are immersed in liquid nitrogen in a specially designed nitrogen cryostat as presented in Fig. 2.1(d). Cooling the coil also reduces the resistance of the metallic copper wires. During each pulse of the magnetic field, the temperature of the resistive coil increases due to the Joule effect. Immersing the resistive coils in liquid nitrogen prevents destructive explosion of the coil due to overheating. The time required to cool the coils between magnetic field pulses varies from several minutes to several hours depending on the strength of magnetic field and the length of the pulse. LNCMI-T has developed a fast cooling channel method, which reduces the cooling time by a factor of $\simeq 3$ [Frings 2008].

Different combination of the resistive coil with the different generators result in a duration of the magnetic field pulses varying from a few tens to several hun-

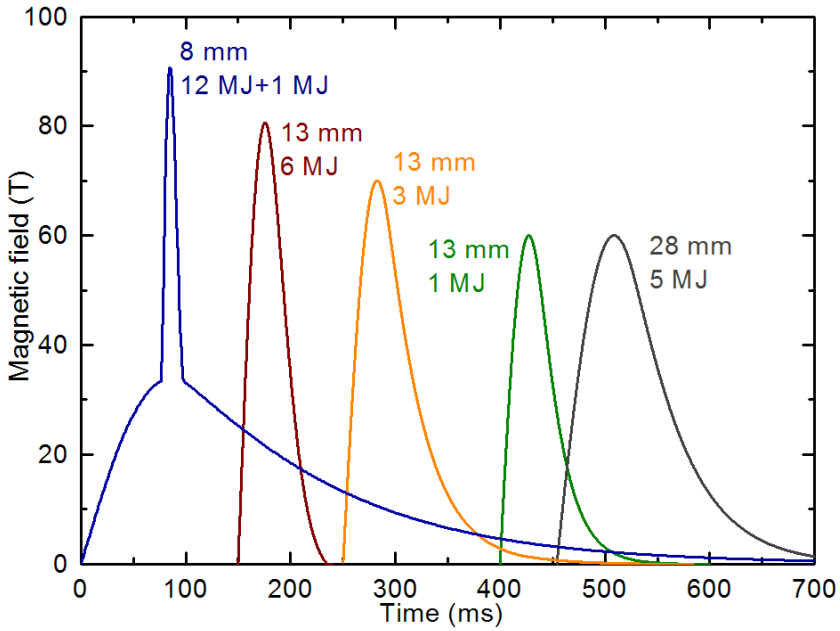

Figure 2.2: Representative magnetic field pulses as a function of time for different coils systems. Diameter of the magnet bore and the energy required for each systems are marked next to each curve.

dreds of milliseconds, accompanied with the maximum magnetic field from 60 T to 90 T. Fig. 2.2 shows the magnetic field as a function of time obtained by different combination of the resistive coil and the generator. The inner bore diameter of the resistive coil and the energies required for each magnetic field pulse are marked next to each curve. For example, the inner bore diameter of the 70 T magnet is 13 mm (See orange solid line in Fig. 2.2). The typical duration of a 70 T pulse is 150 ms if the 6 MJ capacitor bank is used for charging the coil. Magnets with a maximum magnetic field below 80 T are single coil systems, while the 90 T magnet is a dual-coil system. The outer magnet, energized by 1.15 MJ mobile capacitor bank, generates a 34 T long background pulse, while the inner magnet combined with 14 MJ capacitor bank generates a short 62 T pulse [Béard 2013]. Synchronizing the maximum field of the two pulses creates a magnetic field of 90.2 T with a duration of 9.2 ms (see the blue solid line in Fig. 2.2). In this thesis, all the magneto-optical measurement have been performed using a standard 70 T magnet with fast cooling channels.

2.1.3 Cryogenics

For the pulsed magnetic field measurement, the liquid helium cryostat is placed in the magnet bore, as schematically shown in Fig. 2.3(a). Due to the high magnetic field environment and the limited space in the magnet bore, special helium cryostats are required. As presented in Fig. 2.3(a), the liquid helium cryostat consists of top and bottom baths connected by a capillary and a needle valve. The top bath is used

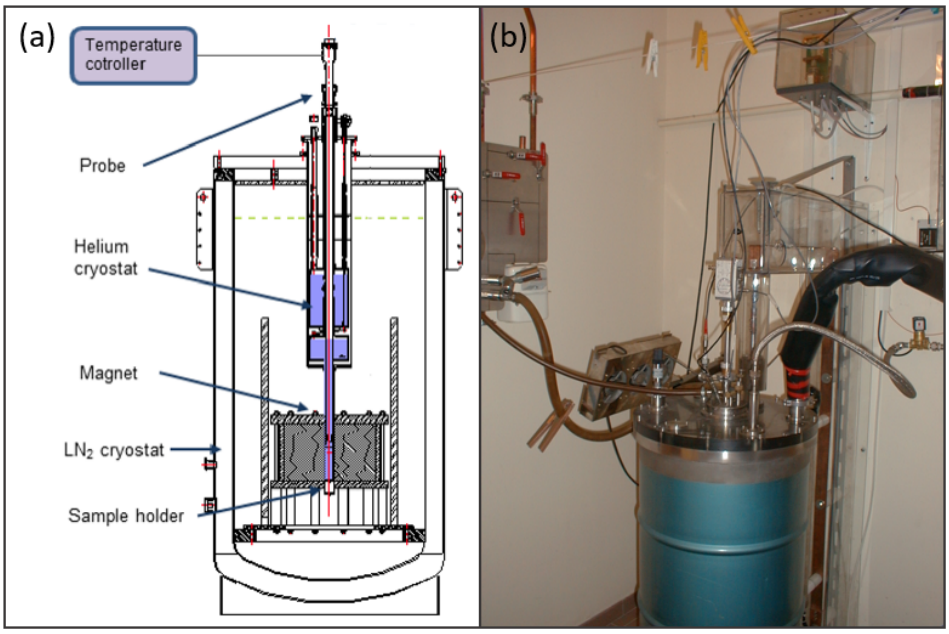

Figure 2.3: (a) A schematic view and (b) a photo of a pulsed magnetic field experiment setup.

to store liquid helium transfered from a helium dewar. The bottom bath has a long extension (tail) which is inserted directly into the magnet bore. The sample holder is placed inside the tail. A resistive heater made from manganin wires is placed around the tail. It allows to control the temperature from 4.2 K (liquid helium) to 300 K by adjusting the input power of the heater [LNCMP-team 2004].

Table 2.1: The inner diameters of the magnet bore and the extension suitable for three different magnet.

Magnet	Magnet bore (mm)	Extension (mm)
100 T	8	4
70 T	13	7
60 T	28	21

According to the diameter of the magnet bore, three type of helium cryostats are used. The main difference between them is the inner diameter of the tail. Table 2.1 shows the diameter of the magnet bore and the corresponding inner diameter of the tail for three different magnets. Photo of a typical experimental setup is presented in Fig. 2.3(b)

2.2 Magneto transmission measurements

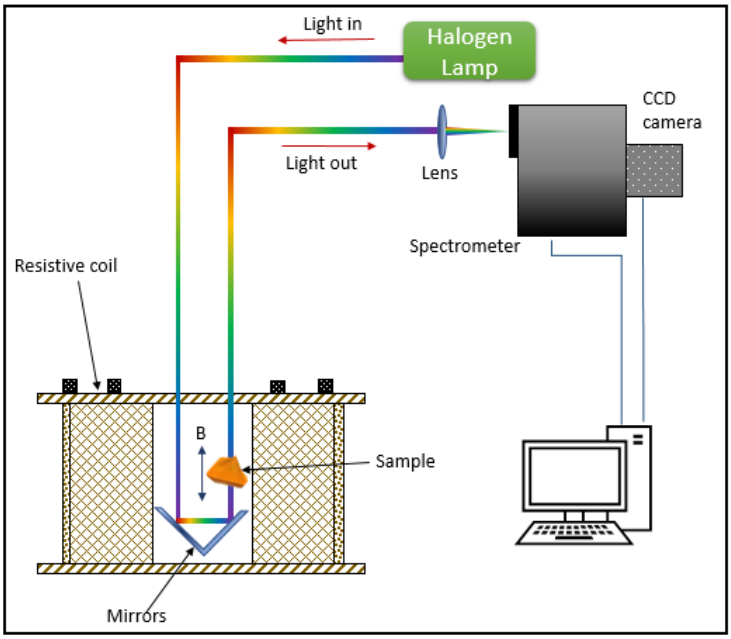

Figure 2.4: Schematic drawing of the transmission measurement in pulse magnetic field.

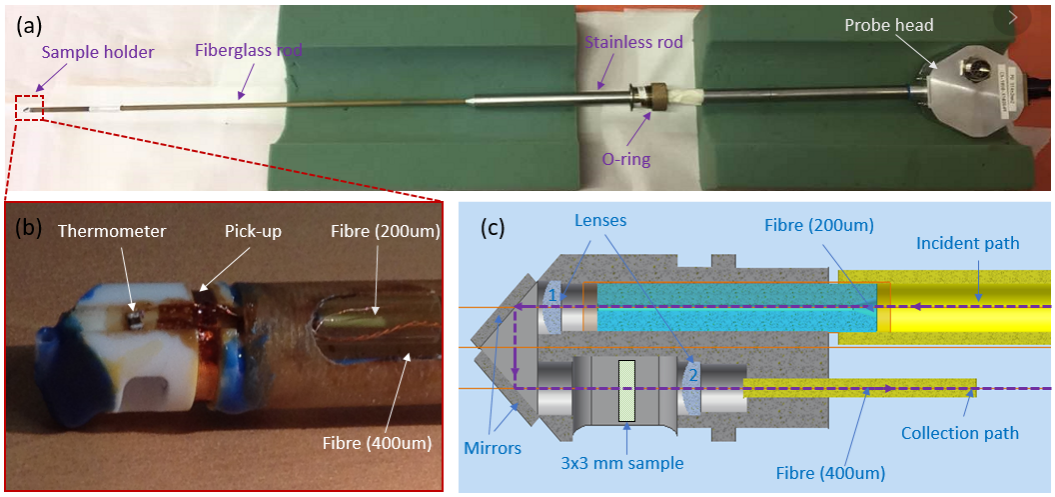

Figure 2.5: (a) Photo of the magneto-transmission probe. (b) Zoom of the sample holder. (c) Schematic of the optical path.

One of the experimental techniques used in this thesis is magneto-transmission, which is suitable to investigate thin samples on a transparent substrate. We have measured the spectra of the transmitted light through the sample, which is placed in the center of the field. The general idea of the magneto transmission measurements is presented in Fig. 2.4.

Due to the limited space in the helium cryostat, a special transmission probe has been designed. The photo of the transmission probe used in our experiment is shown in Fig. 2.5(a). The material of the probe inserted into the magnet has to be insulating to avoid eddy current heating and magnetic forces during the pulse of the magnetic field. The top part of the probe consists a hexagonal head and a 19 mm rod made of the stainless steel. The bottom part of the probe consist a 7 mm rod and a sample holder. The rod is made of low thermal expansion coefficient epoxy fiberglass, while the sample holder is made of ceramic. The entry of the probe to the helium cryostat is sealed by a movable o-ring on the stainless steel rod, which allows the probe to be moved vertically in the cryostat to adjust the position of the sample to be exactly in the center of the magnetic field.

A schematic representation of the optical path in the probe is shown in Fig. 2.5(c). Two multi-mode fibers are used to guide light, one is 200 μm diameter fiber used to guide the incident light beam from a broad-band tungsten-halogen lamp. At the end of the fiber, lens (1) is used to collimate the beam. Two gold plated mirrors are used to reflect the beam to the sample space. Then, the beam, transmitted through the sample, is focused by the lens (2) on the second fiber with 400 μm diameter, which guides the signal to the spectrometer.

This probe is equipped with a thermometer and pick-up coil, as shown in Fig. 2.5(b). To precisely measure the temperature of the sample, we use a Cernox thermometer. Three pairs of 100 μm diameter coper wires are used to connect

the thermometer and the pick-up coil to the socket of the probe head. We use twisted wire pairs to reduce the voltage induced by the pulsed magnetic field.

2.2.1 Pick-up coil

In order to measure precisely the value of the magnetic field on the sample during the magnetic field pulse, a small coil is wound around the sample holder, referred to as a pick-up coil (see Fig. 2.5(b)). It is made of 50-100 turns of 100μm diameter insulated copper wire. The pulse of the magnetic field induces a voltage (V) in the pick-up coil,

$$V = -\frac{d\phi}{dt} = -N \times S\frac{dB}{dt}, \tag{2.1}$$

where ϕ is the magnetic flux, N is the number of turns and S is the surface of one spire. $N \times S$ is the effective area of the whole pick-up coil, which is determined as follow. The pick-up coil is placed in the center of 1 m long calibration coil with known B (I) dependence. The oscillator output of a lock-in amplifier is used to generate a sinusoidal magnetic field in the calibration coil. The pick-up coil voltage is recorded by the lock-in amplifier at the same time. If the magnetic field is known, then the area of the pick-up coil can be calculated using equation 2.1.

2.2.2 Resistance thermometer

A Cernox thin film resistor is used as a thermometer on the probe. Cernox resistors are convenient due to their small package size, which makes them easily fit to the limited space in the probe (see Fig. 2.5(b)). In order to obtain a precise resistance value, we use four-terminal sensing to measure the resistance. The schematic diagram of four-terminal sensing is shown in the inset of Fig. 2.6. Separated measurements of the current and voltage eliminates the contact and lead resistance, leading to a precise measurement of the resistance values.

The resistance/temperature relationship varies between different Cernox. Thus, the resistance/temperature relation of the Cernox has to be calibrated for each thermometer. It is typically done in a following way. The Cexnox to be calibrated is placed on a calibration probe next to a calibrated Cernox. The calibration probe is immersed in a helium cryostat. As the liquid helium slowly evaporates and the cryostat warms up, the temperature increases from 4.2 K to 293 K. The resistance of both Cernox are recorded by a Lakeshore temperature controller. Typically, these data are record every 5 or 10 seconds. An example of calibrated resistance/temperature relationship is represented in Fig. 2.6. The calibrated curve obtained is uploaded to the Lakeshore temperature controller connected to our probe. The data has to be interpolated due to the limited data points that can be stored by the controller (typically 200 data points).

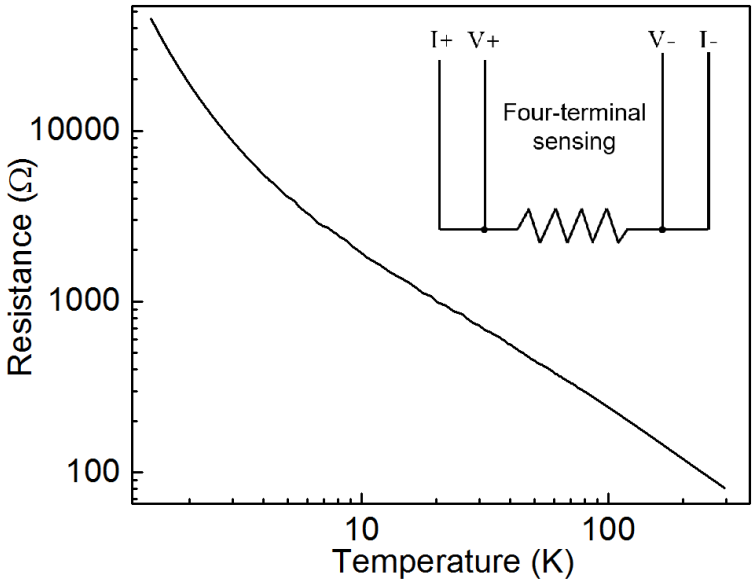

Figure 2.6: Typical calibrated resistance/temperature relationship of resistance thermometer on the transmission probe. Inset: schematic diagram of four-terminal sensing.

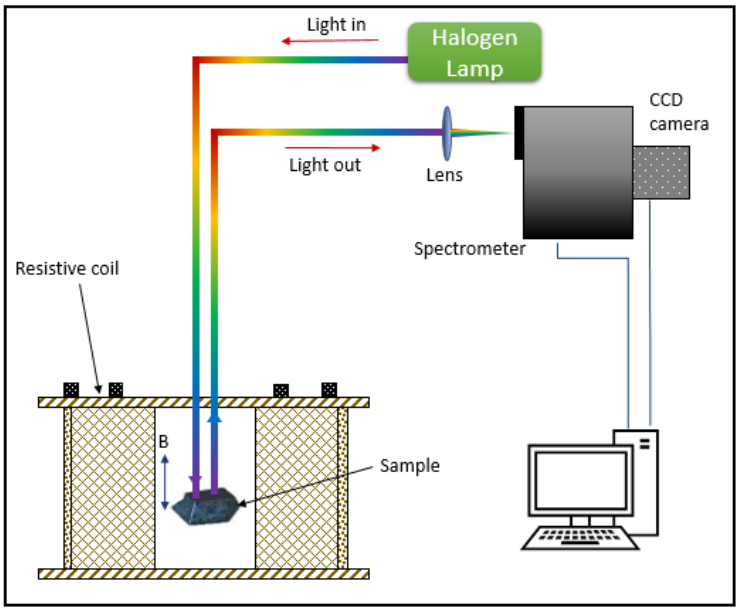

Figure 2.7: Schematic drawing of the reflectivity measurement in pulse magnetic field.

2.3 Magneto reflectivity measurements

For thick samples, we have used a magneto-reflectivity technique. The schematic illustration of the reflectivity set-up is presented in Fig. 2.7. In this case, the incident white light is directly reflected by the sample, and the reflected light is guided to the spectrometer.

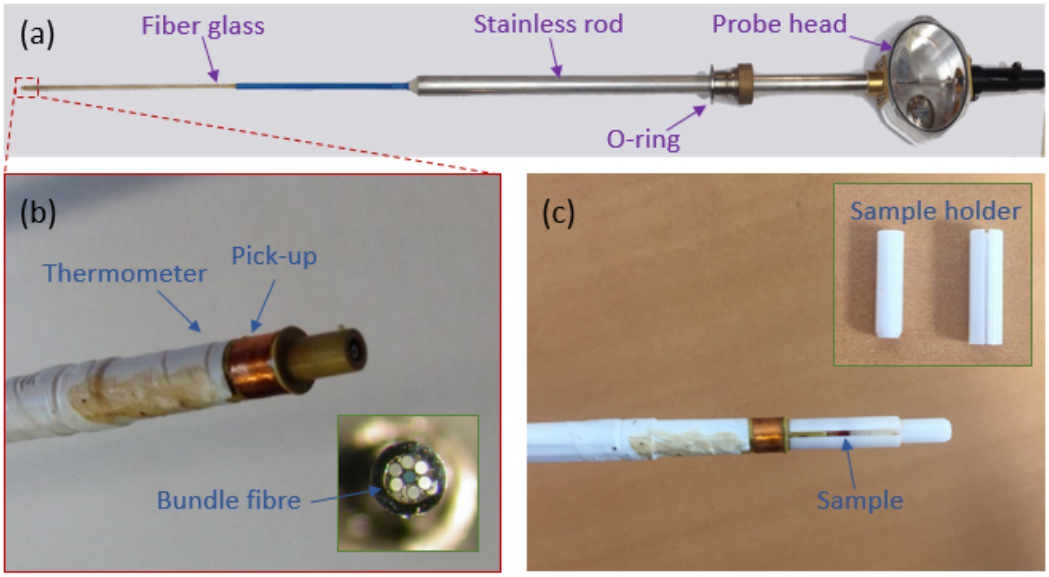

Figure 2.8: (a) Photo of the magneto-reflectivity probe. (b) Zoom on the bottom of the probe, where the pick-up coil and thermometer can be seen clearly. Inset: section of fiber bundle at the bottom of the probe. (c) Sample holder with the sample inside. Inset shows disassembled sample holder.

We have designed and built a probe adapted for such an experiment. Fig. 2.8(a) shows the photo of the reflectivity probe. As before, the probe is mainly made of stainless steel and fiber glass. We use a fiber bundle composed by 7 fibers with 100 μm diameter. The cross-section of the fiber bundle is shown in the inset of Fig. 2.8(b). The fiber in the center is used to guide the excitation light to the sample, then the reflected signal is gathered by the 6 collection fibers surrounding the central fiber. Fig. 2.8(b) shows the bottom of the probe, where the positions of pick-up coil and thermometer are indicated. The thermometer is located in a slightly higher position than pick-up coil and is covered by the teflon tape for protection.

The sample holder consists of a 2.5 mm diameter ferrule and a sleeve made of ceramic (see the inset of Fig. 2.8(c)). The size of the sample should be less than 2.5 mm, and the sample is placed on the top of the ferrule, then the ferrule and the probe head are then connected by the sleeve. The assembled probe and the sample holder are shown in Fig. 2.8(c). It is worth to mention that the diameter of the white fiber glass rod is only 4 mm, which allows the probe to be used in both the

100 T helium cryostat (4 mm diameter) and 70 T helium cryostat (7 mm diameter).

2.4 Synchronization

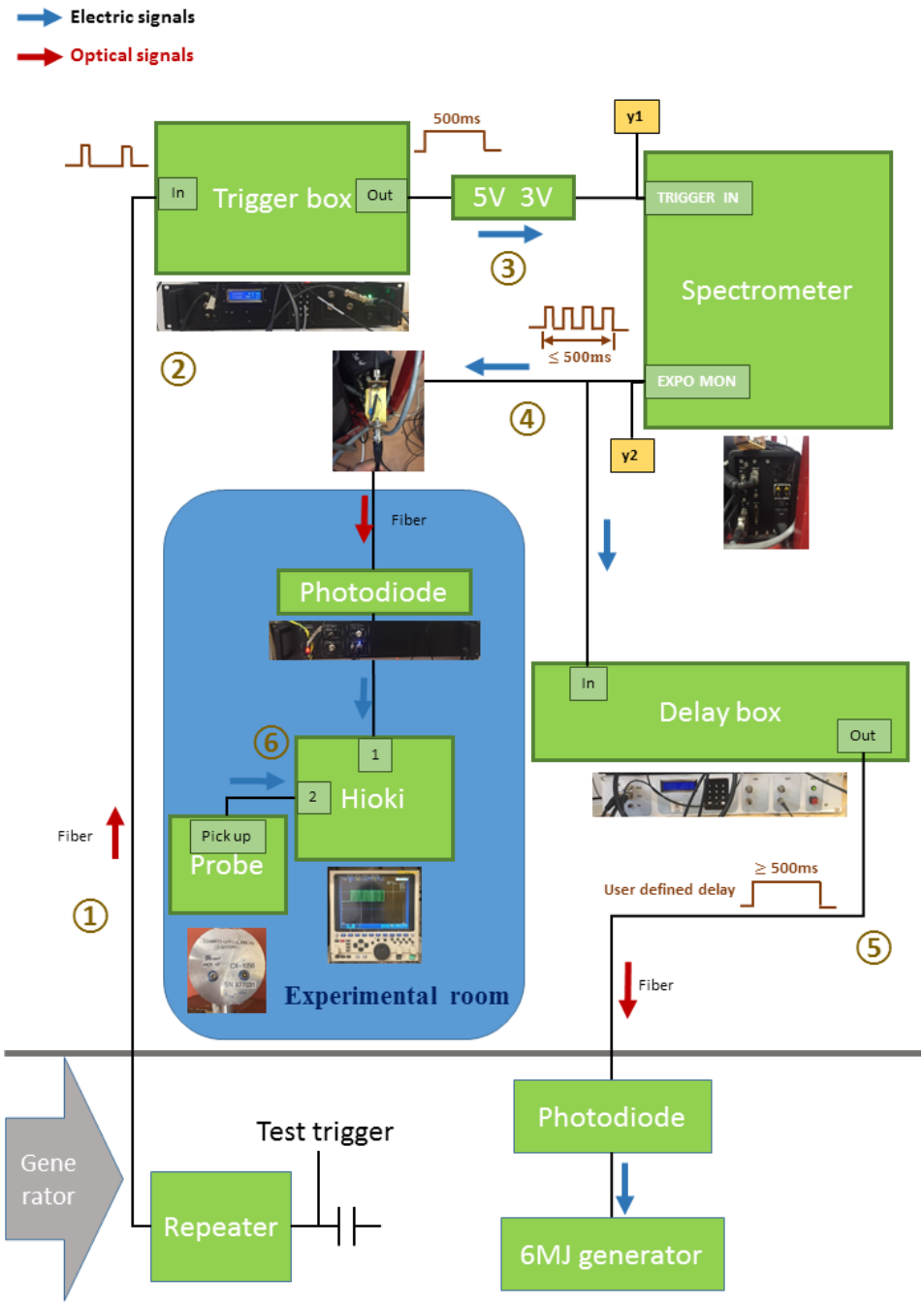

Figure 2.9: Schematic diagram of synchronization sequence for magneto-optical measurements

Since the 70 T magnetic field pulse only lasts 150 ms and the typical time to acquire a spectrum using the CCD camera is 1-2 ms, it is crucial to synchronize the magnetic field pulse with the CCD acquisition. A system was designed for this temporal synchronization with a precision of 0.1 ms. The schematic diagram is shown in Fig. 2.9. A typical sequence of the events is listed as follow:

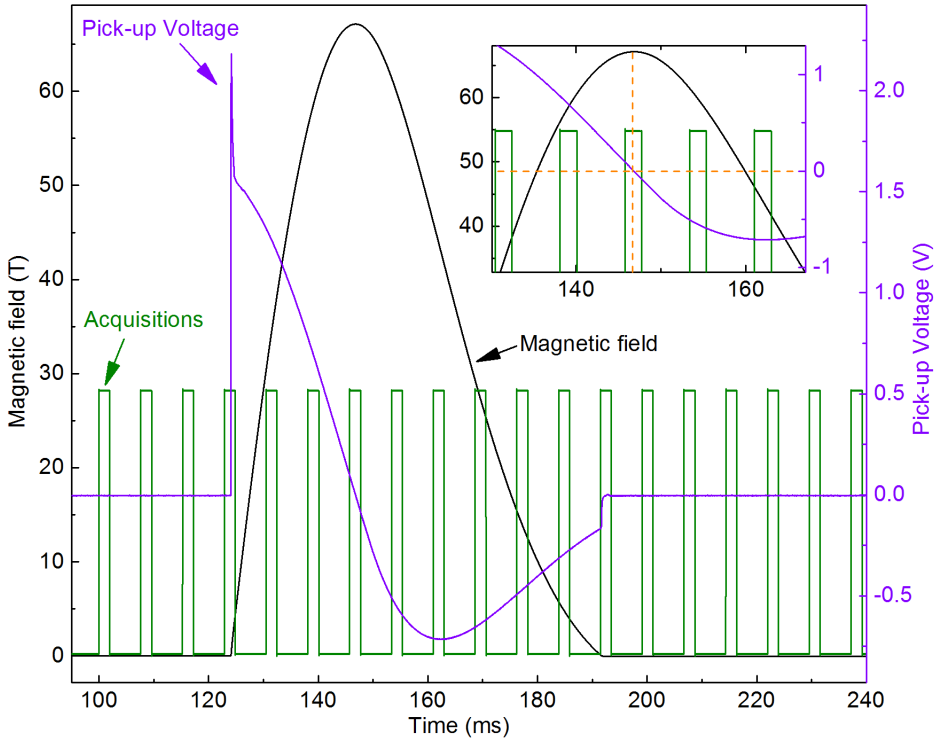

Figure 2.10: Magnetic field (black solid line), pick-up voltage (violate solid line) and CCD acquisition as a function of time during 68 T pulse. The synchronization of CCD acquisition and maximum magnetic field are shown in the inset.

(1) First, the repeater sends an optical continuous pulse signal as a pre-trigger to the delay generator (marked as trigger box) via a multi-mode fiber.

(2) Trigger box converts the optical continual signal to electrical signal pulse signal with 500 ms duration. Voltage of this electrical signal is TTL (5 V).

(3) The input signal for triggering the CCD cameras accepts only 3 V TTL signal, therefore, a voltage converter between the trigger box and the spectrometer is used.

(4) After the spectrometer is triggered, it sends a sequence of multiple acquisitions to the delay box and a digital oscilloscope (Hioki). Between the spectrometer and Hioki, there is a LED and a photo diode. The LED, outside of the experimental room, converts the electrical signal to optical signal. The photo diode, inside of the experimental room, converts the optical signal to electrical signal. The principle here is that all the connection from outside to inside of the experimental room has

to avoid using metallic cable, optical fibers are responsible for all the connections.

(5) Delay box is used to adjust the delay to have a maximum of the magnetic field in the middle of one of the CCD acquisition frames (see inset of Fig. 2.10). The delay box converts the electrical multiple acquisition signal to 500 ms single optical signal and sends it to the generator. Next, the generator discharges into the coil giving a high magnetic field pulse.

(6) The voltage of the pick-up coil on the probe, during the pulse of the magnetic field, is recorded by a Hioki. The magnetic field as a function of time is calculated by integrating the voltage. Typical results are shown in Fig. 2.10, where we show the voltage of pick-up coil (purple line) and the sequence of CCD acquisition (green line) as a function of time during a 68 T pulse. Based on equation 2.1 which shows that voltage of the pick-up is just the derivative of the magnetic field, the magnetic field is calculated by integrating the voltage of pick-up. The magnetic field as a function of time is shown in Fig. 2.10 as black solid line. Each rectangle of the green line represents a CCD acquisition with a typical duration of 2 ms, which ensures that the spectra are acquired at an essentially constant magnetic field. In the case of Fig. 2.10, the delay time is 24 ms, which ensures the 7th acquisition corresponds to the maximum field (see the inset of Fig. 2.10).

Chapter 3

Magneto-transmission on $MAPbI_3$ polycrystalline films

Contents

*In this chapter, we describe magneto-transmission measurements, which lead to the precise determination of the exciton binding energy and reduced mass in thin film perovskite materials. By investigating thin films with a wide range of crystal grain sizes, varying from tens of nanometers to microns, we elucidate the impact of the microstructure on the Coulomb interaction between photo created electrons and holes in $MAPbI_3$ and $Cs_{0.05}(MA_{0.17}FA_{0.83})_{0.95}Pb(I_{0.83}Br_{0.17})_3$ materials. The results presented in this chapter have been published in Energy Environ. Sci., **10**, 1358-1366 (2017).*

3.1 Introduction

Due to the different fabrication methods, thin film perovskites exhibit a variety of morphologies, resulting in crystal grain sizes which vary from tens of nanometers to tens of microns [Huang 2014, D'Innocenzo 2014b]. In this chapter, we investigate the correlation between the morphology of the thin film perovskites and the excitonic properties. To do so, we perform magneto-transmission measurements to extract the binding energy and reduce mass of excitons in $MAPbI_3$ and $Cs_{0.05}(MA_{0.17}FA_{0.83})_{0.95}Pb(I_{0.83}Br_{0.17})_3$ thin films, with a wide range of the crystal grain sizes.

3.2 Magneto-transmission spectroscopy on $MAPbI_3$

First, we will discuss the results for $MAPbI_3$. We have performed low temperature magneto-transmission spectroscopy to investigate $MAPbI_3$ thin films with different morphologies, using long magnetic field pulse techniques as described in detail in chapter 2. The investigated materials are $MAPbI_3$ thin film perovskites with a wide range of grain sizes from tens of nanometers to hundreds of nanometers.

3.2.1 Description of the samples

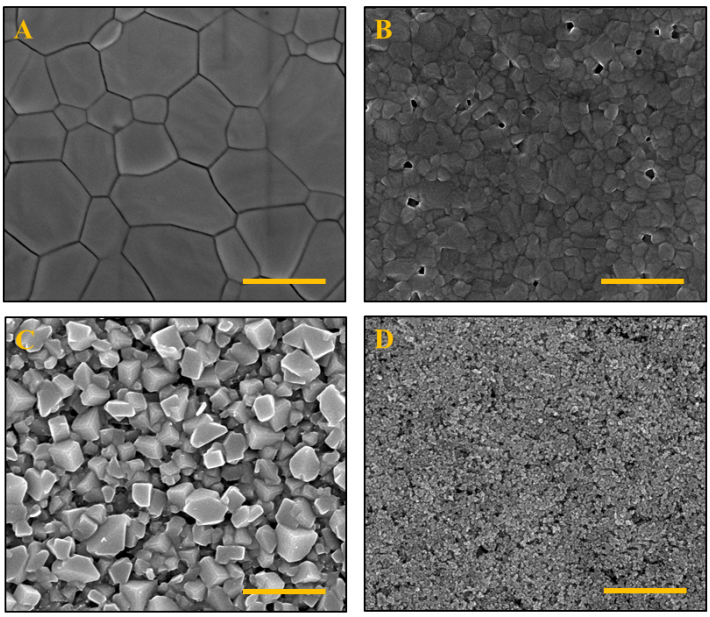

Figure 3.1: Top view SEM images of $MAPBI_3$ thin film deposited on glass substrates with various morphologies. (A) Polycrystalline thin film with an average crystal grain size 770±230 nm (LPC). (B) Polycrystalline thin film with grain size 210±60 nm (SPC). (C) Small crystals of $MAPBI_3$ fabricated with the two-step solution-processed dipping technique, resulting crystal size 290±70 nm (SC). (D) $MAPbI_3$ infiltrated into a thick mesoporous-Al_2O_3, resulting crystal grain size $<$ 50 nm (MP). Scale bars are 1 μm for each panel.

We have measured four different $MAPbI_3$ thin films. They have been fabricated via different methods, resulting in the morphologies with a wide range of different degrees of structural disorder and poly-crystallinity.

Fig. 3.1 represents the top-view scanning electron microscope (SEM) images of the samples. The morphologies vary from a planar polycrystalline film with grain sizes of 770±230 nm (A: Large grain polycrystalline annotated LPC) and polycrystalline film with grain sizes of 210±60 nm (B: Small grain polycrystalline annotated SPC), to small crystals of 290±70 nm fabricated by a two-step dipping

technique. (C: Small crystal annotated SC) and also perovskite infiltrated into a 2 μm thick mesoporous Aluminum oxide scaffold (mp-Al_2O_3) with grain sizes of <50 nm (D: Mesoporous crystal annotated MP).

The SPC, SC, MP samples have been fabricated by Arman Mahboubi Soufiani at the Australian Centre for Advanced Photovoltaics, University of New South Wales. Arman Mahboubi Soufiani also performed the SEM measurement on the SPC, SC, MP samples. The LPC sample has been fabricated by Roberto Brenes in the Research Laboratory of Electronics, Massachusetts Institute of Technology. Roberto Brenes also performed the SEM measurement on the LPC sample.

3.2.2 Magneto-transmission spectra on LPC sample

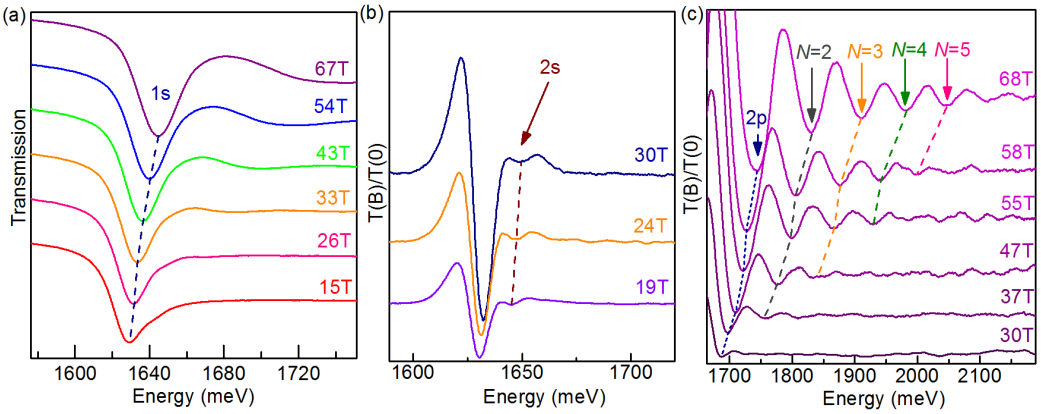

Figure 3.2: Typical magneto-transmission spectra of a LPC sample. (a) Sequences of typical transmission spectra of the LPC sample measured at the indicated magnetic fields. (b) A sequences of the ratios of the transmission spectra measured at intermediate magnetic field, which clearly shows the 2s state. (c) A sequences of the ratios of the transmission spectra in the higher energy range, which clearly shows the Landau level interband transitions.

The experimental approach and data analysis used for all the samples will be explained in detail using as an example results for the LPC sample. Typical magneto-transmission spectra of the LPC sample measured at the indicated values of magnetic field at low temperature (2 K) are presented in Fig. 3.2(a). For each spectrum, we observe a minimum, which corresponds to the 1s excitonic transition. The 1s states blue shifts with increasing magnetic field. For an unambiguous identification of the weaker optical transition, we show in Fig. 3.2(b), (c) the ratio of the transmission spectra at high magnetic field divided by the transmission spectrum obtained at zero magnetic field field. In Fig. 3.2(b), we present the ratio spectra measured at intermediate field (19-30 T), which shows clearly the 2s excitonic transitions. A sequence of the transitions marked with arrows start to be visible from 30 T in a higher energy range, as presented in Fig. 3.2(c). These transitions become more pronounced with increasing magnetic field. Their energies have a larger field-induced

blue shift than the low-energy transitions, which suggests that they are mainly free carrier transitions between Landau levels in the valence and conduction bands.

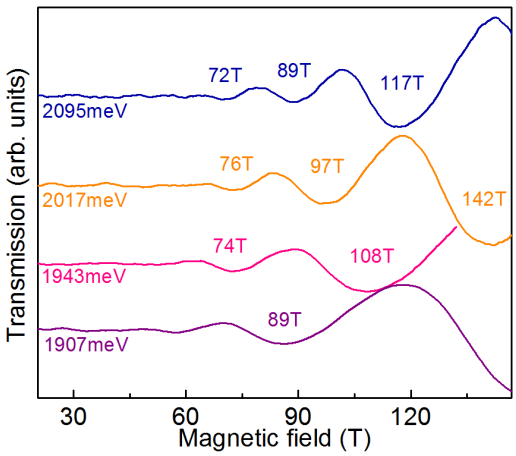

Figure 3.3: Typical results of the low temperature monochromatic transmission as a function of magnetic field obtained through the Mega Gauss technique performed by Dr. Atsuhiko Miyata.

To follow the free carrier transitions over an extended magnetic field range (70 T-150 T), we collaborated with Dr. Atsuhiko Miyata to perform Mega Gauss measurement at LNCMI-T. In this technique, the transmission of monochromatic (laser) light through the sample is measured as a function of the magnetic field. In Fig. 3.3, we show the typical results for the LPC sample. All the spectra show clear minima as a function of magnetic field, which correspond to the resonant transition between the free carrier Landau levels. The energy of the excitation laser is marked below each curve.

3.2.3 Data analysis

For the long pulse measurement, we analyzed each transmission spectrum to find the energy of the absorption at the indicated magnetic field. To do so, we take the energy at the center of each absorption minimum. After finding absorption energies for all the spectra, we plot them as a function of the magnetic field, as shown as colored spheres in Fig. 3.4(a).

For the Mega Gauss measurement, we analyzed each transmission spectrum to find the magnetic field for resonant absorption at the energy of excitation. To do so, we take the magnetic field at the center of each absorption minimum. We plot the excitation energies as a function of the magnetic fields, as shown as black stars in Fig. 3.4(a).

Assuming that free carriers transitions dominate in the high magnetic field range, we first fit the interband transitions between Landau level in the conduction and valence bands using Eq. 1.14. The reduced mass μ is the only fitting parameter for all the Landau levels. Modeling the high energy range and the high

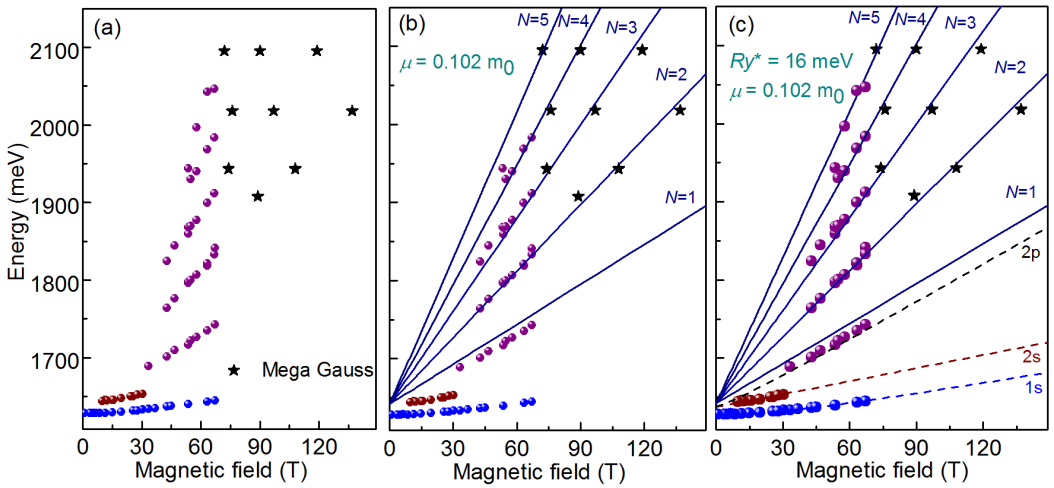

Figure 3.4: (a) Typical results of absorption energies as a function of magnetic field. The blue, red and violet spheres comes from the long pulse magnetic field measurement, while the black stars comes from Mega Gauss measurement measured by Dr. Atsuhiko Miyata in LNCMI-T. (b) Fitting of free carriers interband transition between Landau levels conduction band and valance band (blue solid lines). (c) The plot from panel (b) supplemented with the fitting curve of hydrogen like model for 1s, 2s and 2p (blue, red and black dashed lines).

magnetic field range of the data allows a precise determination of the reduced mass. The results of a typical fit of free carriers transition up to $N = 4$ for the LPC sample are shown in Fig. 3.4(b). For this sample, the reduced mass μ is estimated to be $0.102 \pm 0.002 m_0$.

Then, as the second step, we use Makado and McGill's numerical solutions for the hydrogen-like Hamiltonian to fit the data. The fitting parameters of this solution are the exciton reduced mass μ and the exciton binding energy R^*. We use the same reduced mass μ extracted from the interband Landau level transitions. The fitting results are shown as dashed lines in Fig. 3.4(c). In this sample, we observed three excitonic transitions - 1s, 2s and 2p. The observation of both 1s and 2s states gives a strong constraint on the value of exciton binding energy. The binding energy of exciton in LPC sample is estimated to be 16 ± 1 meV.

3.2.4 Magneto-transmission spectra on SPC, SC and MP samples

Next, we performed the same measurement and analysis on other $MAPbI_3$ samples (SPC, SC, MP) with different grain size. The typical magneto-transmission spectra of three different samples measured at 2 K are shown in Fig. 3.5. Panel (a)-(c) shows the transmission spectra measured at indicated magnetic field for SPC, SC and MP samples, respectively. As before, for each sample, 1s excitonic transitions dominate the spectra. Unfortunately, no 2s excitonic transition are visible for any of these samples. Panel (d)-(f) shows the ratios of the transmission spectra in magnetic field

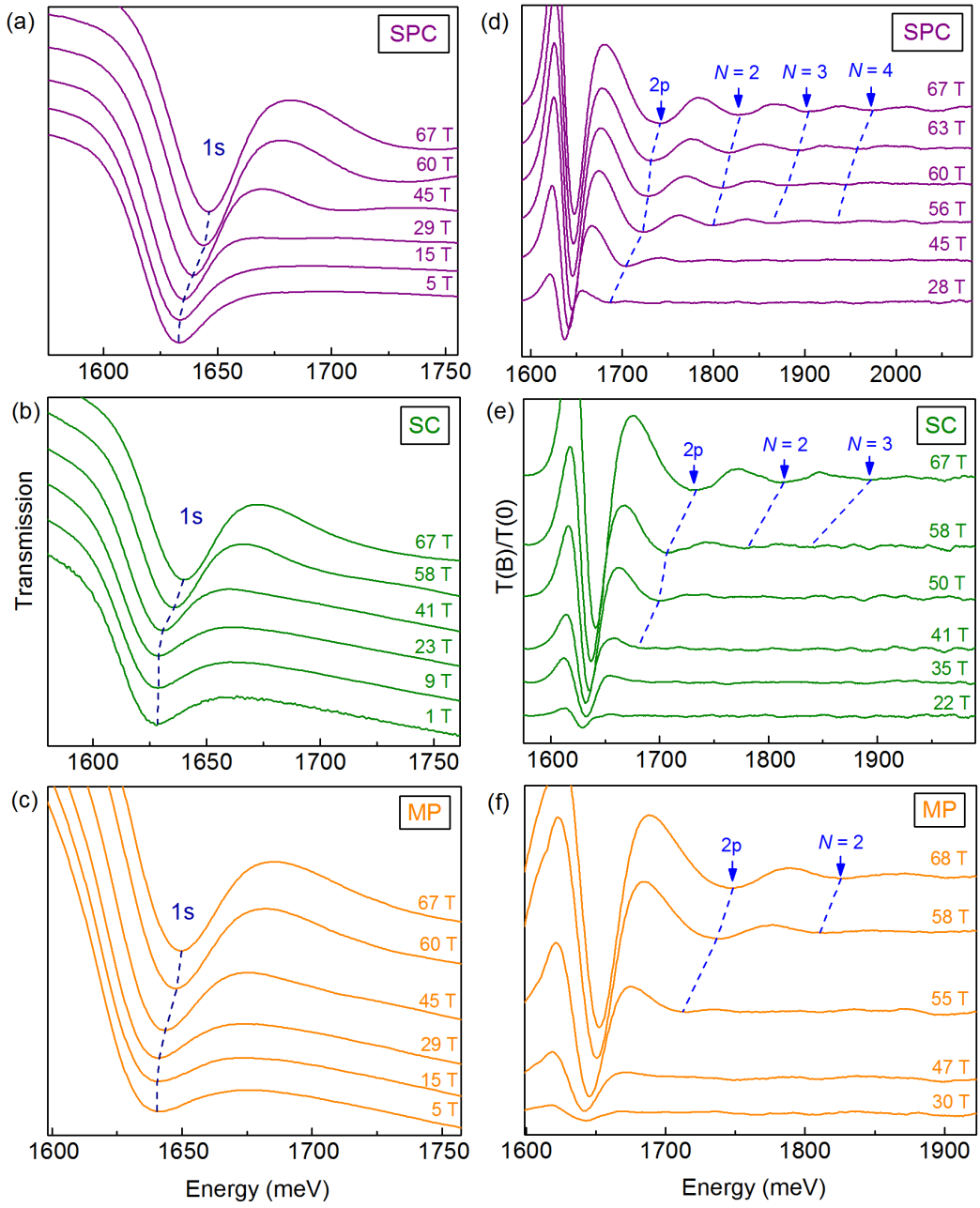

Figure 3.5: Panel (a)-(c) Low temperature transmission spectra measured at indicated magnetic fields for SPC, SC and MP samples, respectively. Panel (d)-(f) The ratios of the low temperature transmission spectra in magnetic field $T(B)$ to that measured at zero field $T(0)$ for for SPC, SC and MP samples, respectively.

$T(B)$ to that measured at zero magnetic field $T(0)$ for SPC, SC and MP samples, respectively. With the increase of the crystal size, the line-width of the 1s transition become smaller and more Landau levels are observed.

3.2.5 Results and discussion

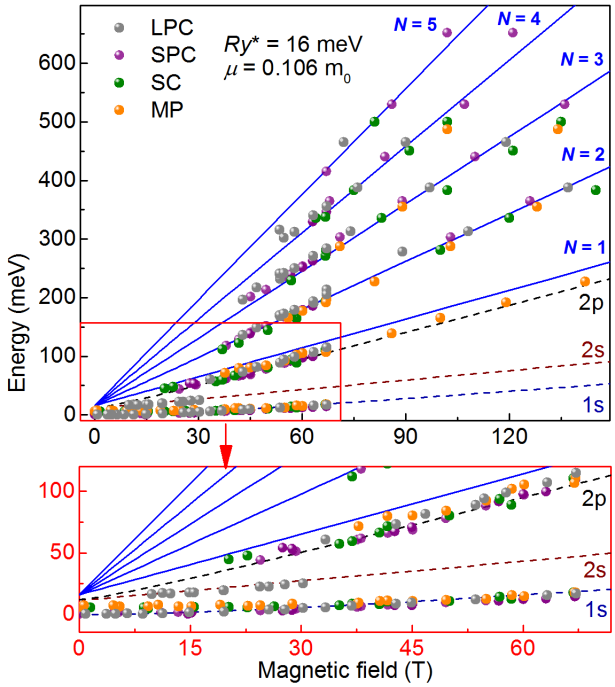

Figure 3.6: Overlaid fan chart of the LPC, SPC, SC and MP samples. The solid and dashed lines are the fits to the set of Landau levels and the excitonic transitions, respectively. The bottom panel shows the zoomed-in plot of the excitonic transition region of the fan chart.

In the absence of a clear observation of the 2s excitonic transition for the SPC, SC and MP samples, a global fit to the excitonic and free-carrier transitions is employed. To visualize the negligible change in the optical response under high magnetic fields of the $MAPbI_3$ with different morphology, the overlaid fan diagrams of the complete set of excitonic and free carrier optical transitions, after shifting by the corresponding bandgap offsets, are presented in Fig. 3.6. The fitting parameters for the global fit are $R_y^* = 16 \pm 1 meV$ and $\mu = 0.106 \pm 0.003 m_0$. Here we clearly show that these $MAPbI_3$ samples, although composed of dramatically different grain sizes and morphologies, exhibit very similar magneto-optical behavior.

In addition to the global fit shown in Fig. 3.6, we also fitted the data for the four morphologies of $MAPbI_3$ separately, as shown in Fig. 3.7. The spheres present the data points from long pulse measurement. The stars present the data points from Mega Gauss measurement performed by A. Miyata. The solid and dashed lines are the fits to the set of Landau levels and the excitonic transitions, respectively. The fitting parameter for the four samples are summarized in Table 3.1. In Fig. 3.8, we show a graphical representation of the summary in Table 3.1. The reduced mass and binding energy are presented with red circles and blue squares, respectively. The SEM image for each sample are inserted at the bottom of the figure. The reduced

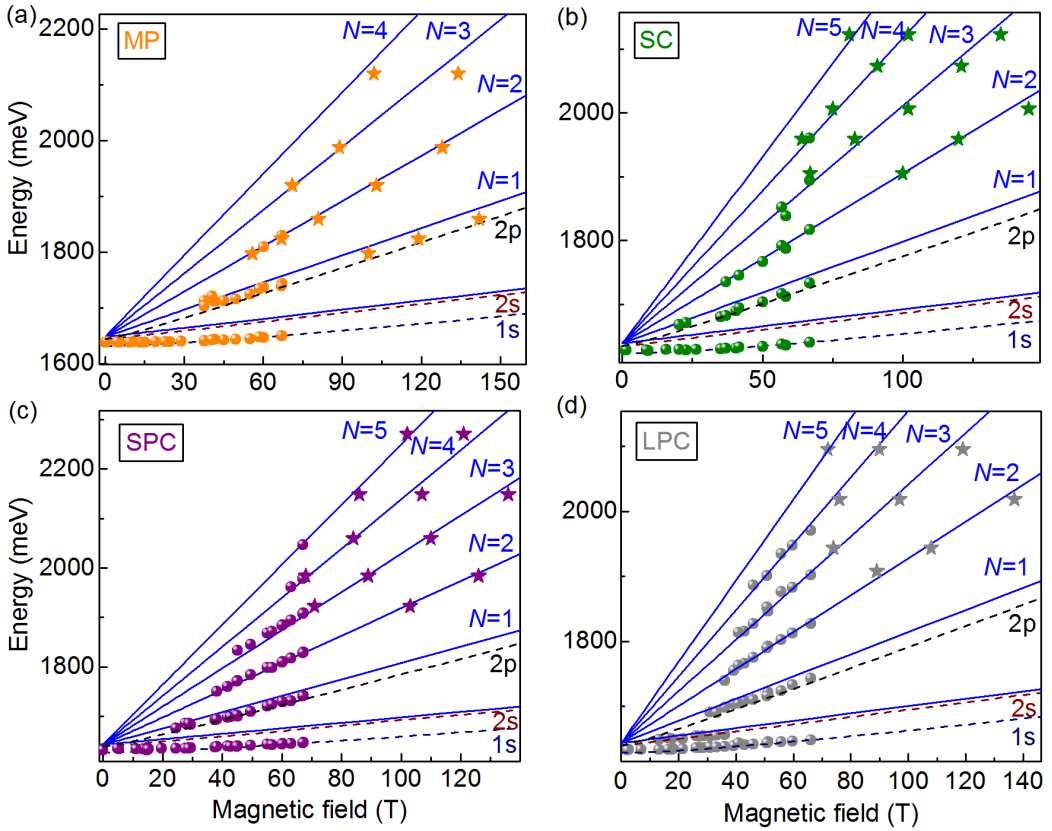

Figure 3.7: (a)-(d) Separate energy fan charts of the MP, SC, SPC and MP samples, respectively. The spheres present the data points from long pulse measurement. The stars present the data points from Mega Gauss measurement performed by A. Miyata. The solid and dashed lines are the fits to the set of Landau levels and the excitonic transitions, respectively.

Table 3.1: Summary of the fitting parameters for the four morphologies of $MAPbI_3$ in the low temperature (2 K).

	Crystal size (nm)	E_g (meV)	μ (m_0)	Ry* (meV)
LPC	770 ± 230	1642 ± 2	0.102 ± 0.002	16 ± 1
SPC	290 ± 70	1643 ± 2	0.105 ± 0.002	16 ± 4
SC	210 ± 60	1639 ± 2	0.109 ± 0.002	16 ± 4
MP	<50	1638 ± 2	0.107 ± 0.003	16 ± 4

mass varies from $0.102\,m_0$ to $0.109\,m_0$, while the binding energy remain the same for all the samples within experimental error. The binding energy of the exciton in the LPC sample is (16 ± 1) meV. While in SC, SPC, MP samples, it is (16 ± 4) meV. The difference in the size of the error bar comes from the observation of 2s state in LPC sample. The energy difference between the 1s and 2s state gives a strong

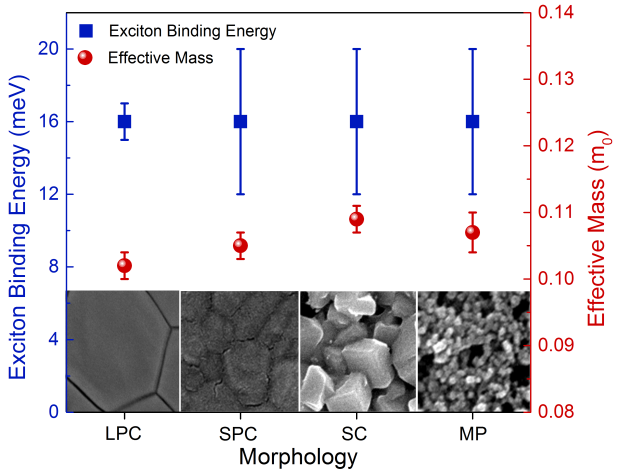

Figure 3.8: Exciton binding energy R^* and reduced mass μ for the various morphologies.

constraint on the exciton binding energy, resulting in a more precise determination of the exciton binding energy.

Recent reports have suggested that the permanent dipole moment of organic cation in small and defects in the crystals generates an electrostatic potential gradient, which causes an enhanced dielectric screening. This results in a very small value of the exciton binding energy of the order of 2-5 meV [Lin 2015, Grancini 2015]. On the other hand, large and defect free crystals exhibit an order of magnitude higher value of exciton binding energy [D'Innocenzo 2014a, Grancini 2015]. However, in our results, the value of exciton binding energy from the $MAPbI_3$ polycrystalline thin films with different crystal grain sizes are all identical. In addition, our results are in good agreement with the previous work of our group [Miyata 2015], which shows that the exciton binding energy and reduced mass of thin film $MAPbI_3$ are (16 ± 2) meV and $0.104\, m_0$, respectively. This indicates that, contrary to the reports in the literature [D'Innocenzo 2014a, Grancini 2015], the exciton binding energy is independent of the crystal grain size for the $MAPbI_3$ perovskite material. In fact, this is expected from the relative size of the exciton Bohr radius and the crystal grains. The Bohr radius of the exciton is 5 nm for all the $MAPbI_3$ morphologies in the low temperature phase [Soufiani 2017], which is substantially less even than the smallest crystal size (tens of nanometer) of thin film perovskite. This rules out any possibility of quantum confinement effect, which has an influence on the exciton binding energy.

3.3 $Cs_{0.05}(MA_{0.17}FA_{0.83})_{0.95}Pb(I_{0.83}Br_{0.17})_3$ thin films

To generalize our finding for $MAPbI_3$ to other perovskite compositions, we have performed magneto-transmission measurement on a state-of-the-art triple-cation lead mixed-halide perovskite, $Cs_{0.05}(MA_{0.17}FA_{0.83})_{0.95}Pb(I_{0.83}Br_{0.17})_3$ [Saliba 2016b].

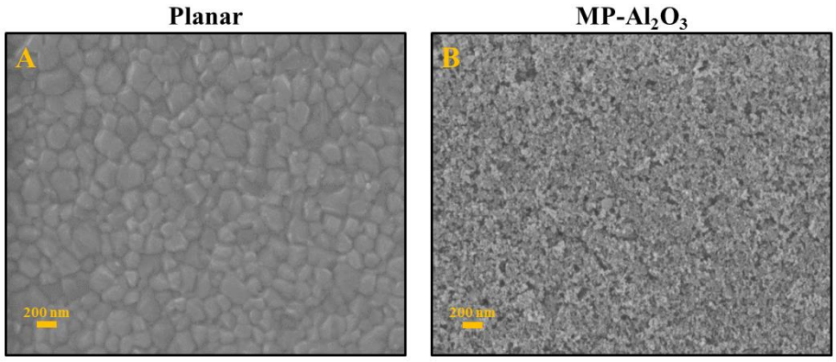

Figure 3.9: Top-view SEM images of $Cs_{0.05}(MA_{0.17}FA_{0.83})_{0.95}Pb(I_{0.83}Br_{0.17})_3$ thin films with two morphologies deposited on glass substrates. (A) Polycrystalline planar thin film. (B) $Cs_{0.05}(MA_{0.17}FA_{0.83})_{0.95}Pb(I_{0.83}Br_{0.17})_3$ infiltrated into a thick MP-Al_2O_3. Scale bars are 200 nm.

The samples were fabricated by Mojtaba Abdi Jalebi, at the Cavendish Laboratory, University of Cambridge. For simplicity, only two considerably different morphologies have been investigated, namely (i) a planar polycrystalline thin film (Planar) with the crystal grain size around 100-300 nm and (ii) a film with the perovskite infiltrated into a thick mp-Al_3O_2 scaffold (Mesoporous), with a resulting crystal grain size < 50 nm. The top-view SEM images of two morphologies taken by Mojtaba Abdi Jalebi are shown in Fig. 3.9.

3.3.1 Magneto-transmission spectra

Typical results of the magneto-transmission spectra measured at 2 K for $Cs_{0.05}(MA_{0.17}FA_{0.83})_{0.95}Pb(I_{0.83}Br_{0.17})_3$ samples are presented in Fig. 3.10. Panel (a) and (d) show the as measured transmission spectra for planar and mesoporous sample, respectively. Both spectra are dominated by a pronounced minimum, which corresponds to the 1s excitonic transition. The transition blue shifts with the increasing magnetic field. Panel (b) and (e) show the ratio transmission spectra for planar sample at 15 T and mesoporous sample at 33 T. At this intermediate magnetic field, we observe the 2s excitonic transition for both samples, which is critical for the accuracy of the fitting procedure. Panel (c) and (f) show the ratio transmission spectra for the planar and mesoporous sample measured at the indicated magnetic field. We observed the 2p excitonic transition and 3 Landau levels for the planar sample, while only the 2p excitonic transition is observed for Mesoporous sample in panel (f). This is probably due to the larger line width of the mesoporous sample, indicating a lower crystal quality.

3.3.2 Data analysis

As for the analysis of the $MAPbI_3$ samples, we take the transition energy at the minimum of the absorption line and construct the energy fan chart. We show the

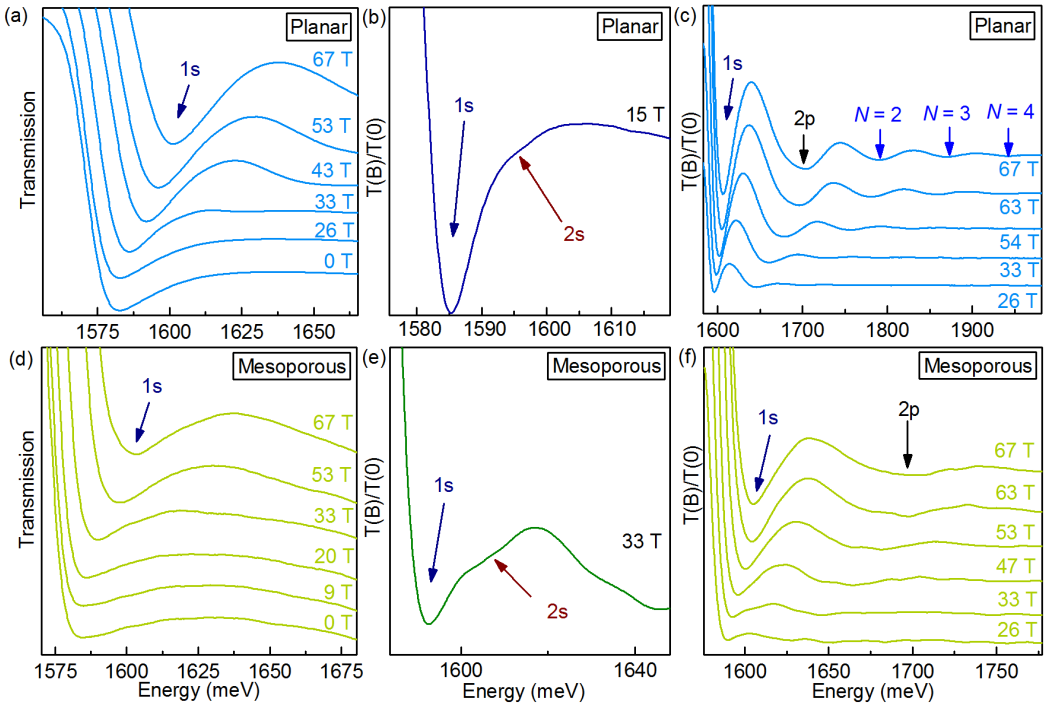

Figure 3.10: Left panels: typical transmission spectra of the polycrystalline (a) and perovskite-infiltrated mesoporous-Al_2O_3 (c) samples measured at indicated magnetic field at 2 K. Right panels: The ratio of the transmission spectra in the magnetic field $T(B)$ to that measured at zero field $T(0)$ for both morphologies sample.

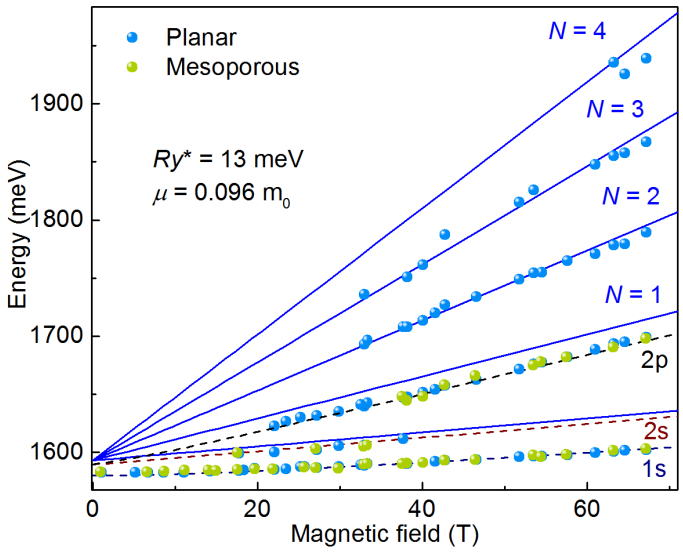

Figure 3.11: Overlaid fan chart of the planar and mesoporous samples. The solid lines and the dashed lines are the fits to the set of Landau levels and the excitonic transitions, respectively.

overlaid fan chart for both planar and mesoporous sample in Fig. 3.11. The green and blue spheres are the transition energies for mesoporous and planar samples, respectively. The solid and dashed lines are the fits to the set of Landau levels and the excitonic transitions, respectively. $R_y^* = 13 \pm 2\,\text{meV}$ and $\mu = 0.096 \pm 0.002\,m_0$ are employed as the fitting parameters. The excitonic transitions of the two morphologies show very good overlap. These results allow us to extend our conclusions to the wider alloyed perovskite family, giving strong proof that the micro structure has a negligible impact on the excitonic properties at low temperature.

Table 3.2: Summary of the fitting parameters for the two different morphologies of $Cs_{0.05}(MA_{0.17}FA_{0.83})_{0.95}Pb(I_{0.83}Br_{0.17})_3$ in the low temperature (2 K), orthorhombic phase.

	E_g (meV)	μ (m_0)	Ry* (meV)
Planar	1593 ± 2	0.096 ± 0.002	13 ± 2
Mesoporous	1594 ± 2	0.096 ± 0.008	13 ± 2

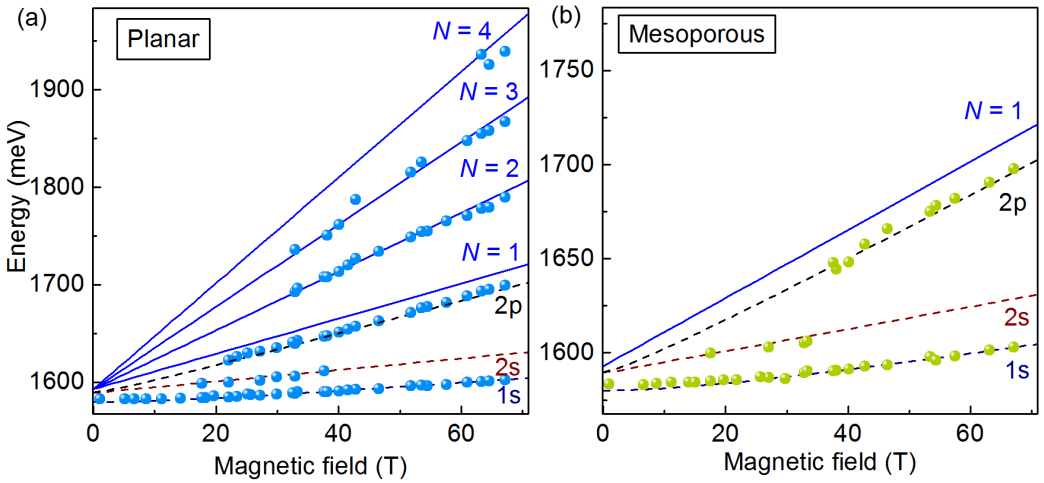

Figure 3.12: (a) Separate energy fan chart of the planar and mesoporous samples. The solid lines and the dashed lines are the fits to the set of Landau levels and the excitonic transitions, respectively.

We also fit the energy fan chart for both morphologies separately, as shown in Fig. 3.12 . A summary of the fitting parameter for both morphologies is shown in Table 3.2. The reduced mass $\mu = 0.096 \pm 0.008\,m_0$ and binding energy $Ry^* = 13 \pm 2\,\text{meV}$ are identical within experimental error for both morphologies. These values are slightly less than the values for $MAPbI_3$. It has been suggested that the band structure of perovskite material can be described by a simple semi-empirical two band **k.p** Hamiltonian approach [Even 2015]. Assuming the effective mass for valence and conduction band are the same which predicts that the

binding energy and reduced mass scale linearly with the bandgap. Consider the bandgap of $Cs_{0.05}(MA_{0.17}FA_{0.83})_{0.95}Pb(I_{0.83}Br_{0.17})_3$ is less than $MAPbI_3$, our finding on $Cs_{0.05}(MA_{0.17}FA_{0.83})_{0.95}Pb(I_{0.83}Br_{0.17})_3$ is in a good agreement with our previous work [Galkowski 2016].

3.4 Conclusions

In this chapter, we have investigated the relationship between excitonic properties and microstructure of the $MAPbI_3$ and $Cs_{0.05}(MA_{0.17}FA_{0.83})_{0.95}Pb(I_{0.83}Br_{0.17})_3$ perovskite using magneto-transmission spectroscopy. At low temperature, the excitonic binding energy and reduced mass are the same for each sample with a variety of crystal grain size. Thus, we conclude that microstructure truly play a negligible role in the exciton properties of mixed organic-inorganic lead halide-based perovskites, regardless of the thin film deposition technique and final morphology. This confirms the hypothesis, that the wide range of exciton binding energies found in the literature [D'Innocenzo 2014a] cannot be attributed to different morphologies or grain sizes.

Chapter 4

Magneto-reflectivity on single crystal $MAPbI_3$

Contents

This chapter presents the results of a magneto-reflectivity investigation of a $MAPbI_3$ single crystal. We have determined the binding energy of the exciton in the low (orthorhombic) and high temperature (tetragonal) phases to be $16 \pm 2\,meV$ and $12 \pm 4\,meV$, respectively. The binding energy of the exciton in the single crystal at low temperature is identical to that of the polycrystalline thin film, confirming the conclusion in Chapter 3 that the microstructure plays a negligible role in the excitonic properties of perovskite materials. Moreover, at room temperature, the binding energy of the exciton in $MAPbI_3$ single crystal is lower than the thermal energy, indicating a non-excitonic behavior. The results presented in this chapter have been published in J. Phys. Chem. Lett. ***8****, 1851-1855 (2017)*

4.1 Introduction

In this work, we have performed magneto-reflectivity studies on a millimeter size $MAPbI_3$ high quality single crystal. First, we describe the data and the analysis, which was performed to obtain the energies of the absorption resonance from the reflectivity spectra. We then deduce the exciton binding energy and reduced mass from the reflectivity measurements in the high magnetic field for both the low temperature orthorhombic, and the high temperature tetragonal phases.

Figure 4.1: A photo of single crystal $MAPbI_3$ sample. The scale bar is 2 millimeter.

4.1.1 $MAPbI_3$ single crystal

A single crystal of $MAPbI_3$ was grown by Dr. Amir-Abbas Haghighirad at the Clarendon Laboratory of the University of Oxford. The growth was performed from a small seed crystal in a supersaturated solution [Nayak 2016]. A photo of the single crystal used in our measurement is shown in Fig. 4.1. The sample has a lateral size of ≈4 mm with a ≈3 mm thickness. The single crystal character was confirmed by X-ray diffraction measurement performed by Dr. Amir-Abbas Haghighirad at the University of Oxford.

4.1.2 Data and analysis

We have performed magneto-reflectivity measurement on a $MAPbI_3$ single crystal using the reflectivity technique described in Section 2.3. In this configuration, the reflected signal from the single crystal is mixed with photoluminance (PL) emission. Since the reflectivity spectra have a dispersive shape, we first discuss the procedure, used to extract the energies of the absorption resonances from the reflectivity spectra.

A typical [0, 1] normalized reflectivity spectrum measured at 60 T and at 2 K is presented as a black line in Fig. 4.2. The $MAPbI_3$ single crystal exhibits strong PL emission even when illuminated with a broad band white light source, thus, the reflectivity spectrum is composed of both PL emission and the reflected light. To distinguish the PL and absorption in the reflectivity spectrum, we have performed PL measurement on the single crystal independently, with the same configuration as the reflectivity measurement. To do so, we simply change the excitation source from the broad band white light source to a laser emitting at 685 nm. The PL spectrum of the $MAPbI_3$ single crystal measured at the same magnetic field is presented as the red line in Fig. 4.2. Both reflectivity and PL spectra show a dominant peak around 1646 meV (marked as PL1), which originates from bound exciton recombination. In a lower energy range, two weaker peaks with energies around 1626 meV and 1612 meV are observed (marked as PL2, PL3), which probably originate from donor-acceptor bound exciton, as proposed by Diab et al. and Phuong et al. [Diab 2016,

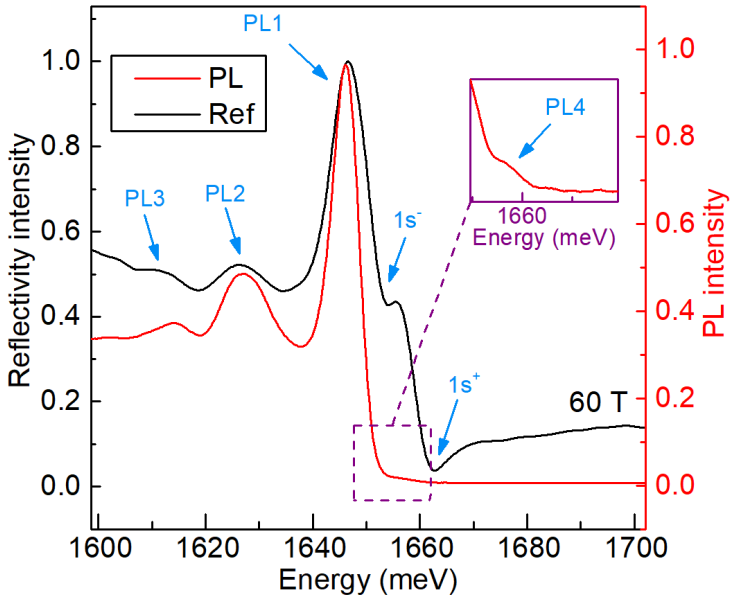

Figure 4.2: Typical normalized reflectivity (black line) and PL (red line) spectra of a single crystal measured in 60 T.

Phuong 2016]. In addition to these three peaks, a very weak peak (PL4) with a peak energy around 1658 meV is observed on the high energy side of PL1. To better see this feature, we show an expanded view of the PL spectrum in the inset of Fig. 4.2. The peak energy of PL4 (1658±1 meV) corresponds very well to the absorption energy of the $1s^+$ state (which will be discussed below). Thus, we deduce that PL4 originates from the high energy component of the Zeeman split exciton emission, while the lower energy component is immersed within the PL1 peak.

First we discuss the difference between PL and reflectivity spectra. The reflectivity spectrum clearly shows two minima on the high energy side of the PL1 peak, which are absent in the PL spectrum. This suggests that they come from the absorption resonance. In fact, these two minima correspond to the Zeeman split 1s exciton absorptions, as marked in Fig. 4.2. It is worth to mention that this is the first time we observe the Zeeman splitting of the 1s transition in $MAPbI_3$ perovskite material without using polarization optics. This is due to the extremely narrow linewidth of the 1s absorption in the single crystal (3.8 meV at 0 T, which is shown in the inset of Fig. 4.4(a)). This should be compared to the much larger value of 20-40 meV in $MAPbI_3$ polycrystalline films [Miyata 2015].

In transmission spectra, the minimum of the absorption line corresponds to the absorption energy, while the reflectivity spectra have a typical dispersive line shape, so the energy of the absorption corresponds to the position of the maximum slope (gradient) of the reflectivity dispersive curve [Cardona 2005]. To determine the absorption energy from the reflectivity spectrum, Korona et al. [Korona 1996] have

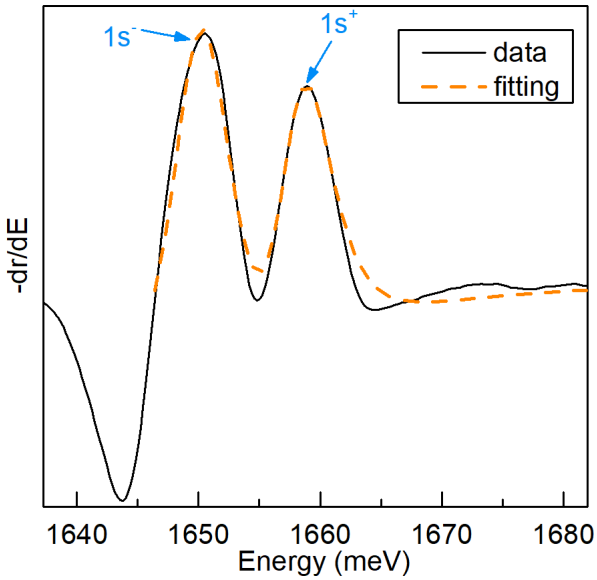

Figure 4.3: A negative differential reflectivity spectrum $(-dr/dE)$ is shown as black line. The orange dashed line shows the fit to the data.

proposed the following formula to fit the reflectivity data:

$$r(E) = r_0 + \sum_j A_j \Re\left(\frac{E_j - E + \mathrm{j}\Gamma_j}{\Gamma_j^2 + (E - E_j)^2} e^{i\theta_j}\right), \tag{4.1}$$

where r_0 is a constant indicating the total amplitude of the reflectivity signal (background), θ_j is a phase, A_j, E_j and Γ_j are the amplitude, energy and broadening parameter for each of the resonances.

A commonly employed method to analyze the reflectivity spectra is to calculate the derivative. This is mainly based on two reasons, (i) the reflectivity spectra have a dispersive line shape, so that the absorption energy is located at the gradient extreme of the reflectivity spectra. Calculating the derivative make the spectra easier to analyze. (ii) Some weak features are hardly observed in the as measured spectra. Calculating the derivative make the weak features more pronounced in the spectra. Thus, instead of fitting the reflectivity spectrum directly, we first calculate the negative derivative of the reflectivity spectrum, as shown with black line in Fig. 4.3. There are two dominant peaks corresponding to the two absorptions in Fig. 4.2. Then, we fit this spectrum with the negative derivative of Eq. 4.1, which is given by,

$$-\frac{dr}{dE} = r_0' + \sum_j A_j' \left(\frac{(\Gamma_j^2 - (E - E_j)^2)cos(\theta_j) + 2\Gamma_j(E - E_j)sin(\theta_j)}{(\Gamma_j^2 + (E - E_j)^2)^2}\right), \tag{4.2}$$

where r_0' and A_j' indicate the background and amplitude for the negative differential spectra. The fitting curve is shown as violet dashed line in Fig. 4.3. We limit

the fitting to the range from 1646 meV to 1680 meV, which covers the two resonances. The absorption energies determined from the fitting are 1650.0±0.5 meV and 1658.1±0.5 meV, which are identical to the energy in the maximum of the peaks. Thus, we conclude that, within experimental error, the peak position in negative derivative of the reflectivity spectra ($-dr/dE$) gives the same energies of the resonant absorption as those obtained from fitting formula 4.2 to the derivative of the data. In the following data analysis, we simply take the energy of the maximum in the negative derivative, rather than fitting the differential reflectivity spectrum.

4.2 Magneto-reflectivity measurement on single crystal $MAPbI_3$

In this section, we show the results of the magneto-reflectivity measurement on $MAPbI_3$ single crystal at both low temperature (2 K) and high temperature (168 K), and the results of temperature dependence reflectivity measurements. The measurements were performed at LNCMI-T using a long magnetic pulse technique. The detailed experimental setup is introduced in the section 2.3.

4.2.1 Low temperature magneto-reflectivity

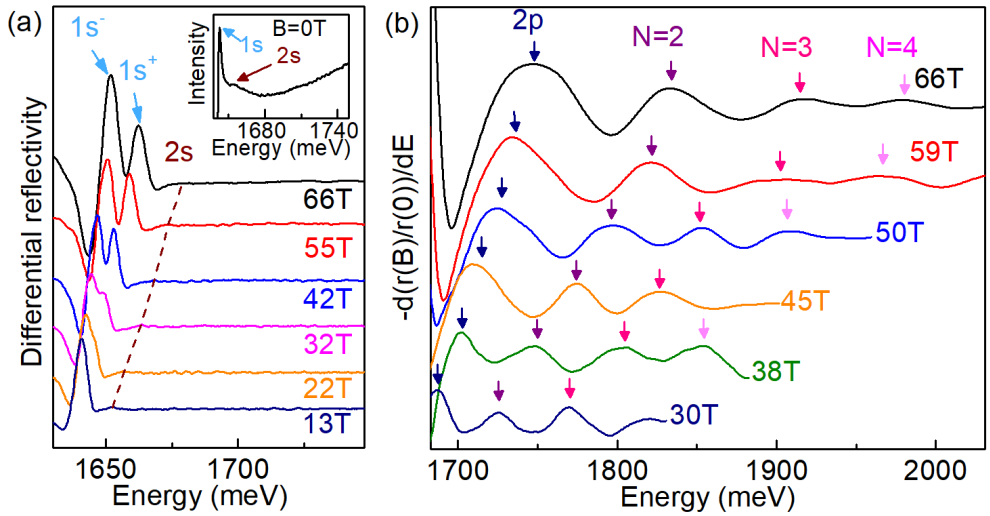

Figure 4.4: (a) Differential reflectivity spectra measured at indicated magnetic field values at 2 K. The arrows mark the absorption peaks. Inset: As-measured reflectivity spectrum at zero magnetic field. (b) High magnetic field differential reflectivity spectra after normalization by zero-field reflectivity. Arrows of the same colors indicate the transition between the same Landau levels.

A full set of the differential magneto-reflectivity spectra measured at 2 K are shown in Fig. 4.4(a) for the magnetic field up to 66 T. At low magnetic field, the dominant peak at 1640 meV corresponds to the 1s excitonic transition. The Zeeman

splitting of the 1s state becomes visible around 32 T. On the higher energy side of the 1s peak, an additional weak absorption peak is attributed to the transition of the 2s excitonic state. To observe additional absorption peaks in the higher energy range, we first divided the measured spectra at high magnetic field by the zero-field spectrum. In such way, we obtained the ratio spectra. Then, in order to obtain the correct transition energies at the maxima of the peaks, we calculated the negative derivative of the ratio spectra, as presented in Fig. 4.4(b). One excitonic transition (2p) and three interband transitions between Landau levels in the conduction and valence bands ($N = 2, 3, 4$) are observed. Note that the 2p excitonic transition is forbidden at zero magnetic field, but becomes dipole allowed at high magnetic field once the cyclotron energy exceeds the exciton binding energy [Makado 1986].

In the inset of Fig. 4.4(a), we show the reflectivity spectrum measured at zero magnetic field. We clearly observe 1s and 2s excitonic transitions, as marked in the insert. However, in the $MAPbI_3$ polycrystalline thin films, the 2s excitonic transition is absent at zero magnetic field, and only starts to be visible in high magnetic field [Miyata 2015]. This is due to the fact that $MAPbI_3$ polycrystalline thin films exhibit a lower crystal quality, resulting in a much broader linewidth of the 1s excitonic transition, which prevents the observation of the 2s excitonic transition. This phenomenon is consistent with the results obtained for other materials, such as $MAPbBr_3$. Galkowski at al. [Galkowski 2016] did not observe 2s excitonic transition in $MAPbBr_3$ polycrystalline thin films, while the 2s excitonic transitions are clearly observed by Tilchin et al. [Tilchin 2016] in the reflectivity spectra of a $MAPbBr_3$ single crystal.

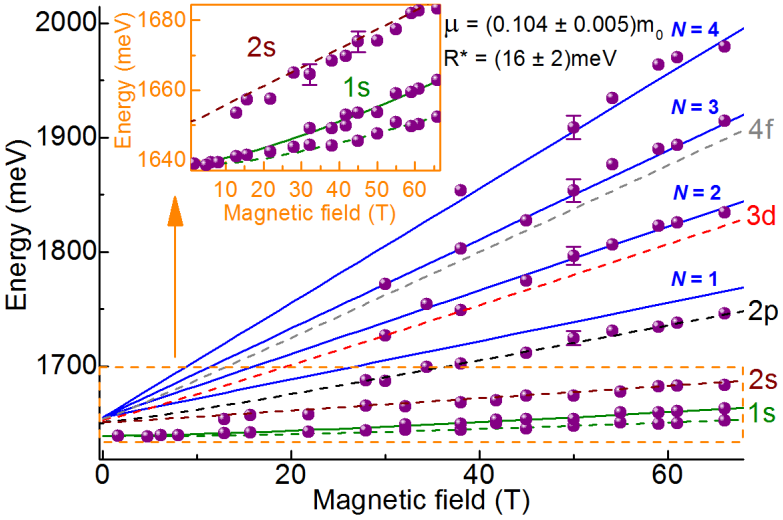

Figure 4.5: Energies for excitonic and Landau level transitions as a function of the applied magnetic field at 2 K (symbols). Blue solid lines are the results of a linear fit of the interband transition between Landau levels in the valence and conduction bands. Dashed lines result from the fit of the hydrogen-like transitions. Inset: Expanded view of the low-energy transitions.

To analyze the data, we plot the energy of the absorption as a function of the magnetic field, as presented in Fig. 4.5. We fit the data using the same models discussed as Chapter 3, namely, the dashed lines present the fit of the hydrogen-like transitions in magnetic field based on the work of Makado and McGill [Makado 1986]. The results of linear fits of the interband transition between Landau levels are presented as blue solid lines. The three excitonic transitions and three inter-Landau level transitions allow us to precisely determine the exciton binding energy and the reduced mass. The splitting of the 1s excitonic transitions is included in this model by adding the Zeeman term ($\pm g_{eff}\mu_B B/2$) to the excitonic transition energies, where g_{eff} and μ_B are the effective g-factor and Bohr magneton. The energy splitting increases linearly with the magnetic field, which gives an effective g factor $g_{eff} = 2.6 \pm 0.1$. This value is slightly larger than previously found ($g_{eff} = 1.72 \pm 0.05$) by Tanaka et al. [Tanaka 2003b], possibly due to the improved resolution of our measurement. It is, however, quite similar to the previous results of our group ($g_{eff} = 2.3 \pm 0.1$) obtained on $MAPbI_{3-x}Cl_x$ thin film sample [Galkowski 2016].

The fitting of the exciton and free carriers transitions allows us to conclude that at 2 K the reduced mass and the exciton binding energy are $(0.104 \pm 0.005)\, m_0$ and (16 ± 2) meV, respectively. It is important to note that the exciton binding energy obtained from the single crystal is identical to that of polycrystalline thin films discussed in Chapter 3. This result confirms the conclusion in Chapter 3 that the crystal grain sizes play a negligible role on the exciton binding energy for perovskite materials.

The exciton binding energy from our result is significantly smaller than previously reported (37-50 meV) from the magneto-optical studies on $MAPbI_3$ polycrystalline thin films, where only the 1s excitonic state was observed [Hirasawa 1994, Tanaka 2003a]. We attribute this difference to the much poorer resolution of the excitonic transitions and the underestimation of the value of the dielectric constant in the previous study [Tanaka 2003a]. In this work, the authors assumed that the exciton binding energy is much larger than the energies of the optical phonon modes, so that the dielectric screening is not influenced by the lattice vibration. Thus, the authors used the high frequency dielectric constant ($\epsilon_{eff} = 6.5$) to calculate the exciton binding energy [Tanaka 2003a]. However, recent Raman scattering experiment shows that optical phonons have energies from 8 meV (vibration of the inorganic cage) to 16 meV (libration of the organic cation) [Quarti 2013]. This suggests that the dielectric screening is enhanced by the lattice vibration, and consequently a value intermediate between the static $\epsilon_0 = 25.7$ [Wehrenfennig 2014] and the high frequency $\epsilon_\infty = 5.6$ [Brivio 2014, Umari 2014] dielectric constant should be used [Even 2014b]. Our values of the exciton binding energy and reduced mass suggest a dielectric constant $\epsilon_{eff} \approx 9.4$, which is indeed intermediate between the low and high frequency values, as expected. Our results are also in a good agreement with the exciton binding energy of 15 meV deduced by Even et al. by fitting a zero field exciton absorption spectrum [Even 2014b].

4.2.2 Temperature dependence reflectivity

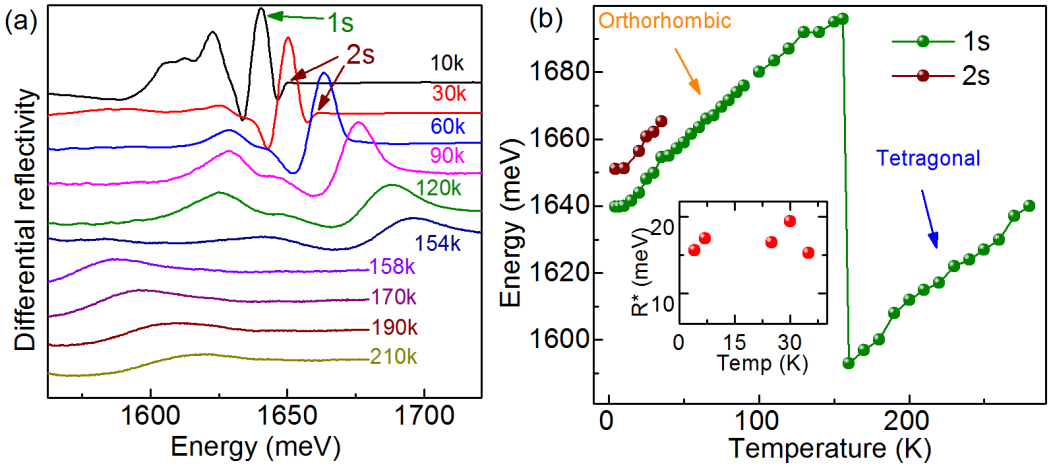

Figure 4.6: (a) Differential reflectivity spectra measured at different temperatures. (b) 1s (green circle) and 2s (red circle) transition energy as a function of the temperature. Inset: Exciton binding energy (estimated here from the 1s-2s splitting) as a function of the temperature.

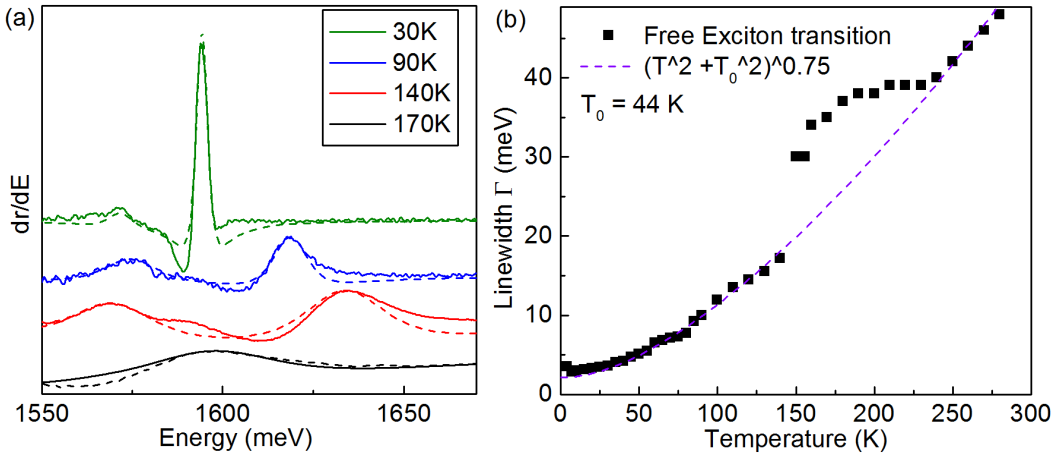

Figure 4.7: (a) The examples of the differentiate reflectivity fitted using Eq. 4.2 at different temperatures. Solid lines are the differentiate reflectivity spectra, dashed lines present the fitted responses. (b) The broadening Γ of free exciton transitions as a function of temperature determined from the fitting of temperature dependence differentiate reflectivity spectra.

The practical application of perovskite based solar cell devices requires a knowledge of the electronic properties of the high temperature tetragonal phase of these materials. We first measured the temperature dependence of the reflectivity spectra of the single crystal. Fig. 4.6(a) shows the typical differential reflectivity spectra at

the indicated temperature. The 1s transition appears as a pronounced peak, while the 2s transition appears as a small shoulder on the high energy side of the 1s transition. Due to the excellent crystalline quality, both 1s and 2s transition are observed at temperatures as high as 35 K. The 1s and 2s transition energies as a function of temperature are represented in Fig. 4.6(b). The 1s and 2s transitions both exhibit a similar trend, blue shifting with increasing temperature. This blue shift is common in perovskite materials [Wu 2014], in contrast to the majority of semiconductors materials, which show a red shift of the band gap energy with the increasing temperature [Varshni 1967]. The blue shift observed for $MAPbI_3$ originates from the increased separation between the band extrema (band gap) with increasing temperature [Huang 2013, Singh 2016]. As discussed in Section 1.3.1, the band gap energy of $MAPbI_3$ is significantly reduced by the spin-orbit interaction. Since $MAPbI_3$ has a large volume coefficient for thermal expansion (50 times more than crystalline silicon), when the temperature increases, the spin-orbit interactions within the inorganic lattice are significantly weakened, resulting in an increase of the separation between the band extrema.

It is possible to deduce the binding energy R^* from the 1s and 2s transitions, since the energy separation of 1s and 2s gives the $0.75R^*$, as expected from Eq. 1.17. The deduced R^* as a function of temperature is shown in the inset of Fig. 4.6(b). The deduced R^* does not show any temperature dependence up to 35 K. This is expected, since there is no structural phase transition for $MAPbI_3$ in the temperature range from 4 K to 35 K, so that the exciton binding energy should remain the same.

The phase transition in the thin film $MAPbI_3$ from orthorhombic to tetragonal phase occurs about 150 K [Baikie 2013] and is accompanied by a dramatic red shift of the bandgap ($\sim$100 meV) [D'Innocenzo 2014a, Even 2014b, Yamada 2015]. In our case, around 154 K, there is a abrupt transition to a lower energy, red-shifted by 103 meV. This suggests that the sample has completed the transition from the low temperature orthorhombic to the high temperature tetragonal phase.

We have also studied the broadening parameter Γ of the free exciton absorption line as a function of temperature, by fitting the temperature dependence differential spectra with Eq. 4.2. Examples of the fitted spectra are shown in Fig. 4.7(a). Solid lines show the measured differential reflectivity spectra, while the dashed lines present the fit. Fig. 4.7(b) shows the broadening parameter Γ as a function of the temperature. Schreiber et al. [Schreiber 1982] have investigate the influence of lattice vibration on the absorption line shape of the excitons. They suggest that, for different dimension of the crystal lattice, the absorption line shape of the excitons exhibit different temperature dependence. In other words, the broadening parameter of the exciton absorption depends on the temperature as $T^{2/3}$, T and $T^{3/2}$ for one-, two- and three-dimensional crystal lattices, respectively [Schreiber 1982]. In our case, apart from the temperature region of the phase transition (orthorhombic/tetragonal), Γ shows a $T^{3/2}$ dependence, with a residual broadening parameter of 3.6 meV (44 K) at low temperature. According to Schreiber's work, this temperature dependence is in a good agreement with the three dimensional crystal lattice of $MAPbI_3$ perovskite. In the temperature region of the phase transition,

an additional broadening is observed. This may due to the fact that the phase transition induces an additional distortion in the crystal structure, which leads to an additional inhomogeneous broadening.

4.2.3 High temperature magneto-reflectivity

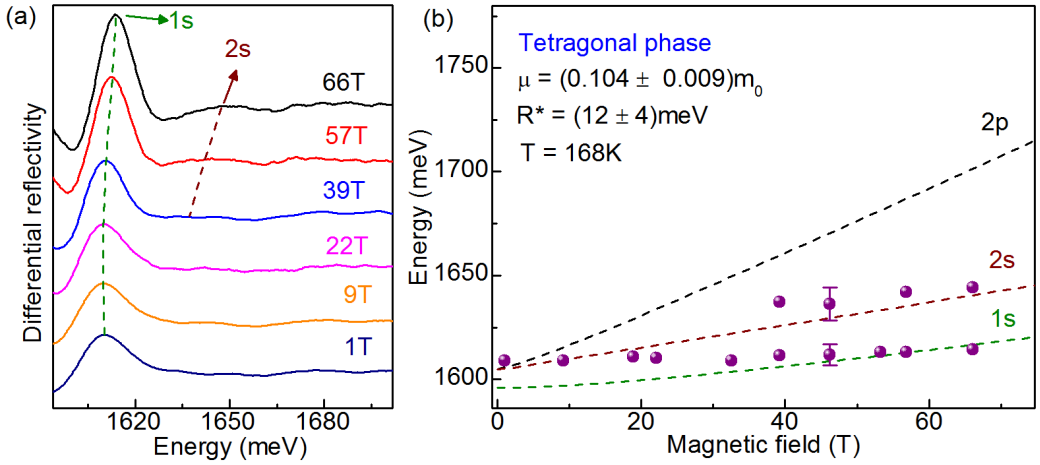

Figure 4.8: (a) Magneto-reflectivity spectra measured at T=168 K differentiated with respect to energy. (b) High-temperature energy fan chart. The dashed lines indicate hydrogenic transitions.

To study the electronic property of the $MAPbI_3$ single crystal in the tetragonal phase, we repeat the magneto-reflectivity measurement at 168 K. The differential reflectivity spectra measured up to 66 T are shown in Fig. 4.8(a). The 1s excitonic states appears as a pronounced peak in the reflectivity spectrum with a considerable broadening (FWHM of 22 meV). The 2s states appear as a shallow peak at magnetic fields higher than 39 T. However, at such a high temperature, no higher excitonic or Landau levels transition are observed. Fig. 4.8(b) represents the energy fan chart at 168 K. We have fitted the data for the 1s and 2s transition. From our previous work [Miyata 2015], the reduced masses of thin films perovskite remain almost the same for both orthorhombic phase and tetragonal phase. Thus, we assume that reduced mass of single crystal at tetragonal phase is the same as at low temperature, $\mu \simeq 0.104\, m_0$. With the same fitting procedure described for Fig. 4.5, we find an exciton binding energy of 12±4 meV comparable to that estimated by similar high temperature magneto-transmission experiments on a thin film [Miyata 2015]. The value of exciton binding energy decreases by few meV when going from the orthorhombic phase to the tetragonal phase. This is consistent with the fact that the phase transition increases the dynamic disorder related to the rotational motion of the organic cation, resulting in an increase of the dielectric constant [Poglitsch 1987, Even 2014b].

Whilever the $MAPbI_3$ remains in the tetragonal phase, the dielectric response does not change, so we assume that the exciton binding energy remains unchanged

in tetragonal phase independent of the temperature. The thermal energy at room temperature is $\approx 26\,\text{meV}$, which is larger than the exciton binding energy in the single crystal. In this case, the electrons and holes in excitons are dissociated by the thermal energy at room temperature, which suggests that the free carriers (rather than excitons) are dominant in the single crystal at room temperature.

4.3 Conclusions

We performed magneto-reflectivity measurement on a high quality $MAPbI_3$ single crystal. The value of the exciton binding energy and effective reduced mass of the single crystal sample at low temperature are identical to that of polycrystalline thin film sample. The estimated value of exciton binding energy of single crystal sample in tetragonal phase is smaller than the thermal energy at room temperature, indicating that $MAPbI_3$ shows non-excitonic behavior at room temperature, which is important for the photovoltaic applications.

Chapter 5

Magneto-transmission on $CsPbX_3$

Contents

*In this chapter, we describe the results of the spectroscopic measurements of the fully inorganic $CsPbX_3$ perovskites. The temperature dependence of the absorption indicates the absence of a structural phase transition for all the investigated materials, up to room temperature. By performing the magneto-transmission measurements, we determine the binding energy and the reduced mass of the excitons in $CsPbX_3$. The results presented in this chapter have been published in ACS Energy Lett., **2 (7)**, 1621-1627 (2017).*

5.1 Introduction

It has been recently demonstrated that introducing small amount of inorganic-cesium cations into the organic lattice of the hybrid perovskite (e.g. $Cs_{0.05}(FA_{0.83}MA_{0.17})_{0.95}Pb(I_{0.83}Br_{0.17})_3$) greatly improves their properties resulting in a superior morphology, high solar cell efficiency and improved stability under standard operation conditions [Saliba 2016b, Saliba 2016a, McMeekin 2016]. Despite the impressive performance of the mixed cation perovskite, very little is known about the influence of the inorganic cesium cation on the electronic properties of the mixed compounds. In order to answer this question, we have investigated the electronic properties of fully inorganic $CsPbX_3$ perovskites.

We present the results of optical studies of the electronic properties of fully inorganic $CsPbX_3$ thin films, where X = Br, I or an alloy of the two. The temperature dependence of the absorption measurements suggest that $CsPbX_3$ does not undergo

a structural phase transition in the range from 4 K to 270 K, which is in striking contrast with organic-inorganic perovskites. We also performed magneto-transmission measurements to determine the binding energy and reduced mass of the exciton in $CsPbX_3$. By comparing the dielectric constant of both hybrid and fully inorganic perovskites, we show that, at low temperature, the dielectric screening is essentially the same for both hybrid and inorganic materials and is mainly dominated by the relative motion of the atoms within the lead halide cage.

5.2 Description of the samples and pre-experimental treatment

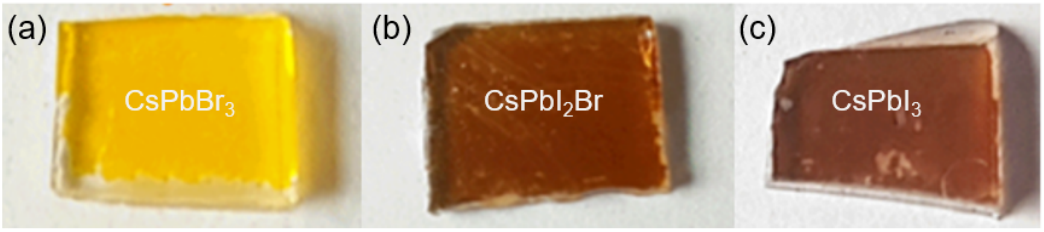

Figure 5.1: (a)-(c) Photos of the annealed $CsPbBr_3$, $CsPbI_2Br$ and $CsPbI_3$ samples, respectively.

$CsPbX_3$ samples were fabricated by Rebecca J. Sutton in the Clarendon Laboratory of the University of Oxford. In total, we have measured three different compounds, namely, $CsPbBr_3$, $CsPbI_2Br$ and $CsPbI_3$. They are polycrystalline thin films deposited on glass microscope slides.

Before we introduce the pre-experimental treatment, we first discuss the basic properties of the three materials. $CsPbI_3$ is known to be unstable under ambient conditions. This is mainly due to the fact that, the small size of the Cs^+ cation results in a tolerance factor too low to sustain a cubic perovskite structure. In fact, it has a "black" cubic perovskite phase with a band gap of around 1.73 eV (stable above $\approx$ 593 K) and a "yellow" non-perovskite phase with a band gap of around 2.8 eV at room temperatures [Vorpahl 2015, Eperon 2015]. At room temperature and in air, a full conversion for $CsPbI_3$ from the black phase to the yellow phase completes within a few minutes, or almost immediately in a humid environment. It has been shown that $CsPbI_2Br$ is significantly more stable in the cubic phase than their fully iodide counterparts [Ma 2016]. This is mainly because Br^- has a smaller ionic radius than I^-, resulting in a higher tolerance factor for $CsPbI_2Br$ than $CsPbI_3$. $CsPbI_2Br$ starts to exhibit a cubic phase with a band gap of 1.9 eV above 338 K [Niezgoda 2017]. Below this temperature, $CsPbI_2Br$ covert to a non perovskite phase within 10 min. $CsPbBr_3$ is even more stable. Indeed, it does not have a non-perovskite phase. This compound can crystallize in three different structure, namely, orthorhombic, tetragonal and cubic. All of these three polymorphs have a perovskite structure [Sakata 1979], and a similar band gap in the range of

2.3-2.4 eV, corresponding to their orange color [Kulbak 2015]. This compound has a phase transition from the orthorhombic phase to a tetragonal phase at 361 K, and a further phase transition to a cubic phase at 403 K. [Kulbak 2015, Stoumpos 2013b].

Due to their limited stability in air at room temperature [Eperon 2015], $CsPbX_3$ samples were systematically annealed before the experiment. The aim of this annealing procedure is to recover the cubic perovskite phase for all the compounds, because $CsPbX_3$ compounds with cubic phase is of interest for their potential in photovoltaic devices, as described in Section 1.4. Initially, $CsPbI_3$ and $CsPbI_2Br$ are transparent, due to the fact that they are in a non-perovskite phase and have a bandgap near the UV range. $CsPbBr_3$ has a yellow color, due to the fact that it is in an orthorhombic phase with a band gap in 2.3-2.4 eV. The temperatures of the phase transition for these three compounds are different (as discussed above), thus, they are annealed at different temperatures. $CsPbI_3$ was annealed at 623 K for 10 min. $CsPbI_2Br$ and $CsPbBr_3$ were annealed at 523 K for 5-7 min. Fig. 5.1(a-c) presents the photos of $CsPbBr_3$, $CsPbI_2Br$ and $CsPbI_3$ after annealing procedure. After annealing, $CsPbBr_3$ shows a yellow color suggesting a band gap in the range of 2.3-2.4 eV, however the crystal structure of annealed $CsPbBr_3$ is hard to specify from the color. $CsPbI_2Br$ and $CsPbI_3$ exhibit a brown color suggesting the band gap in the range of 1.7-1.9 eV. After annealing, the samples were immersed in liquid helium in a cryostat within 4 minutes.

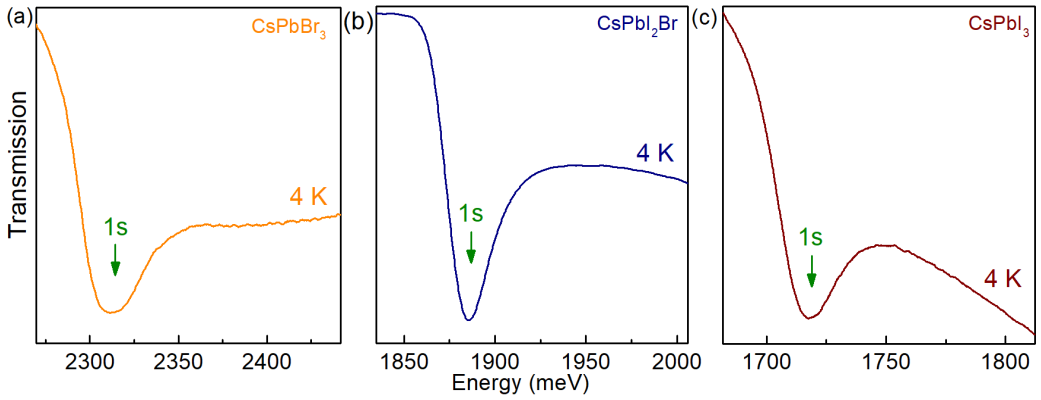

Figure 5.2: (a)-(c) Transmission spectra measured at 4 K for annealed $CsPbBr_3$, $CsPbI_2Br$ and $CsPbI_3$ sample, respectively.

In Fig. 5.2(a-c), we show the typical transmission spectra measured at 4 K of annealed $CsPbBr_3$, $CsPbI_2Br$ and $CsPbI_3$ samples, respectively. All the spectra show a clear minimum corresponding to the 1s excitonic absorption. The absorption energies of $CsPbI_3$ and $CsPbI_2Br$ are around 1.72 and 1.87 eV, suggesting that they are in a black perovskite phase (cubic phase) [Beal 2016]. In the case of $CsPbBr_3$, the absorption energy is around 2.32 eV, suggesting that the $CsPbBr_3$ is also in a perovskite phase. As described before, after annealing, the samples were directly put into liquid helium (4 K), and this procedure freezes the crystal structure. Therefore, we conclude that the sample pre-treatment procedure preserves the perovskite

structure obtained from annealing.

5.3 Temperature dependent transmission measurement

After the pre-treatment of the samples, we measured the absorption of all the $CsPbX_3$ compounds as a function of the temperature, using the transmission technique described in Section 2.2.

In Fig. 5.3(a-c), we show typical transmission spectra of $CsPbBr_3$, $CsPbI_2Br$, $CsPbI_3$ measured over a wide range of temperatures varying from 4 K to 270 K. Each transmission spectrum shows a clear, single minimum, which corresponds to the 1s excitonic absorption. The minimum blue shifts and broadens with increasing temperature for all the compounds. We plot the energy of the minimum of the absorption resonances as a function of the temperature in Fig. 5.3(d). The absorption energies shift continuously with increasing temperature. In organic-inorganic perovskite materials, the structural phase transition is always accompanied by a dramatic band gap energy change [Stoumpos 2013a, Baikie 2013, Galkowski 2017]. Thus, the continuous shift of the band gap as a function of the temperature suggests that there is no structural phase transition in $CsPbX_3$. This phenomenon is in stark contrast with the hybrid organic-inorganic perovskites. In the temperature range of 4 K-300 K, the hybrid organic-inorganic perovskites exhibit a structural phase transition around 150 K-170 K from low temperature orthorhombic to high temperature tetragonal phase [Stoumpos 2013a, Baikie 2013].

All three polymorphs (orthorhombic, tetragonal and cubic phases) of $CsPbBr_3$ exhibit similar band gaps and a yellow color. Simply from the color and the band gap energy, it is hard to specify the exact polymorph for the annealed $CsPbBr_3$. After annealing and putting the sample into the helium cryostat, the measured $CsPbBr_3$ can be in any of the three polymorohs. In order to check which polymorph we have measured, we compared the results for annealed and non-annealed $CsPbBr_3$. The transmission spectra and absorption energy of the annealed $CsPbBr_3$ sample are presented as black dashed lines and spheres in Fig. 5.3(a), (d). The transmission data and the evolution of the absorption energy with the temperature are identical for annealed and non-annealed $CsPbBr_3$. Non-annealed $CsPbBr_3$ is in an orthorhombic phase [Beal 2016], suggesting that annealed $CsPbBr_3$ is in an orthorhombic phase as well. Thus, we conclude that, the annealing procedure does not influence the crystal structure of $CsPbBr_3$ under the measurement condition used.

The absence of the phase transition in the $CsPbX_3$ compunds suggests that the electronic properties, such as exciton binding energy, will not change in the investigated temperature range, as we will demonstrate in Section 5.5.

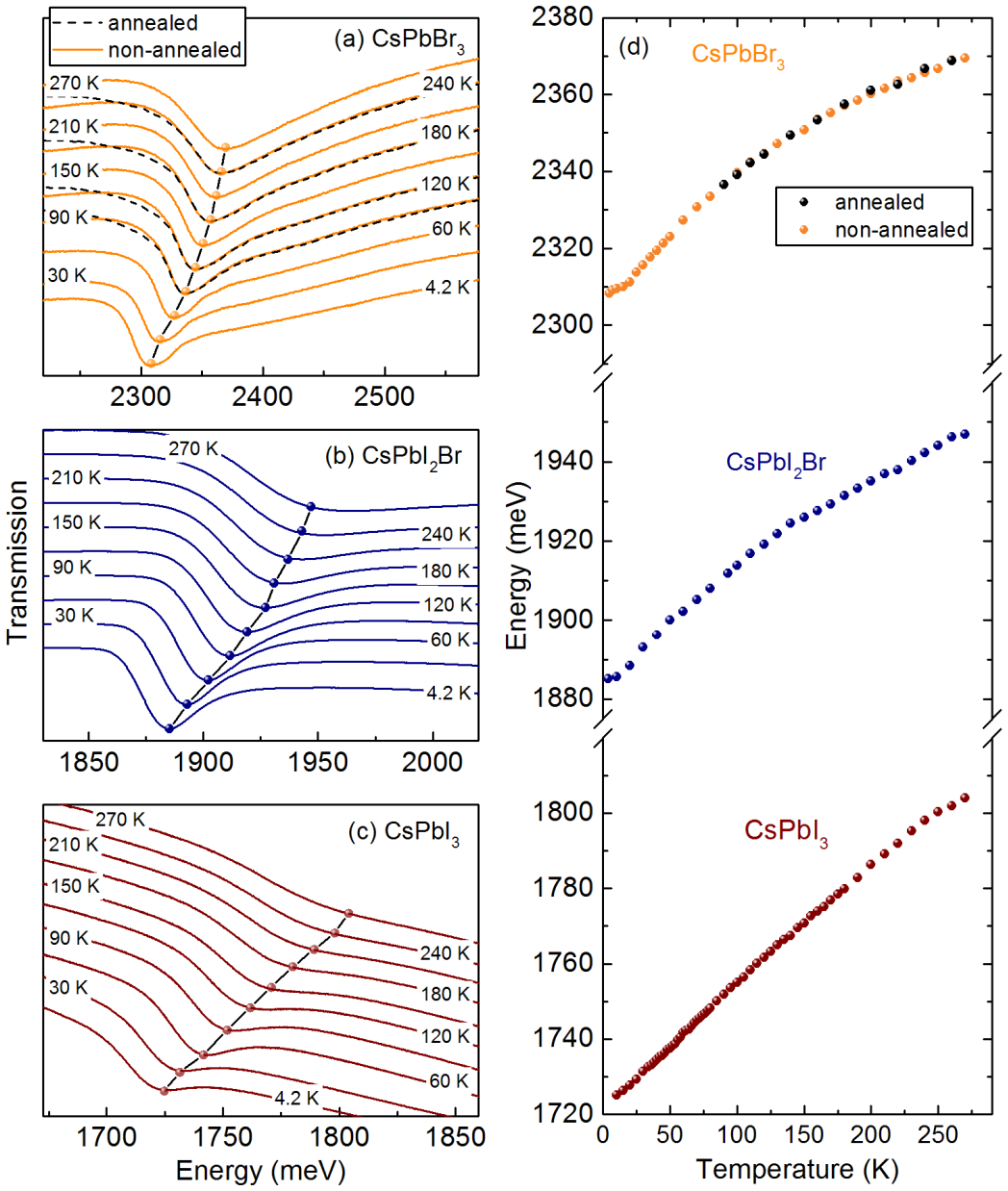

Figure 5.3: Typical transmission spectra of (a) $CsPbBr_3$, (b) $CsPbI_2Br$ and (c) $CsPbI_3$ sample measured at different temperatures. Circle symbols represent the evolution of the 1s absorption with temperature. (d) Energies of the 1s transitions as a function of temperature for all three compounds. The black dashed lines and orange solid lines in panel (a) represent the spectra of annealed and as prepared $CsPbBr_3$. The black and orange circles in panel (d) represent the energies of 1s transitions for annealed and as prepared $CsPbBr_3$.

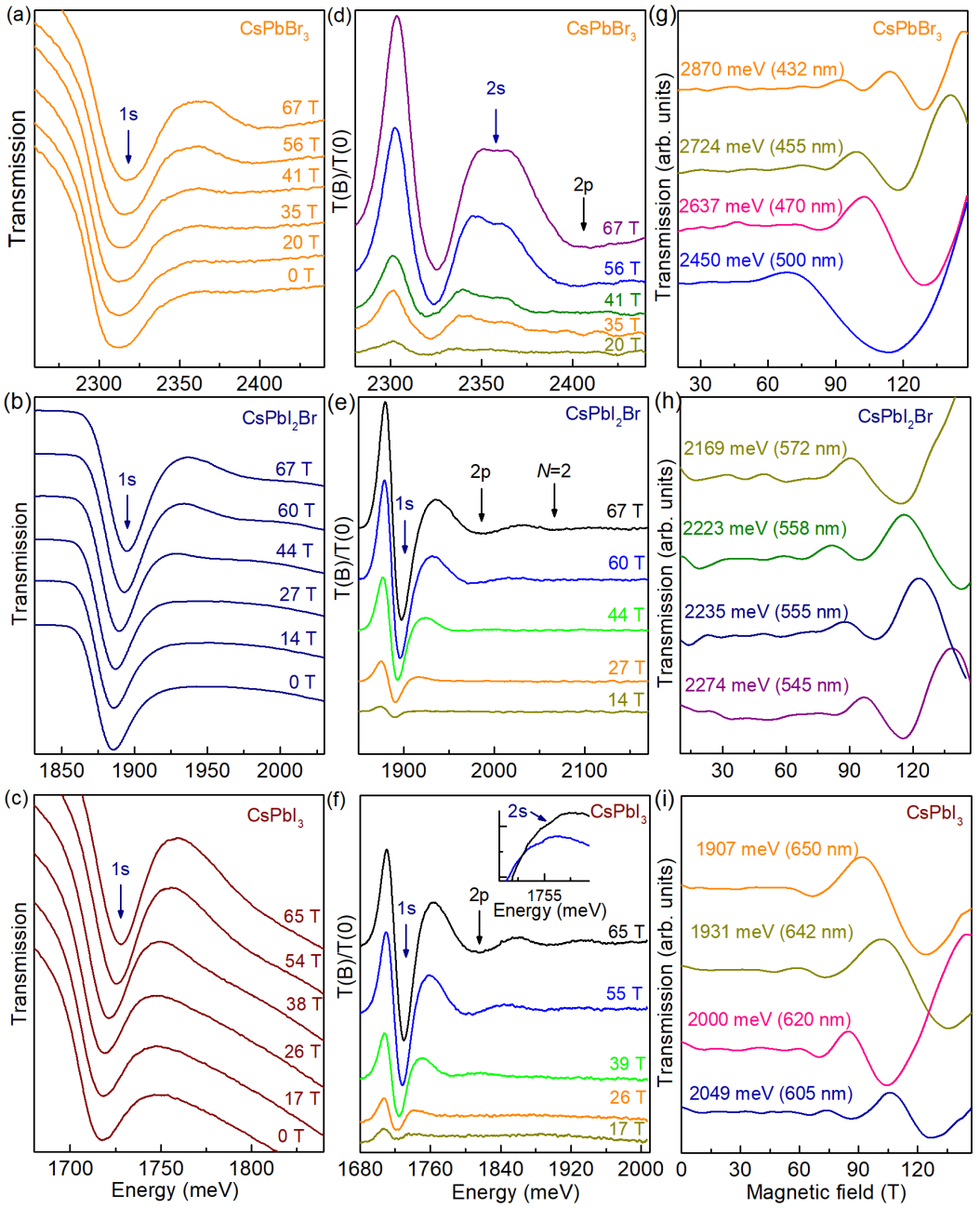

Figure 5.4: (a)-(c) Transmission spectra measured at the indicated magnetic field values for all the three compounds. (d)-(f) Transmission spectra in magnetic field divided by the zero field spectrum for three compounds. (g)-(i) Monochromatic transmission as a function of magnetic field for three compounds obtained by the short pulse technique performed by A. Miyata. The measurements were performed at 2 K.

5.4 Low temperature magneto-transmission measurement

We have performed low temperature magneto-transmission spectroscopy to investigate the electronic properties for $CsPbX_3$ compounds, using long pulsed magnetic

field techniques as described in detail in chapter 2. The results are presented and discussed below.

5.4.1 Typical results and data analysis

Typical magneto-transmission spectra measured at 2 K for $CsPbX_3$ are presented in Fig. 5.4(a)-(c). As for the organic-inorganic compounds, we observe a dominant minimum, which corresponds to the 1s excitonic transition. With the increase of the magnetic field, a blue shift of the 1s transition is observed for all the compounds. To observe the weaker absorption in the higher energy range, we divided the spectra at $B \geqslant 0$ T by the spectrum acquired at zero magnetic field, as shown in Fig. 5.4(d)-(f). We observed additional absorption minima at higher energies. To follow the higher energy transitions in an extended magnetic field range (70 T-150 T), A. Miyata has performed monochromatic absorption measurement via Mega Gauss technique for all the three compounds. Typical results are shown in Fig. 5.4(g)-(i). All the spectra show clearly a series of minima as a function of magnetic field, which correspond to the absorption at a given wavelength of the laser transmitted through the thin films.

We analyze the magneto-transmission data for all the Cs compounds in the same way as for $MAPbI_3$, as described in Chapter 3. Namely, we take the energy at the minimum of the absorption line and construct the energy fan chart for $CsPbI_3$, $CsPbI_2Br$ and $CsPbBr_3$. Typical results are shown in Fig. 5.5(a)-(c). The blue circles represent the data from long pulse measurements, while the black stars represent the data from Mega Gauss measurements performed by A. Miyata. We fit the excitonic transition data in the low energy range with the hydrogen model, as described in detail in Section 1.6.3. For the higher energy range data, we used the formula corresponding to interband transition between the Landau level in the conduction and valence band, as described in details in Section 1.6.2. The orange lines present the fit for the excitonic transitions. The gray lines present the fit for interband transition between Landau levels. We highlight the fit of 1s-2s excitonic transitions by plotting an expanded view of the low field and low energy portion of the fan chart in the panels below the full energy fan chart. The values of the effective mass μ and binding energy R_y^* obtained by the fitting procedure for all three compounds are marked in each figure and summarized in Table 5.2. Note that the exciton binding energy in $CsPbI_2Br$ (22 ± 3 meV) is less accurate than that of $CsPbBr_3$ (15 ± 1 meV) and $CsPbI_3$ (33 ± 1 meV). This is because we observed the 2s state for $CsPbBr_3$ and $CsPbI_3$. The energy difference between 1s and 2s state gives a strong constraint to the value of exciton binding energy. However, no trace of the 2s state for $CsPbI_2Br$ is observed, resulting in a less accurate value for the exciton binding energy in $CsPbI_2Br$.

In Fig. 5.6, we show the binding energy and reduced mass of the exciton in cesium compounds and organic-inorganic compounds as a function of the bandgap. Brown, red and yellow stars present the results for $CsPbI_3$, $CsPbI_2Br$ and $CsPbBr_3$. For comparison, we have added the results of the hybrid organic-inorganic perovskites

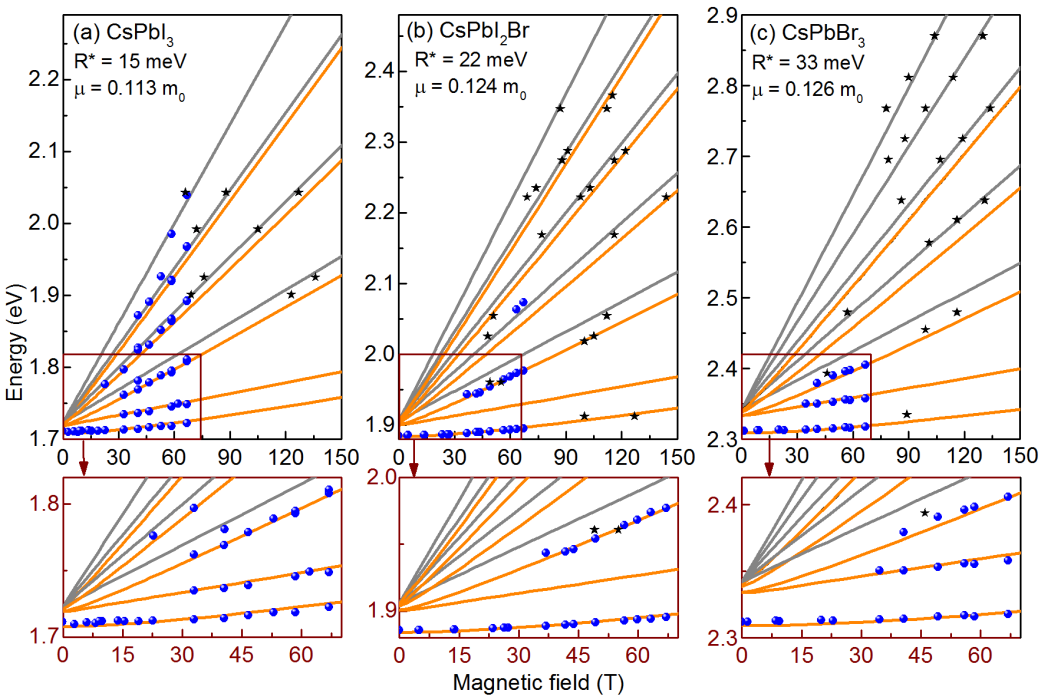

Figure 5.5: Transition energies of the excitons and free carriers as a function of the magnetic field at 2 K for (a) $CsPbI_3$, (b) $CsPbI_2Br$ and (a) $CsPbBr_3$. Circles represent the data from long pulse field measurement. Stars are the data from the Mega Gauss measurement performed by A. Miyata. Orange and gray lines are the results of the fit of the hydrogen-like transition and the interband transition between Landau levels. The lower panels show the zoom-in view of the low field and low energy portion of the fan chart.

from our group's previous work marked as circles [Miyata 2015, Galkowski 2016]. The pink and violet circles represent the results for FA and MA based hybrid perovskites. The evolution of exciton binding energy with the band gap is fitted with the equation $R^* = 0.010 \times E_g$, as shown as black line in Fig. 5.6(a). In Fig. 5.6(b), we observe an increase of the effective mass with the increasing of the band gap. This can be understood in the frame of a simple two band $\mathbf{k}\cdot\mathbf{p}$ model [Heo 2013]. Assuming the effective mass for valence and conduction band are the same, the reduced mass of the exciton can be written as,

$$\frac{1}{\mu} = \frac{4|P|^2}{m_0 E_g}, \tag{5.1}$$

where $P = \langle \Psi_{\mathrm{VB}} | p_x | \Psi_{\mathrm{CB}} \rangle$ is the momentum matrix element that couples states in the conduction and valence bands. $2|p|^2/m_0$ is the Kane energy [Makado 1986]. The theoretical predictions of the Kane energy are in the range 5.3-6.3 eV for these materials [Even 2014b, Fang 2015]. The evolution of the reduced mass with the band gap is fitted with the Kane energy of 8.3 eV, only slightly larger than theo-

Table 5.1: Parameters determined from the fit of the energy fan chart for $CsPbX_3$ at 2 K.

Compound	Phase	E_g (meV)	R^* (meV)	μ (m_0)
$CsPbI_3$	cubic	1723	15 ± 1	0.114 ± 0.01
$CsPbI_2Br$	cubic	1906	22 ± 3	0.124 ± 0.02
$CsPbBr_3$	orthorhombic	2342	33 ± 1	0.126 ± 0.01

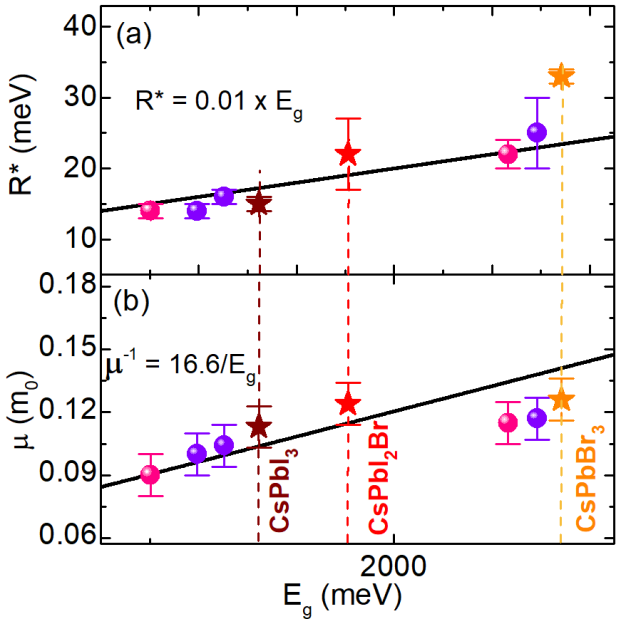

Figure 5.6: (a) Binding energy and (b) effective mass as a function of the band gap. Brown, red and yellow stars present the results for $CsPbI_3$, $CsPbI_2Br$ and $CsPbBr_3$. Pink and violet circles represent the results for the FA and MA based hybrid perovskites, from our previous work [Miyata 2015, Galkowski 2016].

retical predictions. The discrepancy may come from the different value of effective mass used in the model.

5.4.2 Dielectric screening

With the value of the effective mass and binding energy of the exciton, the effective dielectric constant of the materials can be calculated using,

$$\epsilon_{eff} = \frac{e^2}{\hbar}\sqrt{\frac{\mu}{2R_y^*}}, \tag{5.2}$$

Using the values of the exciton effective mass and binding energy obtained from the fitting, we calculated the effective dielectric constants ϵ_{eff} for all the compounds,

which are summarized in Table 5.2.

Table 5.2: Calculated effective dielectric constant for $CsPbX_3$ at 2 K.

Compound	Phase	E_g (meV)	ε_{eff}
$CsPbI_3$	cubic	1723	10.0 ± 0.4
$CsPbI_2Br$	cubic	1906	8.6 ± 0.8
$CsPbBr_3$	orthorhombic	2342	7.3 ± 0.4

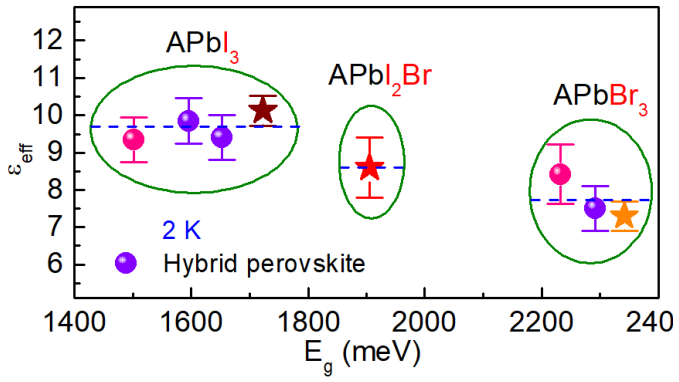

Figure 5.7: Dielectric constant as a function of the band gap. Brown, red and yellow stars present the results for $CsPbI_3$, $CsPbI_2Br$ and $CsPbBr_3$. Pink circles represent the results for the FA based hybrid perovskites, while the violet circles represent the results for the MA based hybrid perovskites.

In Fig. 5.7, we compared the effective dielectric constant for cesium-based perovskites (stars) with the hybrid organic-inorganic perovskites (circles) measured at 2 K. To understand the results, we first group the data in the way that data points from the same group have the same halide, and different A cation (MA, FA, Cs). The blue dashed lines indicate the average value of dielectric constant in each group. It is clear from the results that the dielectric constant does not change within the experimental error for a given lead-halide cage, regardless of the cation. It has been suggested that the main contributions to the dielectric screening are due to the Pb-X stretching modes and Pb-X-Pb rocking modes [Pérez-Osorio 2015, Sendner 2016]. This is consistent with what is observed in Fig. 5.7. At low temperature, when the organic cation motion is frozen, the dielectric mechanism is essentially the same for both hybrid and inorganic perovksites and is mainly dominated by the relative motion of atoms within the lead halide cage.

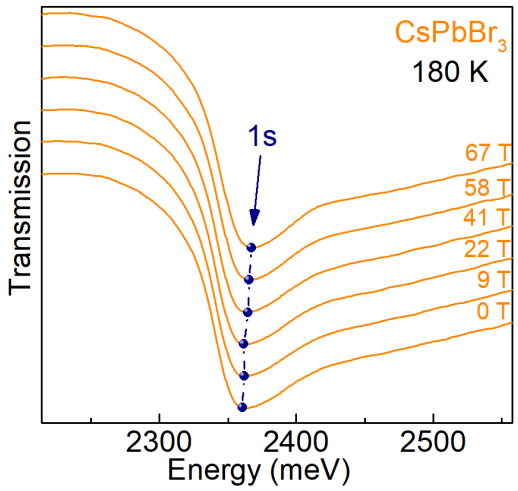

Figure 5.8: Transmission spectra measured at indicated magnetic field and at 180 K for $CsPbBr_3$.

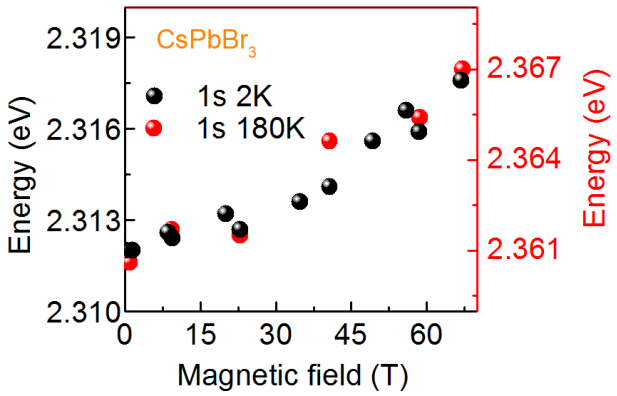

Figure 5.9: 1s transition as a function of magnetic field in $CsPbBr_3$ at two different temperature.

5.5 High temperature magneto-transmission measurement

We also performed magneto-transmission measurement on $CsPbBr_3$ at 180 K. Typical transmission spectra are shown in Fig. 5.8. The spectra show a dominant minimum corresponding to the 1s excitonic transition. However, no higher excitonic and free carrier transitions are observed.

In order to compare the exciton binding energy in cesium compounds at low and high temperature, we plot the 1s transition energies as a function of magnetic field at low temperature (4 K) and high temperature (180 K) in the same frame, as shown in Fig. 5.9. The data are vertically offset to compensate the change of the band gap induced by the increase of the temperature. The excellent overlap of the

two sets of data indicates that the exciton binding energy does not change within experimental accuracy. The temperature dependent transmission measurement suggests that the $CsPbX_3$ materials do not undergo a structural phase transition up to room temperature. Hence, the dielectric screening does not change, thus, the exciton binding energy does not vary over the investigated temperature interval. This result is in contrast with the organic-inorganic perovskites. The phase transition of organic-inorganic perovskites allows the rotational motion of the organic cations, which enhances the dielectric screening and reduces the exciton binding energy [Poglitsch 1987, Even 2014b, Yang 2017b, Galkowski 2016].

5.6 Conclusion

In this chapter, we present the results of magneto-optical investigation of fully inorganic $CsPbX_3$ compounds (X = I, Br and a mixture of these). The continuous increasing of the bandgap with the temperature indicates the absence of any structural phase transition for fully inorganic perovskite in the temperature range from 4 K to 270 K. Thus, the electronic properties of the $CsPbX_3$ do not change over this temperature range. By performing the magneto-transmission measurement on $CsPbX_3$, we have determined the exciton binding energies and reduced mass with high accuracy. Comparison of the values of dielectric constant for inorganic and hybrid perovskites indicates that, at low temperature when the organic cations are frozen, the dominant contribution to the dielectric screening is related to the relative motion within the lead-halide cage.

Chapter 6

Conclusions

Recently, solar cells based on the hybrid perovskites, with the general chemical formula of ABX_3, have reached an astonishing power conversion efficiency as high as 23.6%. The hybrid perovskites exhibit many advantages for the application of photovoltaic devices, such as strong broad band absorption, low cost fabrication processes, long carrier diffusion lengths and lifetimes. Although remarkable achievement have been made in this research field, there are still many fundamental issues which are under debate. For example, (i) the impact of the microstructure on the Coulomb interaction between the photo-created electron-hole pairs (excitons) in the perovskite materials. (ii) the impact of fully inorganic cation on the electronic properties of mixed compounds. To address these issues, we have used magneto-optical methods to investigate the exciton binding energy and reduced mass in $MAPbI_3$ compound with a variety of crystal grain sizes and in $CsPbX_3$ fully inorganic compounds.

A variety of fabrication methods are employed to prepare the perovskite materials, which leads to a variety of morphologies and different degrees of structural disorder in the perovskite materials. To investigate the correlation between the morphology of the thin film perovskites and the excitonic properties, we have performed magneto-transmission measurement on four different $MAPbI_3$ polycrystalline thin films with different crystal grain sizes (from 50 nm to 770 nm). By analyzing the magnetic field evolution of energies of the interband transitions between the excitonic and free-carrier states, we extract the value of exciton binding energy and reduced mass of $MAPbI_3$. We find that these four $MAPbI_3$ polycrystalline thin films have the same value of exciton binding energy ($R^* = 16 \pm 4\, meV$), and the reduced mass of excitons varies slightly from $0.102\, m_0$ to $0.109\, m_0$. This indicates that the microstructure plays a negligible role in the excitonic properties of the $MAPbI_3$ compounds. To generalize our finding to other perovskite compounds, we have performed the same measurement on triple-cation lead mixed-halide thin film perovskite $Cs_{0.05}(MA_{0.17}FA_{0.83})_{0.95}Pb(I_{0.83}Br_{0.17})_3$ with two considerably different morphologies, namely (i) mesoporous with crystal gain size <50 nm, (ii) planar with crystal grain size around 100-300 nm. The extracted value of reduced mass and binding energy of excitons in these two films are identical ($R^* = 13 \pm 2$ meV, $\mu = 0.096 \pm 0.008\, m_0$). Thus, we conclude that microstructure truly play a negligible role in the exciton properties of mixed organic-inorganic lead halide-based perovskites, regardless of the thin film deposition technique and final morphology.

In addition, we have performed magneto-reflectivity studies on a millimeter size $MAPbI_3$ high quality single crystal. We extract the exciton binding energy and

reduced mass for $MAPbI_3$ for both low temperature ($T = 2\,K$) orthorhombic and high temperature ($T = 168\,K$) tetragonal phases. The exciton binding energy in $MAPbI_3$ single crystal at low temperature is identical to that of $MAPbI_3$ polycrystalline thin films, which confirms that the excitonic properties do not depend upon the crystal size or morphology. The estimated value of exciton binding energy in $MAPbI_3$ single crystal in the tetragonal phase ($R^* = 12\,meV$) is less than the thermal energy (26 meV) at room temperature, indicating a non-excitonic behavior for $MAPbI_3$ single crystal at the operational condition.

Finally, we have investigated the electronic properties of fully inorganic $CsPbX_3$ perovskite, where X = Br, I or an alloy of the two. Before the measurement, the $CsPbX_3$ polycrystalline thin films are annealed to recover the perovskite structure, and then the thin films are put in the liquid helium immediately. This pre-experimental treatment process preserves the perovskite structure of $CsPbX_3$ compounds at temperatures as low as 4 K. After the pre-treatment of the samples, we have measured the absorption of all the $CsPbX_3$ compounds as a function of the temperature. The energy of the 1s transition blue shifts continuously with increasing temperature, suggesting that the $CsPbX_3$ compounds do not undergo a structural phase transition in the temperature range from 4 K to 270 K. We also perform low temperature magneto-transmission spectroscopy on all three $CsPbX_3$ compounds. By analyzing the data, we estimate the exciton binding energy and reduced mass in $CsPbBr_3$, $CsPbI_2Br$ and $CsPbI_3$ compounds. Knowing the value of exciton binding energy and reduced mass, we calculate the dielectric constant for all the measured compounds. By comparing the dielectric constant of the fully inorganic and hybrid perovskites at low temperature, we find that the dielectric constant does not change significantly for a given lead-halide cage, regardless of the cation. Thus, we conclude that at low temperature, when the organic cation motion is frozen, the dielectric mechanism is essentially the same for both hybrid and inorganic perovksites and is mainly dominated by the relative motion of atoms within the lead halide cage.

Appendix A

Publications

Publications based on the results of this thesis:

1. **Z. Yang**, A. Surrente, K. Galkowski, N. Bruyant, D. K. Maude, A. A. Haghighirad, H. J. Snaith, P. Plochocka, and R. J. Nicholas
"Unraveling the Exciton Binding Energy and the Dielectric Constant in Single-Crystal Methylammonium Lead Triiodide Perovskite"
The Journal of Physical Chemistry Letters **8(8)**, 1851-1855 (2017)

2. **Z. Yang**, A. Surrente, K. Galkowski, A. Miyata, O. Portugall, R. J. Sutton, A. A. Haghighirad, H. J. Snaith, D. K. Maude, P. Plochocka, and R. J. Nicholas
"Impact of the Halide Cage on the Electronic Properties of Fully Inorganic Cesium Lead Halide Perovskites"
ACS Energy Letters **2(7)**, 1621-1627 (2017)

3. A. M. Soufiani, **Z. Yang**, T. Young, A. Miyata, A. Surrente, A. Pascoe, K. Galkowski, M. Abdi-Jalebi, R. Brenes, J. Urban, N. Zhang, V. Bulovic, O. Portugall, Y. B. Cheng, R. J. Nicholas, A. Ho-Baillie, M. A. Green, P. Plochocka and S. D. Stranks
"Impact of microstructure on the electron - hole interaction in lead halide perovskites"
Energy and Enviromental Science **10**, 1358-1366 (2017)

Other publications:

1. **Z. Yang**, A. Surrente, G. Tutuncuoglu, K. Galkowski, M. Cazaban-Carrazé, F. Amaduzzi, P. Leroux, D. K. Maude, A. Fontcuberta i Morral, and P. Plochocka
"Revealing Large-Scale Homogeneity and Trace Impurity Sensitivity of GaAs Nanoscale Membranes"
Nano Letters **17(5)**, 2979-2984 (2017)

2. A. Miyata, **Z. Yang**, A. Surrente, O. Drachenko, D. K. Maude, O. Portugall, L. B. Duffy, T. Hesjedal, P. Plochocka, and R. J. Nicholas
"Ultrahigh Magnetic Field Spectroscopy Reveals the Band Structure of the 3D Topological Insulator Bi2Se3"
Physical Review B **96**, 121111 (2017)

3. A. Surrente, D. Dumcenco, **Z. Yang**, A. Kuc, Y. Jing, T. Heine, Y. C. Kung, D. K. Maude, A. Kis, and P. Plochocka

"Defect Healing and Charge Transfer-Mediated Valley Polarization in MoS2/MoSe2/MoS2 Trilayer van der Waals Heterostructures"
Nano Letters **17(7)**, 4130-4136 (2017)

4. K. Galkowski, A. A. Mitioglu, A. Surrente, **Z. Yang**, D. K. Maude, P. Kossacki, G. E. Eperon, J. T.-W. Wang, H. J. Snaith, P. Plochocka and R. J. Nicholas
"Spatially Resolved Studies of the Phases and Morphology of Methylammonium and Formamidinium Lead Tri-halide Perovskites"
Nanoscale **9(9)**, 3222 (2017)

Appendix B

Résumé de la thèse en français

Dans cette annexe, nous présentons un résumé en français de ce travail de thèse. Le lecteur ne trouvera aucune nouvelle information et les figures utilisées sont les mêmes que dans la version anglaise.

B.1 Introduction

Les pérovskites forment une large classe de matériaux, ayant la même structure cristalline que le titanate de calcium ($CaTiO_3$), nommé d'après le minéralogiste russe Lev Perovski (1839) [Wenk 2016]. Les pérovskites sont intéressants pour leur flexibilité de substitution chimique et ont un large éventail d'applications industrielles. Par exemple, $BaTiO_3$ est un matériau très utilisé comme ferroélectriques [Megaw 1945]. $YBa_2Cu_3O_7$ ouvre une nouvelle voie vers la supraconductivité à haute température critique [Wu 1987]. Enfin, $Ba(Zn_{1/3}Ta_{2/3})O_3$ est largement utilisé comme filtres de fréquence dans les communications sans fil [Tamura 1986] grâce à une constante diélectrique élevée.

B.1.1 Structure pérovskite

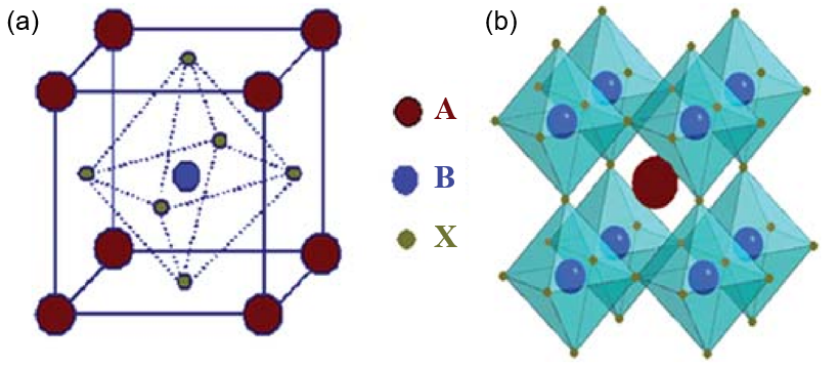

Figure B.1: (a) Structure pérovskite avec la formule chimique ABX_3. (b) Le structure de réseau étendu connecté par octahedre BX_6. Les sphères rouges, bleus, vertes représentent réspectivement les cations A, B et l'anion X. D'après [Cheng 2010].

La formule chimique générale d'une structure pérovskite est ABX_3. La cellule unitaire consiste en un gros cation A, un petit cation B et trois anions X. Un schéma de la cellule unitaire d'une structure pérovskite dans la phase cubique est présenté

dans la figure B.1. Le cation A se trouve aux coins, le cation B est situé au centre du cube, et les anions X sont situés au centre des faces du cube. Dans une structure pérovskite, un cation B et six anions X forment un octaèdre (BX_6 octaèdre), où le cation B est situé au centre de l'octaèdre et les anions X sont situés aux coins autour du cation B (coordination de 6). En réalité, la structure de la pérovskite peut être décrite comme suit : l'octaèdre BX_6 forme un réseau tridimensionnel en reliant tous les coins, tandis que les cations A remplissent les trous parmi les octaèdres (coordination de 12), comme le montre la figure B.1.

B.1.2 Perovskites hybrides

Au cours des dernières années, une grande famille des pérovskites hybrides organiques-inorganiques a attiré beaucoup d'attention en raison de ses nombreuses applications potentielles, comme les diodes électroluminescentes (LED) [Cho 2015], les lasers [Xing 2014] et surtout les dispositifs photovoltaïques à haut rendement [Kojima 2009, Liu 2013]. Les perovskites hybrides organiques-inorganiques sont formés lorsque le cation inorganique A est remplacé par un organique. En raison de l'espace limité entre les octaèdres inorganique, seulement de petits cations organiques, constitués de trois liaisons C-C ou C-N ou moins, peuvent s'adapter à l'intérieur de la structure pérovskite. Les cations A organiques les plus courants sont Méthylammonium (MA: $CH_3NH_3^+$) ou Formamidinium (FA: $CH(NH_2)_2^+$). Les cations B sont habituellement Pb^{2+} ou Sn^{2+}, tandis que les anions X proviennent des halogénures du groupe VII (Br^-, Cl^-, I^-, ou une composition mixte de ceux-ci). Il a été suggéré, que les perovskites hybrides ont un fort caractère d'auto-assemblage pendant la formation du cristal; (i) les ions inorganiques sont favorables à la formation le réseau octaédrique, et (ii) les molécules organiques sont favorables à l'occupation des zones vacantes entre les octaèdres [Cheng 2010]. Ce caractÃÍre fait que ce genre de matériaux est faciles à synthétiser grâce à une variété de méthodes de fabrication, telles que le dépôt séquentiel [Burschka 2013], le traitement en solution [Yang 2015a] assisté par vapeur dépôt [Chen 2013], et aux techniques d'évaporation sous vide [Liu 2013].

Une autre propriété des perovskites hybrides est qu'il est relativement facile de substituer les cations A, B ou les ions halogénures par d'autres éléments. En utilisant la substitution chimique, on peut régler l'énergie de la bande interdite sur une large gamme de 1,1 eV à 3,1 eV [Suarez 2014, Hoke 2015, Zhao 2017], qui couvre l'ensemble du visible et une partie du spectre de la gamme proche infrarouge. En plus des propriétés décrites ci-dessus, les pérovskites hybrides se caractérisent également par une forte absorption à large bande, une longue longueur de diffusion [Dong 2015] et une longue durée de vie des porteurs de charches [Stranks 2013]. Toutes ces propriétés rendent les perovskite hybride très prometteurs en tant que capteur de lumière pour les cellules solaires à faible coût et à haut rendement. $MAPbI_3$, en tant que prototype de cette famille, a d'abord été utilisé comme couche active dans l'industrie solaire dispositifs cellulaires en 2009 [Kojima 2009].

B.1.3 Motivation

Une variétée de méthodes de fabrication sont utilisées pour préparer les matériaux de type pérovskite, tels que les techniques à une seule étape [Kim 2016], à séquençage séquentiel [Burschka 2013] ou à gaz [Huang 2014]. Cela conduit à une variété de morphologies pour les matériaux pérovskite. La morphologie joue un rôle très important, car elle peut influencer la longueur de diffusion ou la durée de vie des porteurs et, par conséquent, l'efficacité des cellules solaires. En plus des paramètres discutés ci-dessus, il a également été suggéré, par Grancini et al. [Grancini 2015], que la morphologie du film a une influence sur l'interaction de Coulomb entre les électron et les trous. En analysant les résultats des spectres de transmission résolus en fonction de la température, ils affirment que l'énergie de liaison de l'exciton peut varier en fonction de la microstructure du film de pérovskite. Afin de vérifier cela, nous avons effectué une spectroscopie de magnéto-transmission sur des films minces $MAPbI_3$ avec une variété de tailles de grains cristallins. Comme nous le verrons, les résultats présentés dans cette thèse démontrent clairement que ce n'est pas le cas.

Il a été démontré récemment que l'introduction de petites quantités de cations inorganiques dans le réseau organique de la perovskite hybride améliore grandement leurs propriétés, résultant en une morphologie supérieure, une efficacité élevée des cellules solaires et une stabilité améliorée dans des conditions de fonctionnement standard [Saliba 2016b, Saliba 2016a, McMeekin 2016]. Malgré les impressionnantes performances des perovskites à cations mixtes, on connaît très peu l'influence du cation de césium inorganique sur les propriétés électroniques des composés mixtes. Afin de répondre à cette question, nous avons étudié les propriétés électroniques de perovskites $CsPbX_3$ entièrement inorganiques.

B.2 Techniques expérimentales

Le deuxième chapitre décrit la mise en place expérimentale, qui est utilisée pour étudier les propriétés excitoniques des pérovskites. Dans cette thèse, deux types de techniques sont utilisés : à savoir les techniques de magnéto-transmission et de magnéto-réflectivité. La technique de magnéto-transmission est utilisée pour mesurer des échantillons transparents (par exemple des films minces polycristallins $MAPbI_3$), tandis que la technique de magnéto-réflectivité est utilisée pour mesurer un échantillon non transparent (par exemple un monocristal de $MAPbI_3$). Plus de détails peuvent être trouvés dans le chapitre 2.

B.3 Magnéto-transmission sur films polycristallins $MAPbI_3$

Nous étudions la corrélation entre la morphologie des pérovskites à couches minces et les propriétés excitoniques. Pour ce faire, nous effectuons des mesures de magnéto-transmission pour extraire l'énergie de liaison et réduire la masse des excitons dans

les films minces $MAPbI_3$, avec une large gamme des tailles de grains de cristal.

B.3.1 Description des échantillions

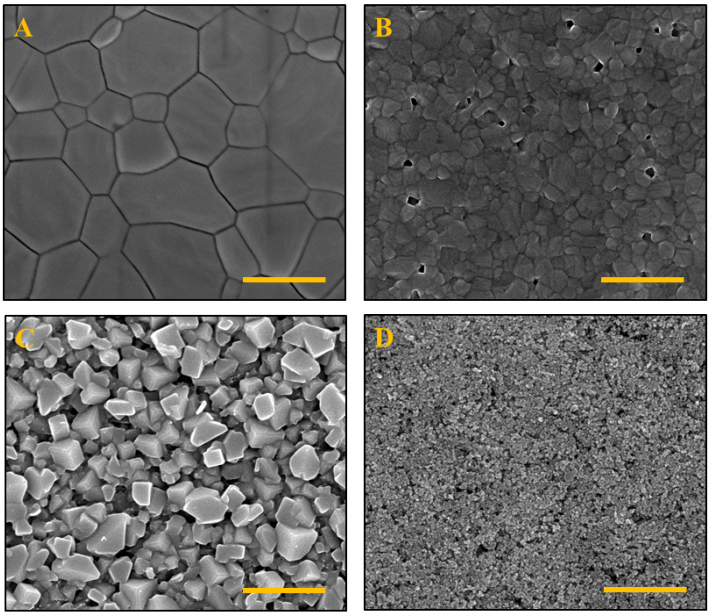

Figure B.2: Images MEB vue de dessus de films minces de $MAPBI_3$ déposés sur des substrats de verre de différentes morphologies. (A) Film mince polycristallin avec une taille moyenne de grain cristallin de 770±230 nm (LPC). (B) film mince polycristallin avec une taille de grain de 210±60 nm (SPC). (C) Petits cristaux de MAPBI fabriqués avec la technique d'immersion en deux étapes traitée par dissolution, donnant une taille de cristaux de 290±70 nm (SC). (D) $MAPBI_3$ infiltré dans un mésoporeux épais-Al_2O_3, résultant d'une taille de grain cristallin < 50 nm (MP). Les barres d'échelle sont 1 μm pour chaque panneau.

La figure B.2 représente des images de microscopie électronique (MEB) de la vue de dessus des échantillons. Les morphologies varient d'un film polycristallin plan avec des tailles de grain de 770±230 nm (A: polycristallin à gros grains annoté LPC) et un film polycristallin avec des tailles de grain de 210±60 nm (B: petit grain polycristallin annoté SPC), à de petits cristaux de 290±70 nm fabriqués par une technique de trempage en deux étapes. (C: petit cristal annoté SC) et également perovskite infiltré dans un échafaudage d'oxyde d'aluminium mésoporeux épaisse de 2 μm (mp-Al_2O_3) avec des tailles de grains <50 nm (D: cristal mésoporeux annoté MP).

B.3.2 Spectres de magnéto-transmission sur un échantillon de LPC

L'approche expérimentale et l'analyse des données utilisées pour tous les échantillons seront expliquées en détail en utilisant comme exemple des résultats de l'échantillon

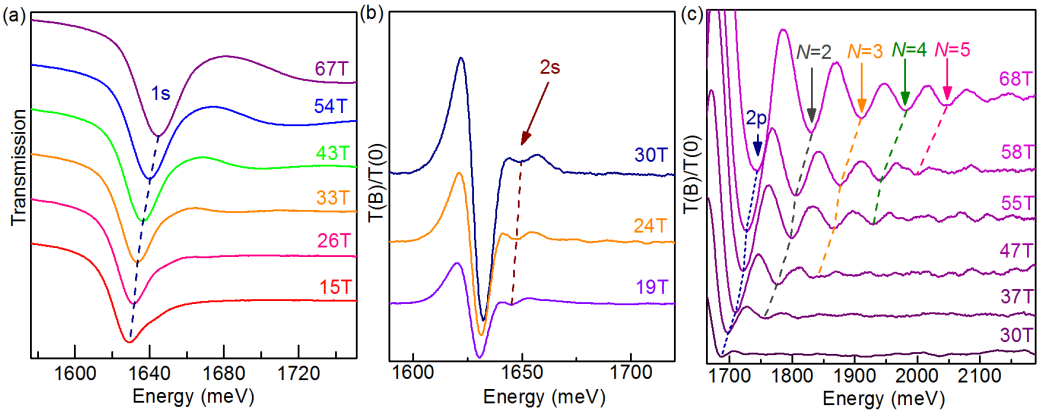

Figure B.3: Spectres typiques de magnéto-transmission d'un échantillon LPC. (a) Séquences de spectres de transmission typiques d'échantillon LPC mesurées sous les champs magnétiques indiqués. (b) Une séquence des rapports des spectres de transmission mesurés sous champ magnétique intermédiaire, qui montre clairement l'état 2s. (c) Une séquence des rapports des spectres de transmission dans la gamme d'énergie supérieure, qui montre clairement les transitions interbandes des niveaux de Landau.

LPC. Les spectres typiques de magnéto-transmission de l'échantillon LPC mesurés aux valeurs indiquées du champ magnétique à basse température (2 K) sont présentés Fig. B.3(a). Pour chaque spectre, nous observons un minimum qui correspond à la transition excitonique 1s. Les états 1s bleu se décale avec un champ magnétique croissant. Pour une identification sans ambiguïté de la transition optique plus faible, nous montrons dans la Fig. B.3(b), (c) le rapport entre les spectres de transmission à un champ magnétique élevé et les spectres de transmission à champ nul. Dans la Fig. B.3 (b), nous présentons les rapport de spectres mesurés sous champ magnétique intermédiaire (19-30 T), qui montre clairement les transitions excitoniques 2s. Une séquence des transitions marquées par des flèches commence à être visible à partir de 30 T dans une plage d'énergie plus élevée, comme présenté dans la Fig. B.3(c). Ces transitions deviennent plus prononcées avec l'augmentation du champ magnétique. Leurs énergies ont un plus grand décalage vers le bleu, induit par le champ magnétique, que les transitions à basse énergie, ce qui suggère qu'il s'agit principalement de transitions de porteurs libres entre les niveaux de Landau dans les bandes de valence et de conduction.

Pour suivre les transitions de porteurs libres sur une plage étendue de champs magnétiques (70 T-150 T), nous avons collaboré avec le Dr. Atsuhiko Miyata pour effectuer une mesure de Mega Gauss au LNCMI-T. Dans cette technique, la transmission de la lumière (laser) monochromatique à travers l'échantillon est mesurée en fonction du champ magnétique. Dans la Fig. B.4, nous montrons les résultats typiques des échantillons de LPC. Tous les spectres montrent des minima clairs en fonction du champ magnétique, qui correspondent à la transition résonante entre les niveaux de Landau des porteurs libres. L'énergie du laser d'excitation est indiquée

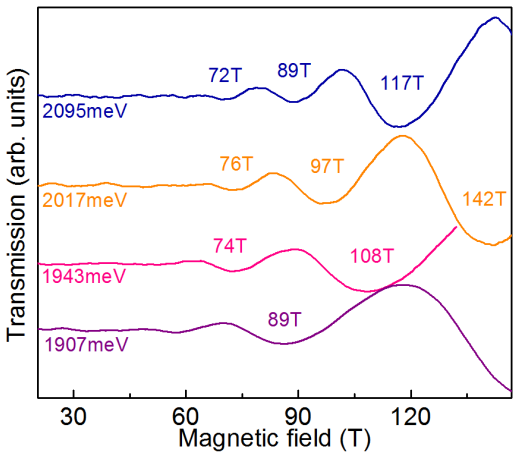

Figure B.4: Résultats typiques de la transmission monochromatique à basse température en fonction du champ magnétique obtenus par la technique de Mega Gauss réalisée par le Dr Atsuhiko Miyata.

en dessous de chaque courbe.

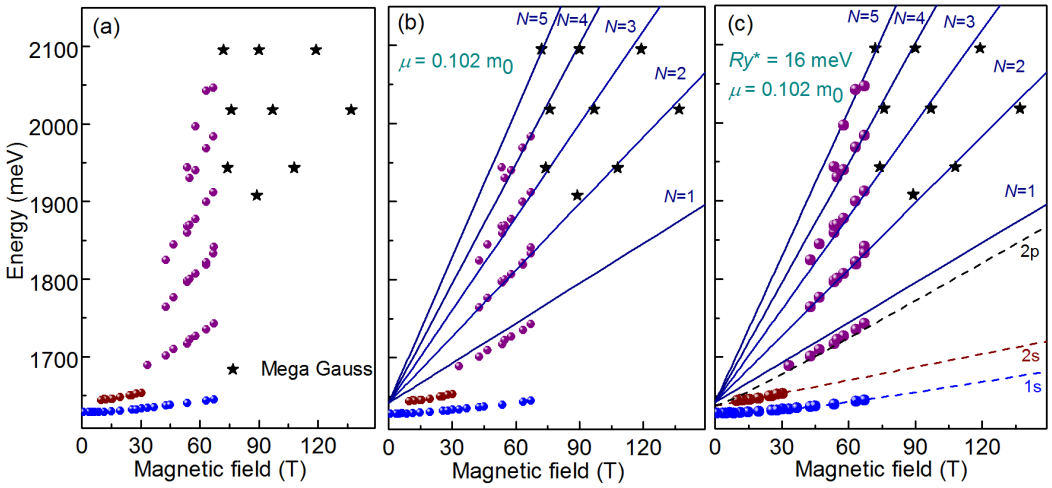

Figure B.5: (a) Résultats typiques des énergies d'absorption en fonction du champ magnétique. Les sphères bleues, rouges et violettes proviennent de la mesure du champ magnétique à impulsions longues, tandis que les étoiles noires proviennent de la mesure de Mega Gauss mesurée par le Dr. Atsuhiko Miyata au LNCMI-T. (b) Ajustement des transitions entre les porteurs libres et les niveaux de Landau de la bande de conduction et de la bande de valence (lignes continues bleues). (c) La courbe du panneau (b) complétée par la courbe d'ajustement du modèle de type hydrogène pour 1s, 2s et 2p (lignes pointillées bleues, rouges et noires).

En supposant que les transitions des porteurs libres dominent dans la gamme des champs magnétiques élevés, nous ajustons d'abord les transitions interbandes entre

les niveaux de Landau dans les bandes de conduction et de valence. La masse réduite μ est le seul paramètre approprié pour tous les niveaux de Landau. La modélisation de la plage de haute énergie et de la plage de champs magnétiques élevée des données permet une détermination précise de la masse réduite. Les résultats d'un ajustement typique de porteurs libres jusqu'à $N = 4$ pour l'échantillon LPC sont montrés sur Fig. B.5(b). Pour cet échantillon, la masse réduite μ est estimée à $0.102 \pm 0.002 m_0$.

Ensuite, dans un second temps, nous utilisons les solutions numériques de Makado et McGill pour que l'hamiltonien ressemblant à l'hydrogène corresponde aux données. Les paramètres d'ajustement de cette solution sont la masse réduite d'exciton μ et l'énergie de liaison d'exciton R^*. Nous utilisons la même masse réduite μ extraite des transitions inter-bandes de Landau. Les résultats d'ajustement sont représentés par des lignes pointillées dans la Fig. B.5(c). Dans cet échantillon, nous avons observé trois transitions excitoniques-1s, 2s et 2p. L'observation des deux états 1 et 2 donne une forte contrainte sur la valeur de l'énergie de liaison d'exciton. L'énergie de liaison de l'exciton dans l'échantillon LPC est estimée à 16 ± 1 meV.

B.3.3 Résultats de la magnéto-transmission sur les échantillons SPC, SC et MP

Table B.1: Résumé des paramètres d'ajustement pour les quatre morphologies de $MAPbI_3$ à basse température (2 K)

	Crystal size (nm)	E_g (meV)	μ (m_0)	Ry* (meV)
LPC	770 ± 230	1642 ± 2	0.102 ± 0.002	16 ± 1
SPC	290 ± 70	1643 ± 2	0.105 ± 0.002	16 ± 4
SC	210 ± 60	1639 ± 2	0.109 ± 0.002	16 ± 4
MP	<50	1638 ± 2	0.107 ± 0.003	16 ± 4

Ensuite, nous avons effectué la même mesure et analyse sur d'autres échantillons $MAPbI_3$ (SPC, SC, MP) avec différentes tailles de grains. Nous avons également adapté les données pour les quatre morphologies de $MAPbI_3$ séparément, comme le montre la Fig. B.6. Les sphères représentent les points de données de la mesure d'impulsion longue. Les étoiles présentent les points de données de la mesure Mega Gauss effectuée par Dr. A. Miyata. Les lignes pleines et pointillées sont respectivement les ajustements de l'ensemble des niveaux de Landau et les transitions excitoniques. Le paramètre d'ajustement pour les quatre échantillons est résumé dans le tableau B.1. Dans la Fig. B.7, nous montre une représentation du tableau B.1. La masse réduite et l'énergie de liaison sont présentées avec respectivement des cercles rouges et des carrés bleus. L'image MEB de chaque échantillon est insérée en bas de la figure. La masse réduite varie de 0,102 m_0 à 0,109 m_0, tandis que l'énergie de liaison reste la même pour tous les échantillons dans l'erreur expérimentale. Ainsi, nous concluons que la microstructure joue un rôle négligeable

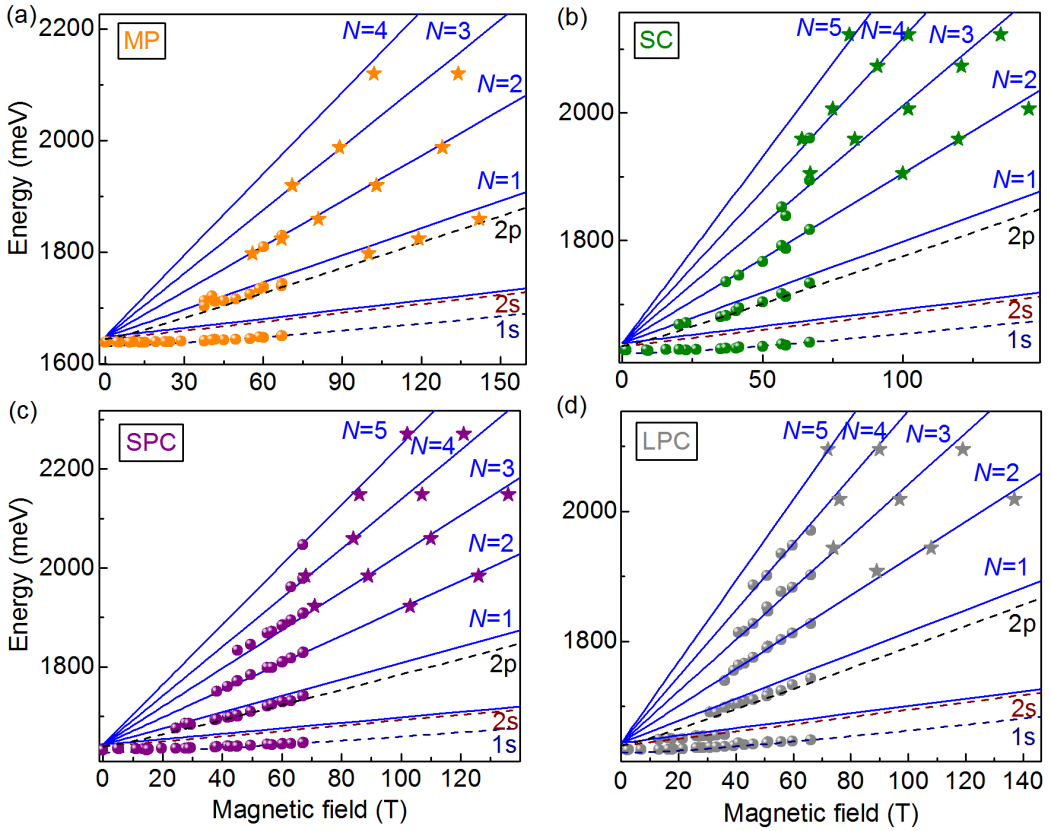

Figure B.6: (a) - (d) Diagrammes en ventilateurs d'énergie séparer des échantillons MP, SC, SPC et MP, respectivement. Les sphères représentent les points de données à partir d'une mesure d'impulsion longue. Les étoiles représentent les points de données issus de la mesure de Mega Gauss effectuée par A. Miyata. Les lignes pleines et pointillées sont respectivement les ajustements à l'ensemble des niveaux de Landau et les transitions excitoniques,.

dans les propriétés d'exciton des perovskites à base d'halogénure de plomb mixte organique-inorganique, quelle que soit la technique de dépôt du film mince et la morphologie finale. Cela confirme l'hypothèse que la large gamme d'énergies de liaison d'excitons trouvées dans la littérature [D'Innocenzo 2014a] ne peut pas être attribuée à des morphologies ou des tailles de grains différentes.

B.4 Magnéto-réflectivité sur monocristal $MAPbI_3$

Dans ce travail, nous avons réalisé des études de magnéto-réflectivité sur une taille millimétrique $MAPbI_3$ monocristal de haute qualité. Premièrement, nous décrivons les données et l'analyse, qui a été effectuée pour obtenir les énergies de la résonance d'absorption des spectres de réflectivité. Nous déduisons ensuite l'énergie de liaison des excitons et la masse réduite à partir des mesures de le réflectivité sous champ

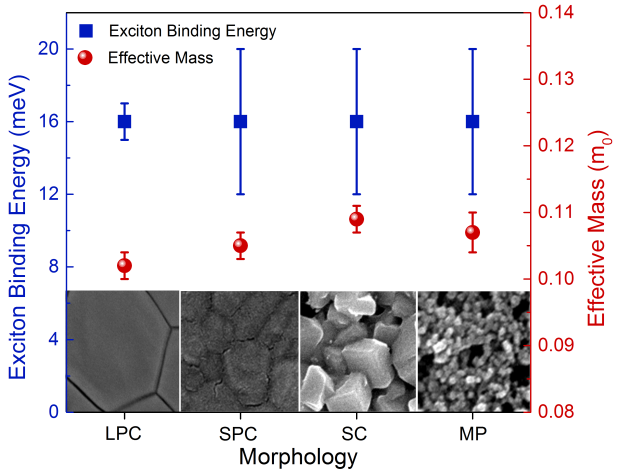

Figure B.7: Énergie de liaison R^* et masse réduite μ des excitons pour les différentes morphologies.

magnétique élevé, à la fois pour les phases orthorhombique à basse température, et les phases tétragonales à haute température.

B.4.1 Magnéto-réflectivité à basse température

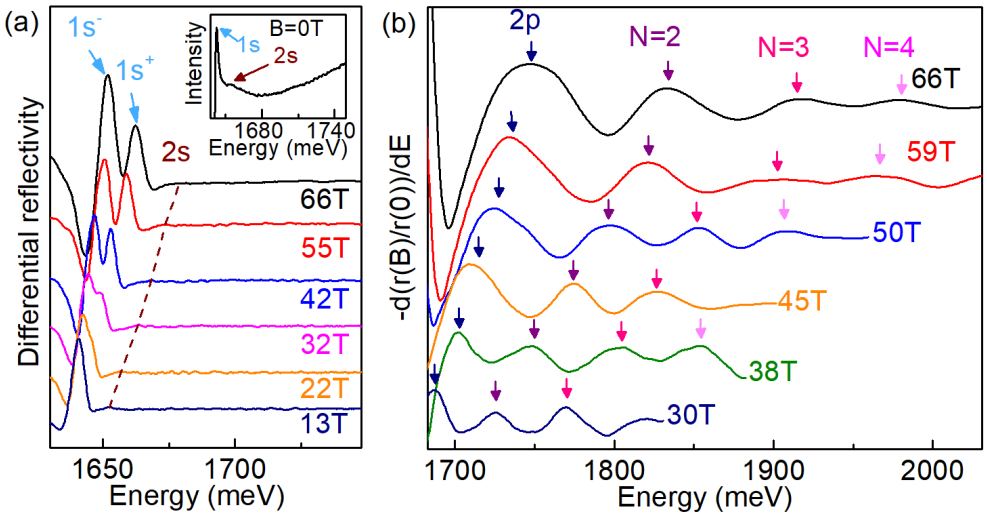

Figure B.8: (a) Spectres de réflectivité différentielle mesurés aux valeurs de champ magnétique indiquées à 2 K. Les flèches indiquent les pics d'absorption. Encart: Spectres de réflectivités tel que mesurés sous un champ magnétique nul. (b) Spectres de réflectivité différentielle sous champ magnétique élevé après normalisation selon la réflectivité à champ nul. Les flèches de mêmes couleurs indiquent la transition entre les mêmes niveaux de Landau.

Un ensemble complet des spectres de magnéto-réflectivité différentielle mesurés á 2 K sont montrés sur la figure B.8(a) pour un champ magnétique montant jusqu'à 66 T. Sous faible champ magnétique, le pic dominant à 1640 meV correspond à la transition excitonique 1s. La division de Zeeman de l'état 1s devient visible autour de 32 T. Du côté de l'énergie supérieure du pic 1s, un pic d'absorption faible supplémentaire est attribué à la transition de l'état excitonique 2s. Pour observer des pics d'absorption supplémentaires dans la gamme d'énergie supérieure, nous avons d'abord divisé les spectres mesurés à un champ magnétique élevé par le spectre à champ nul. De cette manière, nous avons obtenu les rapport de spectres. Ensuite, afin d'obtenir les énergies de transition correctes aux maxima des pics, nous avons calculé la dérivée négative des rapport de spectres, comme présenté sur la figure B.8(b). Une transition excitonique (2p) et trois transitions interbandes entre les niveaux de Landau dans les bandes de conduction et de valence ($N = 2, 3, 4$) sont observées. Notez que la transition excitonique 2p est interdite à un champ magnétique nul, mais devient dipôle autorisé à un champ magnétique élevé une fois que l'énergie du cyclotron dépasse l'énergie de liaison d'exciton [Makado 1986].

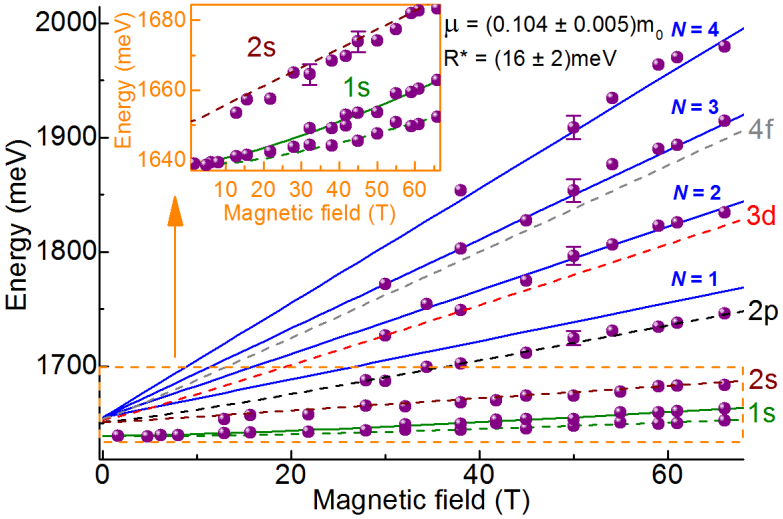

Figure B.9: Energies des transitions excitoniques et des niveaux Landau en fonction du champ magnétique appliqué à 2 K (symboles). Les lignes continues bleues sont le résultat d'un ajustement linéaire des transitions interbandes entre les niveaux de Landau dans les bandes de valence et de conduction. Les lignes pointillées résultent de l'ajustement des transitions de type hydrogène. Encart: Vue agrandie des transitions à basse énergie.

Pour analyser les données, nous tracons l'énergie de l'absorption en fonction du champ magnétique, comme présenté dans la figure B.9. Nous ajustons les données en utilisant les mêmes modèles discutés que le section B.3, à savoir, les lignes pointillées présentent l'ajustement des transitions de type hydrogène dans le champ magnétique basé sur le travail de Makado et McGill [Makado 1986]. Les résultats des ajustements linéaires de la transition interbandes entre les niveaux de Lan-

dau sont présentés sous la forme de lignes continues bleues. Les trois transitions excitoniques et trois transitions de niveau inter-Landau permettent de déterminer précisément l'énergie de liaison de l'exciton et la masse réduite. La division des transitions excitoniques 1s est incluse dans ce modèle en ajoutant le terme Zeeman ($\pm g_{eff}\mu_B B/2$) aux énergies de transition excitoniques, où g_{eff} et μ_B sont le facteur g efficace et Bohr magneton. La division de l'énergie augmente linéairement avec le champ magnétique, ce qui donne un facteur g efficace $g_{eff} = 2.6 \pm 0.1$. Cette valeur est légèrement plus grande que celle trouvée précédemment ($g_{eff} = 1.72 \pm 0.05$) par Tanaka et al. [Tanaka 2003b], probablement en raison de la résolution améliorée de notre mesure. Il est, cependant, assez similaire aux résultats précédents de notre groupe ($g_{eff} = 2.3 \pm 0.1$) obtenu sur $MAPbI_{3-x}Cl_x$ échantillon de film mince [Galkowski 2016].

L'ajustement des transitions des excitons et des porteurs libres permet de conclure qu'à 2 K la masse réduite et l'énergie de liaison des excitons sont $(0.104 \pm 0.005)\, m_0$ et (16 ± 2) meV, respectivement. Il est important de noter que l'énergie de liaison d'exciton obtenue à partir du monocristal est identique à celle des couches minces polycristallines discutées dans le section B.3. Ce résultat confirme la conclusion du section B.3 que les tailles des grains cristallins jouent un rôle négligeable sur l'énergie de liaison des excitons pour les matériaux pérovskites.

B.4.2 Dépendence en temperature de la reflectivité

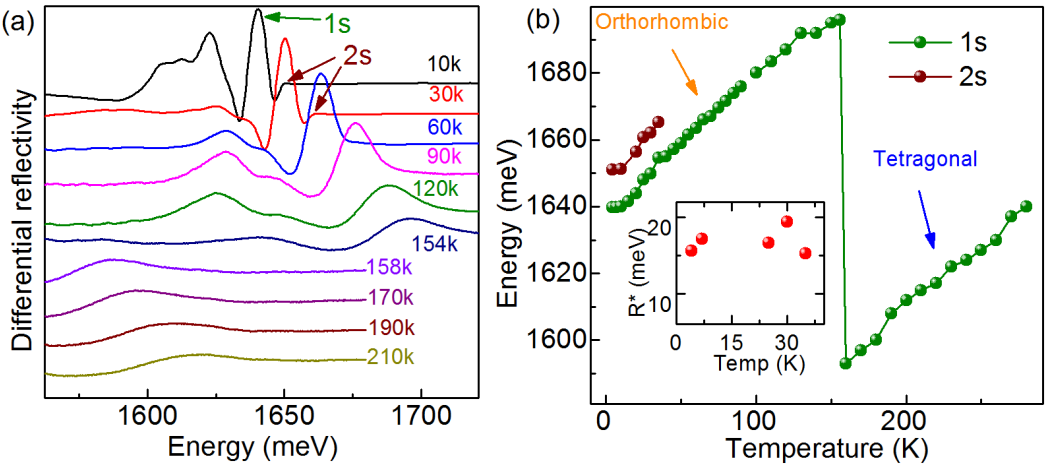

Figure B.10: a) Spectres de réflectivité différentielle mesurés à différentes températures. (b) 1s (cercle vert) et 2s (cercle rouge) énergie de transition en fonction de la température. Encart: énergie de liaison de l'exciton (estimée ici à partir de la division 1s-2s) en fonction de la température.

L'application pratique de dispositifs à base de cellules solaires à base de pérovskite nécessite une connaissance des propriétés électroniques de la phase tétragonale à haute température de ces matériaux. Nous avons d'abord mesuré la dépendance en température des spectres de réflectivité du monocristal. Fig. B.10(a)

montre les spectres de réflectivité différentielle typiques à la température indiquée. La transition 1s apparaît comme un pic prononcé, alors que la transition 2s apparaît comme une petite épaule du côté haute énergie de la transition 1s. En raison de l'excellente qualité cristalline, on observe des transitions 1s et 2s à des températures aussi élevées que 35 K. Les énergies de transition 1s et 2s en fonction de la température sont représentées sur la figure B.10(b). Les transitions 1s et 2s présentent toutes deux une tendance similaire, le décalage vers le bleu avec l'augmentation de la température. Ce décalage vers le bleu est commun dans les matériaux de type perovskite [Wu 2014], contrairement à la majorité des matériaux semi-conducteurs, qui montrent un décalage vers le rouge de l'énergie de bande interdite avec la température croissante [Varshni 1967]. Le décalage bleu observé pour $MAPbI_3$ provient de la séparation accrue entre les extrema de la bande (bande interdite) avec une augmentation de la température [Huang 2013, Singh 2016]. L'énergie de bande interdite de $MAPbI_3$ est significativement réduite par l'interaction spin-orbite. Puisque $MAPbI_3$ a un grand coefficient de dilatation thermique (50 fois plus que le silicium cristallin), lorsque la température augmente, les interactions spin-orbite dans le réseau inorganique sont significativement affaiblies, ce qui entraîne une augmentation de la séparation entre la bande extrema.

Il est possible de déduire l'énergie de liaison R^* des transitions 1s et 2s, puisque la séparation d'énergie de 1s et 2s donne $0.75R^*$. La déduction de R^* en fonction de la température est montrée dans l'encadré de la Fig. B.10(b). La déduction de R^* ne montre aucune dépendance en température jusqu'à 35 K. Ceci est attendu, car il n'y a pas de transition de phase structurelle pour $MAPbI_3$ dans la gamme de température de 4 K à 35 K, de sorte que l'énergie de liaison d'exciton devrait rester la même.

La transition de phase dans le film mince $MAPbI_3$ de la phase orthorhombique à la phase tétragonale se produit environ 150 K [Baikie 2013] et est accompagnée d'un dramatique décalage vers le rouge de l'énergie de gap. ($\sim$100 meV) [D'Innocenzo 2014a, Even 2014b, Yamada 2015]. Dans notre cas, vers 154 K, il y a une transition brusque vers une énergie plus faible, décalée de 103 meV. Ceci suggère que l'échantillon a achevé la transition de la phase orthorhombique basse température à la phase quadratique haute température.

B.4.3 Magnéto-réflectivité à haute température

Pour étudier les propriétés électroniques des monocristaux de $MAPbI_3$ dans la phase tétragonale, nous répétons la mesure de magnéto-réflectivité à 168 K. Les spectres de réflectivité différentielle mesurés jusqu'à 66 T sont montrés sur la figure B.11(a). Les états excitoniques 1s apparaissent comme un pic prononcé dans le spectre de réflectivité avec un élargissement considérable (FWHM de 22 meV). Les états 2s apparaissent comme un pic peu profond sous champs magnétiques supérieurs à 39 T. Cependant, à une température aussi élevée, aucune transition excitonique supérieure ou niveau de Landau n'est observée. Fig. B.11(b) représente le diagramme d'énergie à 168 K. Nous avons ajusté les données pour la transition 1s et

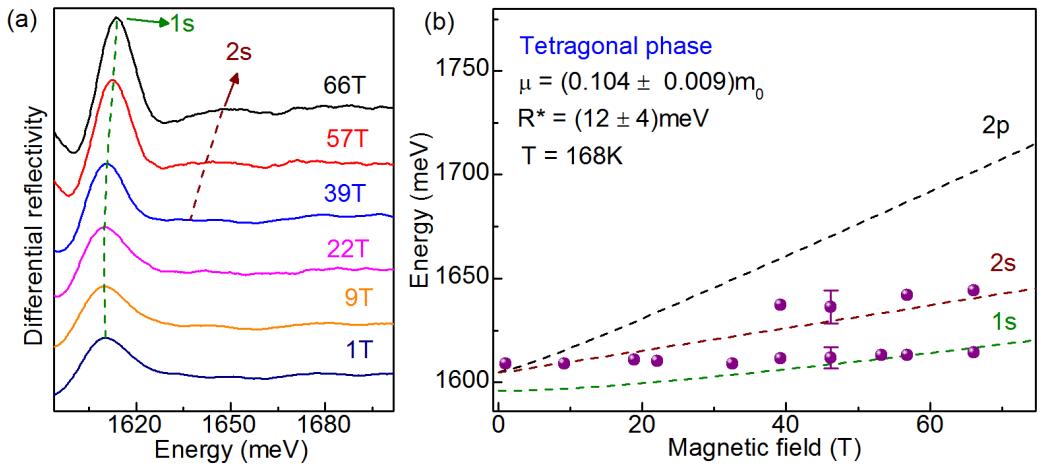

Figure B.11: (a) Dérivée par rapport à l'énergie des spectres de magnéto-réflectivité mesurés à T = 168 K. (b) Diagramme d'énergieà haute température. Les lignes pointillées indiquent des transitions hydrogéniques.

2s. De notre travail précédent [Miyata 2015], les masses réduites de films minces perovskite restent presque les mêmes pour la phase orthorhombique et la phase tétragonale. Ainsi, nous supposons que la masse réduite de monocristal à la phase tétragonale est la même qu'à basse température, $\mu \simeq 0.104\, m_0$. Avec la même procédure d'ajustement décrite pour Fig. B.9, nous trouvons une énergie de liaison exciton de 12±4 meV comparable à celle estimée par des expériences similaires de magnéto-transmission à haute température sur un film mince [Miyata 2015]. La valeur de l'énergie de liaison de l'exciton diminue de quelques meV lorsque l'on passe de la phase orthorhombique à la phase tétragonale. Ceci est cohérent avec le fait que la transition de phase augmente le désordre dynamique lié au mouvement de rotation du cation organique, entraînant une augmentation de la constante diélectrique [Poglitsch 1987, Even 2014b].

Bien que le $MAPbI_3$ reste dans la phase tétragonale, la réponse diélectrique ne change pas, donc nous supposons que l'énergie de liaison de l'exciton reste inchangée en phase tétragonale indépendante de la température. L'énergie thermique à la température de la pièce est de l'ordre de 26%, ce qui est supérieur à l'énergie de liaison de l'exciton dans le monocristal. Dans ce cas, les électrons et les trous dans les excitons sont dissociés par l'énergie thermique à température ambiante, ce qui suggère que les porteurs libres (plutôt que les excitons) sont dominants dans le monocristal à température ambiante.

B.5 Mesure de magneto-transmission de $CsPbX_3$

Dans ce travail, nous présentons les résultats d'études optiques des propriétés électroniques de couches minces de $CsPbX_3$ entièrement inorganiques, de X = Br, ou d'un alliage des deux. La dépendance à la température des mesures d'absorption

suggère que $CsPbX_3$ ne subit pas de transition de phase structurelle dans la gamme de 4 K à 270 K, ce qui contraste fortement avec les pérovskites organiques-inorganiques. Nous avons également effectué une magnéto-transmission mesures pour déterminer l'énergie de liaison et la masse réduite de l'exciton dans $CsPbX_3$. En comparant la constante diélectrique des pérovskites hybrides et entièrement inorganiques, nous montrons que, à basse température, le criblage diélectrique est essentiellement le même pour les matériaux hybrides et inorganiques et est principalement dominé par le mouvement relatif des atomes dans la cage aux halogénures de plomb .

B.5.1 Échantillons traitement pré-expérimental

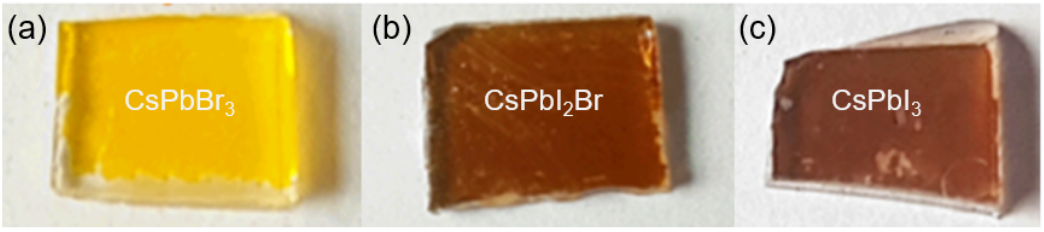

Figure B.12: (a) - (c) Photos des échantillons recuits $CsPbBr_3$, $CsPbI_2Br$ et $CsPbI_3$, respectivement.

En raison de leur stabilité limitée dans l'air à température ambiante [Eperon 2014], les échantillons $CsPbX_3$ ont été systématiquement recuits avant les expériences. Le but de cette procédure de recuit est de récupérer la phase cubique pérovskite pour tous les composés, car les composés $CsPbX_3$ à phase cubique présentent un intérêt potentiel dans les dispositifs photovoltaïques. Initialement, $CsPbI_3$ et $CsPbI_2Br$ sont transparents, en raison du fait qu'ils sont dans une phase non-pérovskite et ont une bande interdite proche de la gamme UV. $CsPbBr_3$ a une couleur jaune, en raison du fait qu'il est dans une phase orthorhombique avec une bande interdite dans 2,3-2,4 eV. Les températures de la transition de phase pour ces trois composés sont différentes (comme discuté ci-dessus), ainsi, ils sont recuits à différentes températures. CsPbI3 a été recuit à 623 K pendant 10 min. $CsPbI_2Br$ et $CsPbBr_3$ ont été recuits à 523 K pendant 5-7 min. La figure B.12(a-c) présente les photos de $CsPbBr_3$, $CsPbI_2Br$ et $CsPbI_3$ après la procédure de recuit. Après recuit, $CsPbBr_3$ montre une couleur jaune suggérant une bande interdite dans la gamme de 2,3-2,4 eV, cependant la structure cristalline de $CsPbBr_3$ recuit est difficile à déterminer à partir de la couleur. $CsPbI_2Br$ et $CsPbI_3$ présentent une couleur brune suggérant une bande interdite comprise entre 1,7 et 1,9 eV. Après recuit, les échantillons ont été immergés dans de l'hélium liquide dans un cryostat en 4 minutes.

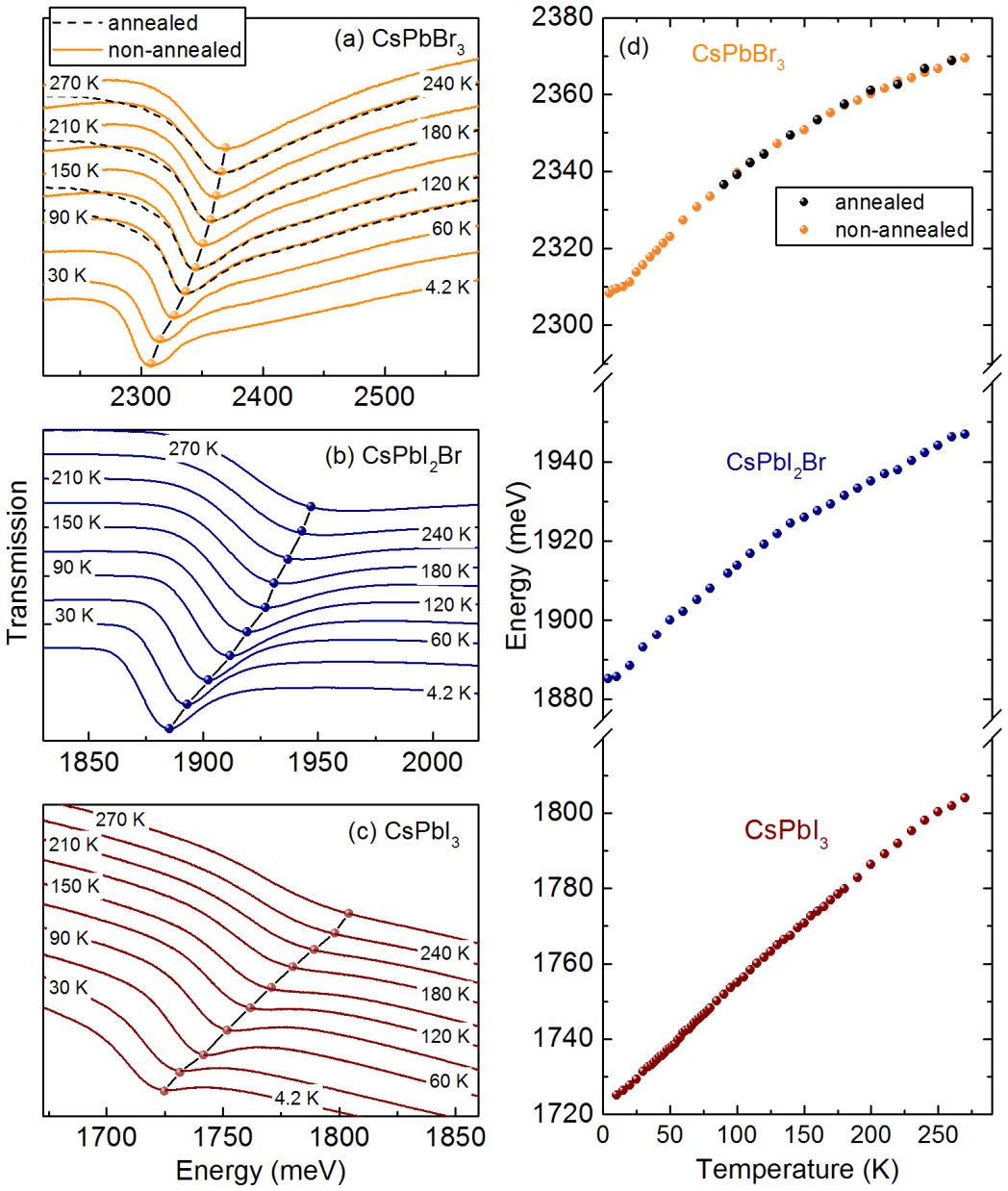

Figure B.13: Spectres de transmission typique de (a) l'échantillon $CsPbBr_3$, (b) $CsPbI_2Br$ et (c) $CsPbI_3$ mesurés à différentes températures. Les symboles de cercle représentent l'évolution de l'absorption de 1s avec la température. (d) Energie des transitions 1s en fonction de la température pour les trois composés. Les lignes pointillées noires et les lignes pleines orange dans le panneau (a) représentent les spectres de $CsPbBr_3$ recuits et préparés. Les cercles noirs et orange du panneau (d) représentent les énergies des transitions 1s pour $CsPbBr_3$ recuit et préparés.

B.5.2 Mesure de transmission en fonction de la température

Dans la Fig. B.13, nous montrons les spectres de transmission typiques de $CsPbBr_3$, $CsPbI_2Br$, $CsPbI_3$ mesurés sur une large gamme de températures variant de 4 K à 270 K. Chaque spectre de transmission montre un minimum unique clair, qui correspond à la 1s excitonique absorption. Le bleu minimum se déplace et s'élargit avec l'augmentation de la température pour tous les composés. Nous traçons l'énergie du minimum des résonances d'absorption en fonction de la température de la figure B.13(d). Les énergies d'absorption changent continuellement avec l'augmentation de la température. Dans les matériaux perovskites organiques-inorganiques, la transition de phase structurale s'accompagne toujours d'un changement dramatique d'énergie de bande interdite [Stoumpos 2013a, Baikie 2013, Galkowski 2017]. Ainsi, le décalage continu de la bande interdite en fonction de la température suggère qu'il n'y a pas de transition de phase structurelle dans $CsPbX_3$. Ce phénomène est en contraste frappant avec les perovskites hybrides organiques-inorganiques. Dans la plage de température de 4 K-300 K, les pérovskites hybrides organiques-inorganiques présentent une transition de phase structurale autour de 150 K-170 K de la phase orthorhombique basse température à la phase tétragonale haute température [Stoumpos 2013a, Baikie 2013].

B.5.3 Mesure de magnéto-transmission à basse température

Nous avons effectué une spectroscopie de magnéto-transmission à basse température pour étudier les propriétés électroniques des composés $CsPbX_3$, en utilisant des techniques de champs magnétiques pulsés longs. Les résultats sont présentés et discuté ci-dessous.

B.5.3.1 Résultats typiques et analyse des données

Nous analysons les données de magnéto-transmission pour tous les composés Cs de la même manière que pour $MAPbI_3$. A savoir, nous prenons l'énergie au minimum de la ligne d'absorption et construisons le diagramme d'énegie pour $CsPbI_3$, $CsPbI_2Br$ et $CsPbBr_3$. Les résultats typiques sont montrés sur la Fig. B.14. Les cercles bleus représentent les données de mesures d'impulsions longues, tandis que les étoiles noires représentent les données issues des mesures de Mega Gauss effectuées par A. Miyata. Nous ajustons les données de transition excitoniques dans la plage de basse énergie avec le modèle de l'hydrogène. Pour les données de gamme d'énergie plus élevée, nous avons utilisé la formule correspondant à la transition inter-bande entre le niveau de Landau dans la bande de conduction et de valence. Les lignes orange présentent l'ajustement pour les transitions excitoniques. Les lignes grises présentent l'ajustement pour transition interbandes entre les niveaux de Landau. Nous mettons en évidence l'ajustement des transitions excitoniques 1s-2s en traçant une vue élargie de la partie bas champ et basse énergie du diagramme dans les panneaux en dessous du diagrame d'énergie complèt. Les valeurs de la masse effective

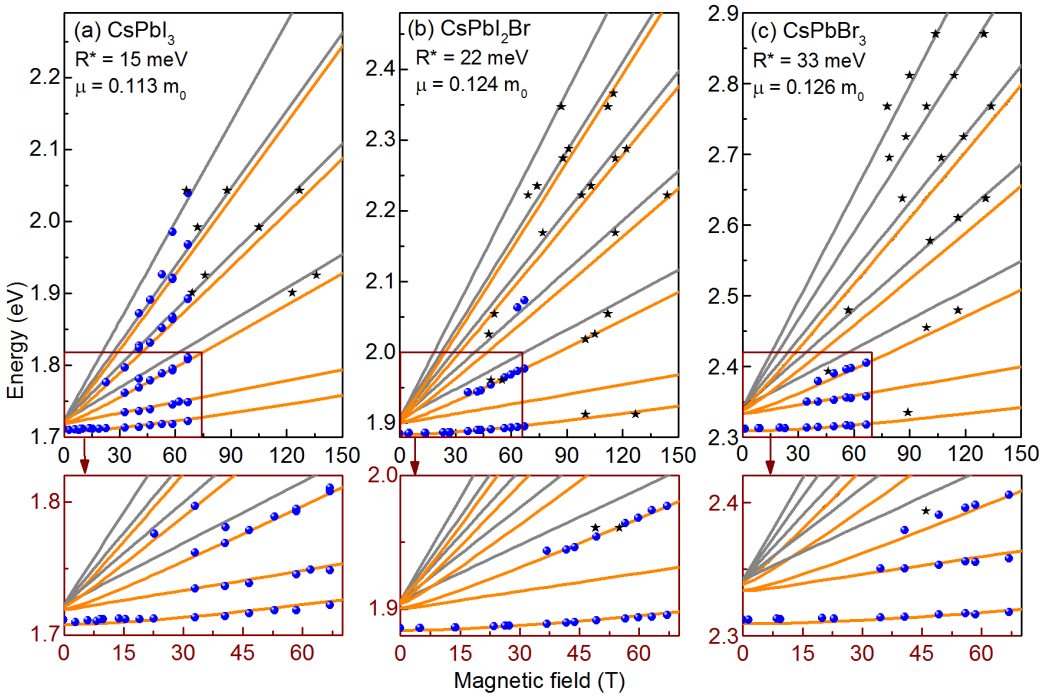

Figure B.14: Les énergies de transition des excitons et des porteurs libres en fonction du champ magnétique à 2 K pour (a) $CsPbI_3$, (b) $CsPbI_2Br$ et (a) $CsPbBr_3$. Les cercles représentent les données issues de la mesure du champ de l'impulsion longue. Les étoiles sont les données de la mesure Mega Gauss effectuée par A. Miyata. Les lignes orange et grises sont le résultat de l'ajustement de la transition de type hydrogène et de la transition inter-bande entre les niveaux de Landau. Les panneaux inférieurs montrent le zoom avant de la partie basse et basse énergie du diagramme d'éénergie.

μ et de l'énergie de liaison Ry^* obtenues par la procédure d'ajustement pour les trois composés sont indiquées sur chaque figure et résumées dans le tableau B.3.

Dans la figure B.15, nous montrons l'énergie de liaison et la masse réduite de l'exciton dans les composés de césium et les composés organiques-inorganiques en fonction de la bande interdite. Les étoiles brunes, rouges et jaunes présentent les résultats pour $CsPbI_3$, $CsPbI_2Br$ et $CsPbBr_3$. à titre de comparaison, nous avons ajouté les résultats des perovskites hybrides organiques-inorganiques provenant des travaux antérieurs de notre groupe marqués comme des cercles [Miyata 2015, Galkowski 2016]. Les cercles roses et violets représentent les résultats pour les pérovskites hybrides à base de FA et MA. L'évolution de l'énergie de liaison d'excitons avec la bande interdite est ajustée avec l'équation $R^* = 0,010E_g$, comme indiqué en trait noir sur la figure B.15. Dans la Fig B.15(b), nous observons une augmentation de la masse effective avec l'augmentation de la bande interdite. Cela peut être compris dans le cadre d'un modèle k.p simple à deux bandes [Heo 2013]. En supposant que la masse efficace pour la valence et la bande de

Table B.2: Paramètres déterminés à partir de l'ajustement du diagramme du ventilateur énergétique pour CsPbX $_3$ à 2 K.

Compound	Phase	E_g (meV)	R^* (meV)	μ (m_0)
$CsPbI_3$	cubic	1723	15 ± 1	0.114 ± 0.01
$CsPbI_2Br$	cubic	1906	22 ± 3	0.124 ± 0.02
$CsPbBr_3$	orthorhombic	2342	33 ± 1	0.126 ± 0.01

conduction sont les mêmes, la masse réduite de l'exciton peut s'écrire comme,

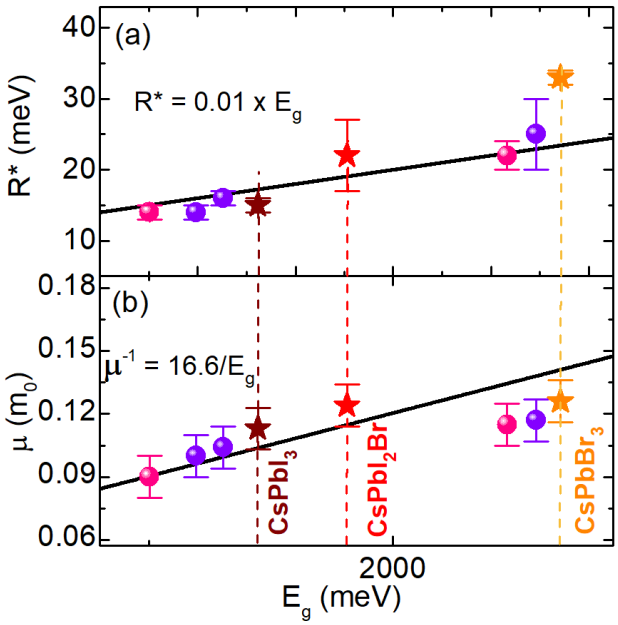

Figure B.15: (a) L'énergie de liaison et (b) la masse effective en fonction de la bande interdite. Les étoiles brunes, rouges et jaunes représentent les résultats pour CsPbI $_3$, CsPbI $_2$ Br et CsPbBr $_3$. Les cercles roses et violets représentent les résultats pour les pérovskites hybrides à base de FA et MA, provenant de notre travail précédent [Miyata 2015, Galkowski 2016].

$$\frac{1}{\mu} = \frac{4|P|^2}{m_0 E_g}, \tag{B.1}$$

où $P = \langle \Psi_{\mathrm{VB}} | p_x | \Psi_{\mathrm{CB}} \rangle$ est l'élément de matrice de quantité de mouvement qui couple les états des bandes de conduction et de valence. $2|p|^2/m_0$ est l'énergie de Kane [Makado 1986]. Les prédictions théoriques de l'énergie de Kane sont de l'ordre de 5.3-6.3 eV pour ces matériaux [Even 2014b, Fang 2015]. L'évolution de la masse réduite avec la bande interdite reproduit une énergie de Kane de 8,3 eV, seulement

légèrement supérieure aux prédictions théoriques. L'écart peut provenir de la valeur différente de la masse effective utilisée dans le modèle.

Avec la valeur de la masse effective et de l'énergie de liaison de l'exciton, la constante diélectrique effective des matériaux peut être calculée en utilisant,

$$\epsilon_{eff} = \frac{e^2}{\hbar}\sqrt{\frac{\mu}{2R_y^*}}, \tag{B.2}$$

En utilisant les valeurs de la masse effective des excitons et de l'énergie de liaison obtenues à partir du raccord, nous avons calculé les constantes diélectriques efficaces ϵ_{eff} pour tous les composés, résumées dans le tableau B.3.

Table B.3: Constante diélectrique effective calculée pour $CsPbX_3$ à 2 K.

Compound	Phase	E_g (meV)	ε_{eff}
$CsPbI_3$	cubic	1723	10.0 ± 0.4
$CsPbI_2Br$	cubic	1906	8.6 ± 0.8
$CsPbBr_3$	orthorhombic	2342	7.3 ± 0.4

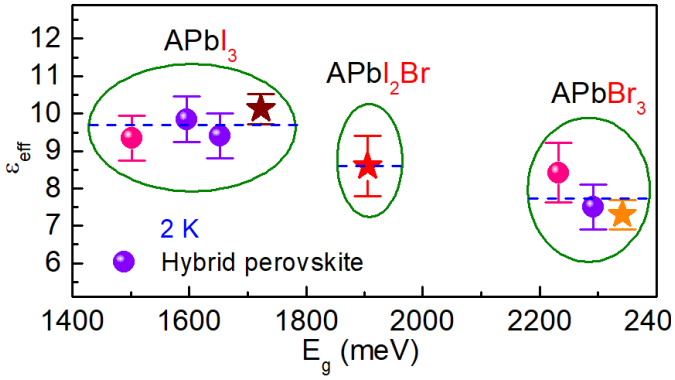

Figure B.16: Constante diélectrique en fonction de la bande interdite. Les étoiles brunes, rouges et jaunes représentent les résultats pour $CsPbI_3$, $CsPbI_2Br$ et $CsPbBr_3$. Les cercles roses représentent les résultats pour les pérovskites hybrides à base de FA, tandis que les cercles violets représentent les résultats pour les pérovskites hybrides à base de MA.

Dans la Fig. B.16, nous avons comparé la constante diélectrique effective pour les pérovskites à base de césium (étoiles) avec les pérovskites hybrides organiques-inorganiques (cercles) mesurées à 2 K. Pour comprendre les résultats, nous regroupons d'abord les données de la même manière que les points de données d'un même groupe ont le même halogénure et différents cation A (MA, FA, Cs). Les lignes pointillées bleues indiquent la valeur moyenne de la constante diélectrique dans chaque groupe. Il ressort des résultats que la constante diélectrique ne change

pas plus que l'erreur expérimentale pour une cage donnée en halogénure de plomb, quel que soit le cation. Il a été suggéré que les contributions principales au criblage diélectrique sont dues aux modes d'étirement Pb-X et aux modes de basculement Pb-X-Pb [Pérez-Osorio 2015, Sendner 2016]. Ceci est cohérent avec ce qui est observé sur la Fig. B.16. A basse température, lorsque le mouvement des cations organiques est gelé, le mécanisme diélectrique est essentiellement le même pour les perovksites hybrides et inorganiques et est principalement dominé par le mouvement relatif des atomes dans la cage aux halogénures de plomb.

Bibliography

[Ahmad 2017] Waqar Ahmad, Jahangeer Khan, Guangda Niu and Jiang Tang. *Inorganic $CsPbI_3$ Perovskite-Based Solar Cells: A Choice for a Tandem Device*. Solar RRL, 2017. (Cited on page 18.)

[Amat 2014] Anna Amat, Edoardo Mosconi, Enrico Ronca, Claudio Quarti, Paolo Umari, Md K Nazeeruddin, Michael Gratzel and Filippo De Angelis. *Cation-induced band-gap tuning in organohalide perovskites: interplay of spin–orbit coupling and octahedra tilting*. Nano letters, vol. 14, no. 6, pages 3608–3616, 2014. (Cited on pages 4, 6 and 7.)

[Baena 2015] Juan Pablo Correa Baena, Ludmilla Steier, Wolfgang Tress, Michael Saliba, Stefanie Neutzner, Taisuke Matsui, Fabrizio Giordano, T Jesper Jacobsson, Ajay Ram Srimath Kandada, Shaik M Zakeeruddin*et al.* *Highly efficient planar perovskite solar cells through band alignment engineering*. Energy & Environmental Science, vol. 8, no. 10, pages 2928–2934, 2015. (Cited on page 20.)

[Baikie 2013] Tom Baikie, Yanan Fang, Jeannette M Kadro, Martin Schreyer, Fengxia Wei, Subodh G Mhaisalkar, Michael Graetzel and Tim J White. *Synthesis and crystal chemistry of the hybrid perovskite $(CH_3NH_3)PbI_3$ for solid-state sensitised solar cell applications*. Journal of Materials Chemistry A, vol. 1, no. 18, pages 5628–5641, 2013. (Cited on pages 63, 70, 94 and 98.)

[Bailie 2015] Colin D Bailie, M Greyson Christoforo, Jonathan P Mailoa, Andrea R Bowring, Eva L Unger, William H Nguyen, Julian Burschka, Norman Pellet, Jungwoo Z Lee, Michael Grätzel*et al.* *Semi-transparent perovskite solar cells for tandems with silicon and CIGS*. Energy & Environmental Science, vol. 8, no. 3, pages 956–963, 2015. (Cited on page 20.)

[Beal 2016] Rachel E Beal, Daniel J Slotcavage, Tomas Leijtens, Andrea R Bowring, Rebecca A Belisle, William H Nguyen, George F Burkhard, Eric T Hoke and Michael D McGehee. *Cesium lead halide perovskites with improved stability for tandem solar cells*. The journal of physical chemistry letters, vol. 7, no. 5, pages 746–751, 2016. (Cited on pages 16, 21, 69 and 70.)

[Béard 2013] J Béard, J Billette, P Frings, M Suleiman and F Lecouturier. *Special coils development at the national high magnetic field laboratory in Toulouse*. Journal of Low Temperature Physics, vol. 170, no. 5-6, pages 442–446, 2013. (Cited on page 32.)

[Borriello 2008] Ivo Borriello, Giovanni Cantele and Domenico Ninno. *Ab initio investigation of hybrid organic-inorganic perovskites based on tin halides*. Physical Review B, vol. 77, no. 23, page 235214, 2008. (Cited on pages 4 and 6.)

[Brgoch 2014] Jakoah Brgoch, Anna J Lehner, Michael Chabinyc and Ram Seshadri. *Ab initio calculations of band gaps and absolute band positions of polymorphs of $RbPbI_3$ and $CsPbI_3$: Implications for main-group halide perovskite photovoltaics.* The Journal of Physical Chemistry C, vol. 118, no. 48, pages 27721–27727, 2014. (Cited on pages 16 and 17.)

[Brivio 2014] Federico Brivio, Keith T Butler, Aron Walsh and Mark Van Schilfgaarde. *Relativistic quasiparticle self-consistent electronic structure of hybrid halide perovskite photovoltaic absorbers.* Physical Review B, vol. 89, no. 15, page 155204, 2014. (Cited on pages 14 and 61.)

[Brivio 2015] Federico Brivio, Jarvist M Frost, Jonathan M Skelton, Adam J Jackson, Oliver J Weber, Mark T Weller, Alejandro R Goni, Aurélien MA Leguy, Piers RF Barnes and Aron Walsh. *Lattice dynamics and vibrational spectra of the orthorhombic, tetragonal, and cubic phases of methylammonium lead iodide.* Physical Review B, vol. 92, no. 14, page 144308, 2015. (Cited on pages 7 and 8.)

[Burschka 2013] Julian Burschka, Norman Pellet, Soo-Jin Moon, Robin Humphry-Baker, Peng Gao, Mohammad K Nazeeruddin and Michael Grätzel. *Sequential deposition as a route to high-performance perovskite-sensitized solar cells.* Nature, vol. 499, no. 7458, pages 316–319, 2013. (Cited on pages 3, 9, 84 and 85.)

[Bush 2017] Kevin A Bush, Axel F Palmstrom, J Yu Zhengshan, Mathieu Boccard, Rongrong Cheacharoen, Jonathan P Mailoa, David P McMeekin, Robert LZ Hoye, Colin D Bailie, Tomas Leijtens*et al. 23.6%-efficient monolithic perovskite/silicon tandem solar cells with improved stability.* Nature Energy, vol. 2, page 17009, 2017. (Cited on page 21.)

[Buttner 1992] RH Buttner and EN Maslen. *Structural parameters and electron difference density in $BaTiO_3$.* Acta Crystallographica Section B: Structural Science, vol. 48, no. 6, pages 764–769, 1992. (Cited on page 3.)

[Cardona 2005] Manuel Cardona and Y Yu Peter. Fundamentals of semiconductors. Springer, 2005. (Cited on page 57.)

[Chen 2013] Qi Chen, Huanping Zhou, Ziruo Hong, Song Luo, Hsin-Sheng Duan, Hsin-Hua Wang, Yongsheng Liu, Gang Li and Yang Yang. *Planar heterojunction perovskite solar cells via vapor-assisted solution process.* Journal of the American Chemical Society, vol. 136, no. 2, pages 622–625, 2013. (Cited on pages 3 and 84.)

[Chen 2017] Chien-Yu Chen, Hung-Yu Lin, Kai-Ming Chiang, Wei-Lun Tsai, Yu-Ching Huang, Cheng-Si Tsao and Hao-Wu Lin. *All-Vacuum-Deposited Stoichiometrically Balanced Inorganic Cesium Lead Halide Perovskite Solar*

Cells with Stabilized Efficiency Exceeding 11%. Advanced Materials, vol. 29, no. 12, 2017. (Cited on page 18.)

[Cheng 2010] Ziyong Cheng and Jun Lin. *Layered organic–inorganic hybrid perovskites: structure, optical properties, film preparation, patterning and templating engineering*. CrystEngComm, vol. 12, no. 10, pages 2646–2662, 2010. (Cited on pages 2, 3, 83 and 84.)

[Cho 2015] Himchan Cho, Su-Hun Jeong, Min-Ho Park, Young-Hoon Kim, Christoph Wolf, Chang-Lyoul Lee, Jin Hyuck Heo, Aditya Sadhanala, NoSoung Myoung, Seunghyup Yoo*et al. Overcoming the electroluminescence efficiency limitations of perovskite light-emitting diodes*. Science, vol. 350, no. 6265, pages 1222–1225, 2015. (Cited on pages 3 and 84.)

[Correa-Baena 2017] Juan-Pablo Correa-Baena, Michael Saliba, Tonio Buonassisi, Michael Grätzel, Antonio Abate, Wolfgang Tress and Anders Hagfeldt. *Promises and challenges of perovskite solar cells*. Science, vol. 358, no. 6364, pages 739–744, 2017. (Cited on pages 18 and 19.)

[Diab 2016] Hiba Diab, Gaëlle Trippé-Allard, Ferdinand Lédée, Khaoula Jemli, Christèle Vilar, Guillaume Bouchez, Vincent LR Jacques, Antonio Tejeda, Jacky Even, Jean-Sébastien Lauret*et al. Narrow Linewidth Excitonic Emission in Organic–Inorganic Lead Iodide Perovskite Single Crystals*. The journal of physical chemistry letters, vol. 7, no. 24, pages 5093–5100, 2016. (Cited on page 57.)

[Dil 2009] J Hugo Dil. *Spin and angle resolved photoemission on non-magnetic low-dimensional systems*. Journal of Physics: Condensed Matter, vol. 21, no. 40, page 403001, 2009. (Cited on page 15.)

[D'Innocenzo 2014a] Valerio D'Innocenzo, Giulia Grancini, Marcelo JP Alcocer, Ajay Ram Srimath Kandada, Samuel D Stranks, Michael M Lee, Guglielmo Lanzani, Henry J Snaith and Annamaria Petrozza. *Excitons versus free charges in organo-lead tri-halide perovskites*. Nature communications, vol. 5, page 3586, 2014. (Cited on pages 49, 53, 63, 90 and 94.)

[D'Innocenzo 2014b] Valerio D'Innocenzo, Ajay Ram Srimath Kandada, Michele De Bastiani, Marina Gandini and Annamaria Petrozza. *Tuning the light emission properties by band gap engineering in hybrid lead halide perovskite*. Journal of the American Chemical Society, vol. 136, no. 51, pages 17730–17733, 2014. (Cited on page 41.)

[Dong 2015] Qingfeng Dong, Yanjun Fang, Yuchuan Shao, Padhraic Mulligan, Jie Qiu, Lei Cao and Jinsong Huang. *Electron-hole diffusion lengths> 175 μm in solution-grown $CH_3NH_3PbI_3$ single crystals*. Science, vol. 347, no. 6225, pages 967–970, 2015. (Cited on pages 3, 9 and 84.)

[Eperon 2014] Giles E Eperon, Samuel D Stranks, Christopher Menelaou, Michael B Johnston, Laura M Herz and Henry J Snaith. *Formamidinium lead trihalide: a broadly tunable perovskite for efficient planar heterojunction solar cells.* Energy & Environmental Science, vol. 7, no. 3, pages 982–988, 2014. (Cited on pages 5, 6, 15, 18 and 96.)

[Eperon 2015] Giles E Eperon, Giuseppe M Paternò, Rebecca J Sutton, Andrea Zampetti, Amir Abbas Haghighirad, Franco Cacialli and Henry J Snaith. *Inorganic caesium lead iodide perovskite solar cells.* Journal of Materials Chemistry A, vol. 3, no. 39, pages 19688–19695, 2015. (Cited on pages 16, 18, 68 and 69.)

[Eperon 2016] Giles E Eperon, Tomas Leijtens, Kevin A Bush, Rohit Prasanna, Thomas Green, Jacob Tse-Wei Wang, David P McMeekin, George Volonakis, Rebecca L Milot, Richard May*et al. Perovskite-perovskite tandem photovoltaics with optimized band gaps.* Science, vol. 354, no. 6314, pages 861–865, 2016. (Cited on pages 21 and 22.)

[Even 2012] Jacky Even, Laurent Pedesseau, M-A Dupertuis, J-M Jancu and Claudine Katan. *Electronic model for self-assembled hybrid organic/perovskite semiconductors: Reverse band edge electronic states ordering and spin-orbit coupling.* Physical Review B, vol. 86, no. 20, page 205301, 2012. (Cited on pages 10 and 26.)

[Even 2013] Jacky Even, Laurent Pedesseau, Jean-Marc Jancu and Claudine Katan. *Importance of spin–orbit coupling in hybrid organic/inorganic perovskites for photovoltaic applications.* The Journal of Physical Chemistry Letters, vol. 4, no. 17, pages 2999–3005, 2013. (Cited on pages 10 and 13.)

[Even 2014a] Jacky Even, Laurent Pedesseau, Jean-Marc Jancu and Claudine Katan. *DFT and k· p modelling of the phase transitions of lead and tin halide perovskites for photovoltaic cells.* physica status solidi (RRL)-Rapid Research Letters, vol. 8, no. 1, pages 31–35, 2014. (Cited on page 12.)

[Even 2014b] Jacky Even, Laurent Pedesseau and Claudine Katan. *Analysis of multivalley and multibandgap absorption and enhancement of free carriers related to exciton screening in hybrid perovskites.* The Journal of Physical Chemistry C, vol. 118, no. 22, pages 11566–11572, 2014. (Cited on pages 8, 10, 12, 14, 15, 61, 63, 64, 74, 78, 94, 95 and 100.)

[Even 2015] Jacky Even, Laurent Pedesseau, Claudine Katan, Mikaël Kepenekian, Jean-Sébastien Lauret, Daniel Sapori and Emmanuelle Deleporte. *Solid-state physics perspective on hybrid perovskite semiconductors.* 2015. (Cited on pages 10, 11, 12, 13 and 52.)

[Fang 2015] Hong-Hua Fang, Raissa Raissa, Mustapha Abdu-Aguye, Sampson Adjokatse, Graeme R Blake, Jacky Even and Maria Antonietta Loi. *Photo-*

physics of organic–inorganic hybrid lead iodide perovskite single crystals. Advanced Functional Materials, vol. 25, no. 16, pages 2378–2385, 2015. (Cited on pages 74 and 100.)

[Frenkel 1931] J Frenkel. *On the transformation of light into heat in solids. I*. Physical Review, vol. 37, no. 1, page 17, 1931. (Cited on page 22.)

[Frings 2008] Paul Frings, Holger Witte, Harry Jones, Jérome Beard and Thomas Hermannsdoerfer. *Rapid cooling methods for pulsed magnets*. IEEE Transactions on Applied Superconductivity, vol. 18, no. 2, pages 612–615, 2008. (Cited on page 31.)

[Galkowski 2016] Krzysztof Galkowski, Anatolie Mitioglu, Atsuhiko Miyata, Paulina Plochocka, Oliver Portugall, Giles E Eperon, Jacob Tse-Wei Wang, Thomas Stergiopoulos, Samuel D Stranks, Henry J Snaith*et al. Determination of the exciton binding energy and effective masses for methylammonium and formamidinium lead tri-halide perovskite semiconductors*. Energy & Environmental Science, vol. 9, no. 3, pages 962–970, 2016. (Cited on pages 53, 60, 61, 74, 75, 78, 93, 99 and 100.)

[Galkowski 2017] K Galkowski, AA Mitioglu, A Surrente, Z Yang, D. K Maude, P Kossacki, GE Eperon, JT-W Wang, HJ Snaith, P Plochocka*et al. Spatially resolved studies of the phases and morphology of methylammonium and formamidinium lead tri-halide perovskites*. Nanoscale, vol. 9, no. 9, pages 3222–3230, 2017. (Cited on pages 9, 70 and 98.)

[Grancini 2015] Giulia Grancini, Ajay Ram Srimath Kandada, Jarvist M Frost, Alex J Barker, Michele De Bastiani, Marina Gandini, Sergio Marras, Guglielmo Lanzani, Aron Walsh and Annamaria Petrozza. *Role of microstructure in the electron–hole interaction of hybrid lead halide perovskites*. Nature photonics, vol. 9, no. 10, pages 695–701, 2015. (Cited on pages 9, 49 and 85.)

[Green 2001] Martin A Green. *Third generation photovoltaics: Ultra-high conversion efficiency at low cost*. Progress in Photovoltaics: Research and Applications, vol. 9, no. 2, pages 123–135, 2001. (Cited on page 20.)

[Hao 2014a] Feng Hao, Constantinos C Stoumpos, Duyen Hanh Cao, Robert PH Chang and Mercouri G Kanatzidis. *Lead-free solid-state organic-inorganic halide perovskite solar cells*. Nature Photonics, vol. 8, no. 6, pages 489–494, 2014. (Cited on page 5.)

[Hao 2014b] Feng Hao, Constantinos C Stoumpos, Robert PH Chang and Mercouri G Kanatzidis. *Anomalous band gap behavior in mixed Sn and Pb perovskites enables broadening of absorption spectrum in solar cells*. Journal of the American Chemical Society, vol. 136, no. 22, pages 8094–8099, 2014. (Cited on page 5.)

[Hayashi 1950] Masakazu Hayashi and Kiichiro Katsuki. *Absorption spectrum of cuprous oxide.* Journal of the Physical Society of Japan, vol. 5, no. 5, pages 380B–381, 1950. (Cited on page 22.)

[Heo 2013] Jin Hyuck Heo, Sang Hyuk Im, Jun Hong Noh, Tarak N Mandal, Choong-Sun Lim, Jeong Ah Chang, Yong Hui Lee, Hi-jung Kim, Arpita Sarkar, Md K Nazeeruddin*et al. Efficient inorganic-organic hybrid heterojunction solar cells containing perovskite compound and polymeric hole conductors.* Nature photonics, vol. 7, no. 6, pages 486–491, 2013. (Cited on pages 74 and 99.)

[Hirasawa 1994] M Hirasawa, T Ishihara, T Goto, K3 Uchida and N Miura. *Magnetoabsorption of the lowest exciton in perovskite-type compound $(CH_3NH_3)PbI_3$.* Physica B: Condensed Matter, vol. 201, pages 427–430, 1994. (Cited on page 61.)

[Hoke 2015] Eric T Hoke, Daniel J Slotcavage, Emma R Dohner, Andrea R Bowring, Hemamala I Karunadasa and Michael D McGehee. *Reversible photo-induced trap formation in mixed-halide hybrid perovskites for photovoltaics.* Chemical Science, vol. 6, no. 1, pages 613–617, 2015. (Cited on pages 3, 4, 21 and 84.)

[Huang 2013] Ling yi Huang and Walter RL Lambrecht. *Electronic band structure, phonons, and exciton binding energies of halide perovskites CsSnCl3, CsSnBr3, and CsSnI3.* Physical Review B, vol. 88, no. 16, page 165203, 2013. (Cited on pages 63 and 94.)

[Huang 2014] Fuzhi Huang, Yasmina Dkhissi, Wenchao Huang, Manda Xiao, Iacopo Benesperi, Sergey Rubanov, Ye Zhu, Xiongfeng Lin, Liangcong Jiang, Yecheng Zhou*et al. Gas-assisted preparation of lead iodide perovskite films consisting of a monolayer of single crystalline grains for high efficiency planar solar cells.* Nano Energy, vol. 10, pages 10–18, 2014. (Cited on pages 4, 9, 41 and 85.)

[Jacobsson 2016] T Jesper Jacobsson, Juan-Pablo Correa-Baena, Meysam Pazoki, Michael Saliba, Kurt Schenk, Michael Grätzel and Anders Hagfeldt. *Exploration of the compositional space for mixed lead halogen perovskites for high efficiency solar cells.* Energy & Environmental Science, vol. 9, no. 5, pages 1706–1724, 2016. (Cited on page 19.)

[Jeon 2015] Nam Joong Jeon, Jun Hong Noh, Woon Seok Yang, Young Chan Kim, Seungchan Ryu, Jangwon Seo and Sang Il Seok. *Compositional engineering of perovskite materials for high-performance solar cells.* Nature, vol. 517, no. 7535, pages 476–480, 2015. (Cited on pages 19 and 20.)

[Jin 2012] Hosub Jin, Jino Im and Arthur J Freeman. *Topological insulator phase in halide perovskite structures.* Physical Review B, vol. 86, no. 12, page 121102, 2012. (Cited on page 4.)

[Johnsson 2007] Mats Johnsson and Peter Lemmens. *Crystallography and chemistry of perovskites*. Handbook of magnetism and advanced magnetic materials, 2007. (Cited on pages 2 and 3.)

[Katan 2015] Claudine Katan, Laurent Pedesseau, Mikaël Kepenekian, Alain Rolland and Jacky Even. *Interplay of spin–orbit coupling and lattice distortion in metal substituted 3D tri-chloride hybrid perovskites*. Journal of Materials Chemistry A, vol. 3, no. 17, pages 9232–9240, 2015. (Cited on pages 4, 13 and 14.)

[Ke 2017] Weijun Ke, Constantinos C Stoumpos, Ioannis Spanopoulos, Lingling Mao, Michelle Chen, Michael R Wasielewski and Mercouri G Kanatzidis. *Efficient Lead-Free Solar Cells Based on Hollow {en} MASnI3 Perovskites*. Journal of the American Chemical Society, vol. 139, no. 41, pages 14800–14806, 2017. (Cited on page 5.)

[Kepenekian 2017] Mikael Kepenekian and Jacky Even. *Rashba and Dresselhaus Couplings in Halide Perovskites: Accomplishments and Opportunities for Spintronics and Spin–Orbitronics*. The Journal of Physical Chemistry Letters, vol. 8, no. 14, pages 3362–3370, 2017. (Cited on pages 14 and 15.)

[Kieslich 2014] Gregor Kieslich, Shijing Sun and Anthony K Cheetham. *Solid-state principles applied to organic–inorganic perovskites: new tricks for an old dog*. Chemical Science, vol. 5, no. 12, pages 4712–4715, 2014. (Cited on page 7.)

[Kim 2016] Jincheol Kim, Jae S Yun, Xiaoming Wen, Arman Mahboubi Soufiani, Cho Fai Jonathan Lau, Benjamin Wilkinson, Jan Seidel, Martin A Green, Shujuan Huang and Anita WY Ho-Baillie. *Nucleation and growth control of HC (NH2) 2PbI3 for planar perovskite solar cell*. The Journal of Physical Chemistry C, vol. 120, no. 20, pages 11262–11267, 2016. (Cited on pages 9 and 85.)

[Knop 1990] Osvald Knop, Roderick E Wasylishen, Mary Anne White, T Stanley Cameron and Michiel JM Van Oort. *Alkylammonium lead halides. Part 2. $CH_3NH_3PbX_3$ (X= Cl, Br, I) perovskites: cuboctahedral halide cages with isotropic cation reorientation*. Canadian Journal of Chemistry, vol. 68, no. 3, pages 412–422, 1990. (Cited on page 7.)

[Kojima 2009] Akihiro Kojima, Kenjiro Teshima, Yasuo Shirai and Tsutomu Miyasaka. *Organometal halide perovskites as visible-light sensitizers for photovoltaic cells*. Journal of the American Chemical Society, vol. 131, no. 17, pages 6050–6051, 2009. (Cited on pages 3 and 84.)

[Korona 1996] KP Korona, A Wysmol/ek, K Pakul/a, R Stepniewski, JM Baranowski, I Grzegory, B L/ucznik, M Wroblewski and S Porowski. *Exciton region reflectance of homoepitaxial GaN layers*. Applied physics letters, vol. 69, no. 6, pages 788–790, 1996. (Cited on page 57.)

[Kulbak 2015] Michael Kulbak, David Cahen and Gary Hodes. *How important is the organic part of lead halide perovskite photovoltaic cells? Efficient CsPbBr3 cells.* The journal of physical chemistry letters, vol. 6, no. 13, pages 2452–2456, 2015. (Cited on pages 18 and 69.)

[Kunugita 2015] Hideyuki Kunugita, Tsubasa Hashimoto, Yuki Kiyota, Yosuke Udagawa, Yuko Takeoka, Yuiga Nakamura, Junro Sano, Tomonori Matsushita, Takashi Kondo, Tsutomu Miyasaka*et al. Excitonic feature in hybrid perovskite $CH_3NH_3PbBr_3$ single crystals.* Chemistry Letters, vol. 44, no. 6, pages 852–854, 2015. (Cited on page 8.)

[Lai 2017] Minliang Lai, Qiao Kong, Connor G Bischak, Yi Yu, Letian Dou, Samuel W Eaton, Naomi S Ginsberg and Peidong Yang. *Structural, optical, and electrical properties of phase-controlled cesium lead iodide nanowires.* Nano Research, vol. 10, no. 4, pages 1107–1114, 2017. (Cited on page 17.)

[Lee 2015] Jin-Wook Lee, Deok-Hwan Kim, Hui-Seon Kim, Seung-Woo Seo, Sung Min Cho and Nam-Gyu Park. *Formamidinium and cesium hybridization for photo-and moisture-stable perovskite solar cell.* Advanced Energy Materials, vol. 5, no. 20, 2015. (Cited on page 21.)

[Leijtens 2015] Tomas Leijtens, Giles E Eperon, Nakita K Noel, Severin N Habisreutinger, Annamaria Petrozza and Henry J Snaith. *Stability of metal halide perovskite solar cells.* Advanced Energy Materials, vol. 5, no. 20, 2015. (Cited on page 18.)

[Li 2015] Zhen Li, Mengjin Yang, Ji-Sang Park, Su-Huai Wei, Joseph J Berry and Kai Zhu. *Stabilizing perovskite structures by tuning tolerance factor: formation of formamidinium and cesium lead iodide solid-state alloys.* Chemistry of Materials, vol. 28, no. 1, pages 284–292, 2015. (Cited on page 18.)

[Li 2016] Dehui Li, Gongming Wang, Hung-Chieh Cheng, Chih-Yen Chen, Hao Wu, Yuan Liu, Yu Huang and Xiangfeng Duan. *Size-dependent phase transition in methylammonium lead iodide perovskite microplate crystals.* Nature communications, vol. 7, 2016. (Cited on pages 7 and 9.)

[Lin 2015] Qianqian Lin, Ardalan Armin, Ravi Chandra Raju Nagiri, Paul L Burn and Paul Meredith. *Electro-optics of perovskite solar cells.* Nature Photonics, vol. 9, no. 2, pages 106–112, 2015. (Cited on page 49.)

[Liu 2013] Mingzhen Liu, Michael B Johnston and Henry J Snaith. *Efficient planar heterojunction perovskite solar cells by vapour deposition.* Nature, vol. 501, no. 7467, pages 395–398, 2013. (Cited on pages 3 and 84.)

[LNCMP-team 2004] The LNCMP-team. *The LNCMP: a pulsed-field user-facility in Toulouse.* Physica B: Condensed Matter, vol. 346 - 347, pages 668 – 672, 2004. Proceedings of the 7th International Symposium on Research in High Magnetic Fields. (Cited on page 33.)

[Ma 2016] Qingshan Ma, Shujuan Huang, Xiaoming Wen, Martin A Green and Anita WY Ho-Baillie. *Hole transport layer free inorganic $CsPbIBr_2$ perovskite solar cell by dual source thermal evaporation.* Advanced Energy Materials, vol. 6, no. 7, 2016. (Cited on page 68.)

[Makado 1986] PC Makado and NC McGill. *Energy levels of a neutral hydrogen-like system in a constant magnetic field of arbitrary strength.* Journal of Physics C: Solid State Physics, vol. 19, no. 6, page 873, 1986. (Cited on pages 27, 60, 61, 74, 92 and 100.)

[McKechnie 2017] Scott McKechnie, Jarvist M Frost, Dimitar Pashov, Pooya Azarhoosh, Aron Walsh and Mark van Schilfgaarde. *Dynamic Symmetry Breaking and Spin Splitting in Metal Halide Perovskites.* arXiv preprint arXiv:1711.00533, 2017. (Cited on page 15.)

[McMeekin 2016] David P McMeekin, Golnaz Sadoughi, Waqaas Rehman, Giles E Eperon, Michael Saliba, Maximilian T Hörantner, Amir Haghighirad, Nobuya Sakai, Lars Korte, Bernd Rech*et al. A mixed-cation lead mixed-halide perovskite absorber for tandem solar cells.* Science, vol. 351, no. 6269, pages 151–155, 2016. (Cited on pages 21, 67 and 85.)

[Megaw 1945] Helen D Megaw. *Crystal structure of barium titanate.* Nature, vol. 155, no. 3938, pages 484–485, 1945. (Cited on pages 1 and 83.)

[Miller 1994] JR Miller, MD Bird, S Bole, A Bonito-Oliva, Y Eyssa, WJ Kenney, TA Painter, H-J Schneider-Muntau, LT Summers, SW Van Sciver*et al. An overview of the 45-T hybrid magnet system for the new National High Magnetic Field Laboratory.* IEEE Transactions on Magnetics, vol. 30, no. 4, pages 1563–1571, 1994. (Cited on page 29.)

[Miyata 2015] Atsuhiko Miyata, Anatolie Mitioglu, Paulina Plochocka, Oliver Portugall, Jacob Tse-Wei Wang, Samuel D Stranks, Henry J Snaith and Robin J Nicholas. *Direct measurement of the exciton binding energy and effective masses for charge carriers in organic-inorganic tri-halide perovskites.* Nature Physics, vol. 11, no. 7, pages 582–587, 2015. (Cited on pages 8, 49, 57, 60, 64, 74, 75, 95, 99 and 100.)

[Motta 2015] Carlo Motta, Fedwa El-Mellouhi, Sabre Kais, Nouar Tabet, Fahhad Alharbi and Stefano Sanvito. *Revealing the role of organic cations in hybrid halide perovskite $CH_3NH_3PbI_3$.* Nature communications, vol. 6, page 7026, 2015. (Cited on page 7.)

[Nayak 2016] Pabitra K Nayak, David T Moore, Bernard Wenger, Simantini Nayak, Amir A Haghighirad, Adam Fineberg, Nakita K Noel, Obadiah G Reid, Garry Rumbles, Philipp Kukura*et al. Mechanism for rapid growth of organic–inorganic halide perovskite crystals.* Nature communications, vol. 7, page 13303, 2016. (Cited on page 56.)

[Niesner 2016] Daniel Niesner, Max Wilhelm, Ievgen Levchuk, Andres Osvet, Shreetu Shrestha, Miroslaw Batentschuk, Christoph Brabec and Thomas Fauster. *Giant Rashba Splitting in CH_3NH_3 $PbBr_3$ Organic-Inorganic Perovskite.* Physical review letters, vol. 117, no. 12, page 126401, 2016. (Cited on page 15.)

[Niezgoda 2017] J Scott Niezgoda, Benjamin J Foley, Alexander Z Chen and Joshua J Choi. *Improved Charge Collection in Highly Efficient $CsPbBrI_2$ Solar Cells with Light-Induced Dealloying.* ACS Energy Letters, vol. 2, no. 5, pages 1043–1049, 2017. (Cited on page 68.)

[Noel 2014] Nakita K Noel, Samuel D Stranks, Antonio Abate, Christian Wehrenfennig, Simone Guarnera, Amir-Abbas Haghighirad, Aditya Sadhanala, Giles E Eperon, Sandeep K Pathak, Michael B Johnston*et al.* *Lead-free organic–inorganic tin halide perovskites for photovoltaic applications.* Energy & Environmental Science, vol. 7, no. 9, pages 3061–3068, 2014. (Cited on page 5.)

[Noh 2013] Jun Hong Noh, Sang Hyuk Im, Jin Hyuck Heo, Tarak N Mandal and Sang Il Seok. *Chemical management for colorful, efficient, and stable inorganic–organic hybrid nanostructured solar cells.* Nano letters, vol. 13, no. 4, pages 1764–1769, 2013. (Cited on page 4.)

[Oku 2015] Takeo Oku. *Crystal structures of $CH_3NH_3PbI_3$ and related perovskite compounds used for solar cells.* In Solar Cells-New Approaches and Reviews. InTech, 2015. (Cited on page 7.)

[Onoda-Yamamuro 1992] Noriko Onoda-Yamamuro, Takasuke Matsuo and Hiroshi Suga. *Dielectric study of CH3NH3PbX3 (X= Cl, Br, I).* Journal of Physics and Chemistry of Solids, vol. 53, no. 7, pages 935–939, 1992. (Cited on page 8.)

[Papavassiliou 1994] George C Papavassiliou, IB Koutselas, A Terzis and M-H Whangbo. *Structural and electronic properties of the natural quantum-well system $(C_6H_5CH_2CH_2NH_3)_2SnI_4$.* Solid state communications, vol. 91, no. 9, pages 695–698, 1994. (Cited on page 13.)

[Pelant 2012] Ivan Pelant and Jan Valenta. Luminescence spectroscopy of semiconductors. Oxford University Press, 2012. (Cited on pages 23 and 24.)

[Pellet 2014] Norman Pellet, Peng Gao, Giuliano Gregori, Tae-Youl Yang, Mohammad K Nazeeruddin, Joachim Maier and Michael Grätzel. *Mixed-organic-cation Perovskite photovoltaics for enhanced solar-light harvesting.* Angewandte Chemie International Edition, vol. 53, no. 12, pages 3151–3157, 2014. (Cited on pages 6 and 20.)

[Pérez-Osorio 2015] Miguel A Pérez-Osorio, Rebecca L Milot, Marina R Filip, Jay B Patel, Laura M Herz, Michael B Johnston and Feliciano Giustino. *Vibrational properties of the organic–inorganic halide perovskite $CH_3NH_3PbI_3$ from theory and experiment: Factor group analysis, first-principles calculations, and low-temperature infrared spectra.* The Journal of Physical Chemistry C, vol. 119, no. 46, pages 25703–25718, 2015. (Cited on pages 76 and 102.)

[Philippe 2015] Bertrand Philippe, Byung-Wook Park, Rebecka Lindblad, Johan Oscarsson, Sareh Ahmadi, Erik MJ Johansson and Hakan Rensmo. *Chemical and Electronic Structure Characterization of Lead Halide Perovskites and Stability Behavior under Different Exposures A Photoelectron Spectroscopy Investigation.* Chemistry of Materials, vol. 27, no. 5, pages 1720–1731, 2015. (Cited on page 15.)

[Phuong 2016] Le Quang Phuong, Yumi Nakaike, Atsushi Wakamiya and Yoshihiko Kanemitsu. *Free Excitons and Exciton–Phonon Coupling in $CH_3NH_3PbI_3$ Single Crystals Revealed by Photocurrent and Photoluminescence Measurements at Low Temperatures.* The journal of physical chemistry letters, vol. 7, no. 23, pages 4905–4910, 2016. (Cited on page 57.)

[Poglitsch 1987] Albrecht Poglitsch and Daniel Weber. *Dynamic disorder in methylammoniumtrihalogenoplumbates (II) observed by millimeter-wave spectroscopy.* The Journal of chemical physics, vol. 87, no. 11, pages 6373–6378, 1987. (Cited on pages 8, 64, 78 and 95.)

[Quarti 2013] Claudio Quarti, Giulia Grancini, Edoardo Mosconi, Paola Bruno, James M Ball, Michael M Lee, Henry J Snaith, Annamaria Petrozza and Filippo De Angelis. *The Raman spectrum of the $CH_3NH_3PbI_3$ hybrid perovskite: interplay of theory and experiment.* The journal of physical chemistry letters, vol. 5, no. 2, pages 279–284, 2013. (Cited on page 61.)

[Sachdev 2006] Subir Sachdev. *Handbook of magnetism and advanced magnetic materials.* 2006. (Cited on page 3.)

[Sakata 1979] Makoto Sakata, Takashi Nishiwaki and Jimpei Harada. *Neutron diffraction study of the structure of cubic $CsPbBr_3$.* Journal of the Physical Society of Japan, vol. 47, no. 1, pages 232–233, 1979. (Cited on page 68.)

[Saliba 2016a] Michael Saliba, Taisuke Matsui, Konrad Domanski, Ji-Youn Seo, Amita Ummadisingu, Shaik M Zakeeruddin, Juan-Pablo Correa-Baena, Wolfgang R Tress, Antonio Abate, Anders Hagfeldt*et al.* *Incorporation of rubidium cations into perovskite solar cells improves photovoltaic performance.* Science, vol. 354, no. 6309, pages 206–209, 2016. (Cited on pages 20, 67 and 85.)

[Saliba 2016b] Michael Saliba, Taisuke Matsui, Ji-Youn Seo, Konrad Domanski, Juan-Pablo Correa-Baena, Mohammad Khaja Nazeeruddin, Shaik M Zakeeruddin, Wolfgang Tress, Antonio Abate, Anders Hagfeldt*et al.* *Cesium-containing triple cation perovskite solar cells: improved stability, reproducibility and high efficiency.* Energy & Environmental Science, vol. 9, no. 6, pages 1989–1997, 2016. (Cited on pages 20, 49, 67 and 85.)

[Schreiber 1982] Michael Schreiber and Yutaka Toyozawa. *Numerical Experiments on the Absorption Lineshape of the Exciton under Lattice Vibrations. I. The Overall Lineshape.* Journal of the Physical Society of Japan, vol. 51, no. 5, pages 1528–1536, 1982. (Cited on page 63.)

[Sendner 2016] Michael Sendner, Pabitra K Nayak, David A Egger, Sebastian Beck, Christian Müller, Bernd Epding, Wolfgang Kowalsky, Leeor Kronik, Henry J Snaith, Annemarie Pucci*et al.* *Optical phonons in methylammonium lead halide perovskites and implications for charge transport.* Materials Horizons, vol. 3, no. 6, pages 613–620, 2016. (Cited on pages 76 and 102.)

[Shah 1999] Arvind Shah, Pedro Torres, Reto Tscharner, Nicolas Wyrsch and Herbert Keppner. *Photovoltaic technology: the case for thin-film solar cells.* science, vol. 285, no. 5428, pages 692–698, 1999. (Cited on pages 16 and 21.)

[Shi 2015] Dong Shi, Valerio Adinolfi, Riccardo Comin, Mingjian Yuan, Erkki Alarousu, Andrei Buin, Yin Chen, Sjoerd Hoogland, Alexander Rothenberger, Khabiboulakh Katsiev*et al.* *Low trap-state density and long carrier diffusion in organolead trihalide perovskite single crystals.* Science, vol. 347, no. 6221, pages 519–522, 2015. (Cited on page 9.)

[Shkrob 2014] Ilya A Shkrob and Timothy W Marin. *Charge trapping in photovoltaically active perovskites and related halogenoplumbate compounds.* The journal of physical chemistry letters, vol. 5, no. 7, pages 1066–1071, 2014. (Cited on page 15.)

[Shockley 1961] William Shockley and Hans J Queisser. *Detailed balance limit of efficiency of p-n junction solar cells.* Journal of applied physics, vol. 32, no. 3, pages 510–519, 1961. (Cited on page 20.)

[Singh 2016] Shivam Singh, Cheng Li, Fabian Panzer, K. L. Narasimhan, Anna Graeser, Tanaji P. Gujar, Anna Kohler, Mukundan Thelakkat, Sven Huettner and Dinesh Kabra. *Effect of Thermal and Structural Disorder on the Electronic Structure of Hybrid Perovskite Semiconductor $CH_3NH_3PbI_3$.* The Journal of Physical Chemistry Letters, vol. 7, no. 15, pages 3014–3021, 2016. (Cited on pages 63 and 94.)

[Sivaram 2015] Varun Sivaram, Samuel D Stranks and Henry J Snaith. *Outshining silicon.* Scientific American, vol. 313, no. 1, pages 54–59, 2015. (Cited on pages 20 and 21.)

[Soufiani 2017] Arman Mahboubi Soufiani, Zhuo Yang, Trevor Young, Atsuhiko Miyata, Alessandro Surrente, Alexander Pascoe, Krzysztof Galkowski, Mojtaba Abdi-Jalebi, Roberto Brenes, Joanna Urban*et al.* *Impact of microstructure on the electron–hole interaction in lead halide perovskites.* Energy & Environmental Science, vol. 10, no. 6, pages 1358–1366, 2017. (Cited on page 49.)

[Stoumpos 2013a] Constantinos C Stoumpos, Christos D Malliakas and Mercouri G Kanatzidis. *Semiconducting tin and lead iodide perovskites with organic cations: phase transitions, high mobilities, and near-infrared photoluminescent properties.* Inorganic chemistry, vol. 52, no. 15, pages 9019–9038, 2013. (Cited on pages 70 and 98.)

[Stoumpos 2013b] Constantinos C Stoumpos, Christos D Malliakas, John A Peters, Zhifu Liu, Maria Sebastian, Jino Im, Thomas C Chasapis, Arief C Wibowo, Duck Young Chung, Arthur J Freeman*et al.* *Crystal growth of the perovskite semiconductor CsPbBr3: a new material for high-energy radiation detection.* Crystal Growth & Design, vol. 13, no. 7, pages 2722–2727, 2013. (Cited on page 69.)

[Stranks 2013] Samuel D Stranks, Giles E Eperon, Giulia Grancini, Christopher Menelaou, Marcelo JP Alcocer, Tomas Leijtens, Laura M Herz, Annamaria Petrozza and Henry J Snaith. *Electron-hole diffusion lengths exceeding 1 micrometer in an organometal trihalide perovskite absorber.* Science, vol. 342, no. 6156, pages 341–344, 2013. (Cited on pages 3, 15 and 84.)

[Suarez 2014] Belen Suarez, Victoria Gonzalez-Pedro, Teresa S Ripolles, Rafael S Sanchez, Luis Otero and Ivan Mora-Sero. *Recombination study of combined halides (Cl, Br, I) perovskite solar cells.* The journal of physical chemistry letters, vol. 5, no. 10, pages 1628–1635, 2014. (Cited on pages 3, 5 and 84.)

[Swarnkar 2016] Abhishek Swarnkar, Ashley R Marshall, Erin M Sanehira, Boris D Chernomordik, David T Moore, Jeffrey A Christians, Tamoghna Chakrabarti and Joseph M Luther. *Quantum dot–induced phase stabilization of α-$CsPbI_3$ perovskite for high-efficiency photovoltaics.* Science, vol. 354, no. 6308, pages 92–95, 2016. (Cited on pages 17 and 18.)

[Tamura 1986] Hiroshi Tamura, Djuniadi A Sagala and Kikuo Wakino. *Lattice vibrations of $Ba(Zn_{1/3}Ta_{2/3})O_3$ crystal with ordered perovskite structure.* Japanese journal of applied physics, vol. 25, no. 6R, page 787, 1986. (Cited on pages 2 and 83.)

[Tanaka 2003a] Kenichiro Tanaka and Takashi Kondo. *Bandgap and exciton binding energies in lead-iodide-based natural quantum-well crystals.* Science and Technology of Advanced Materials, vol. 4, no. 6, pages 599–604, 2003. (Cited on page 61.)

[Tanaka 2003b] Kenichiro Tanaka, Takayuki Takahashi, Takuma Ban, Takashi Kondo, Kazuhito Uchida and Noboru Miura. *Comparative study on the excitons in lead-halide-based perovskite-type crystals CH 3 NH 3 PbBr 3 CH 3 NH 3 PbI 3.* Solid state communications, vol. 127, no. 9, pages 619–623, 2003. (Cited on pages 61 and 93.)

[Tilchin 2016] Jenya Tilchin, Dmitry N Dirin, Georgy I Maikov, Aldona Sashchiuk, Maksym V Kovalenko and Efrat Lifshitz. *Hydrogen-like Wannier–Mott Excitons in Single Crystal of Methylammonium Lead Bromide Perovskite.* ACS nano, vol. 10, no. 6, pages 6363–6371, 2016. (Cited on page 60.)

[Umari 2014] Paolo Umari, Edoardo Mosconi and Filippo De Angelis. *Relativistic GW calculations on $CH_3NH_3PbI_3$ and $CH_3NH_3SnI_3$ perovskites for solar cell applications.* Scientific reports, vol. 4, page 4467, 2014. (Cited on page 61.)

[Varshni 1967] Yatendra Pal Varshni. *Temperature dependence of the energy gap in semiconductors.* physica, vol. 34, no. 1, pages 149–154, 1967. (Cited on pages 14, 63 and 94.)

[Vorpahl 2015] Sarah M Vorpahl, Samuel D Stranks, Hirokazu Nagaoka, Giles E Eperon, Mark E Ziffer, Henry J Snaith, David S Ginger*et al. Impact of microstructure on local carrier lifetime in perovskite solar cells.* Science, page aaa5333, 2015. (Cited on pages 9, 10 and 68.)

[Waleed 2017] Aashir Waleed, Mohammad Mahdi Tavakoli, Leilei Gu, Shabeeb Hussain, Daquan Zhang, Swapnadeep Poddar, Ziyi Wang, Rongjun Zhang and Zhiyong Fan. *All Inorganic Cesium Lead Iodide Perovskite Nanowires with Stabilized Cubic Phase at Room Temperature and Nanowire Array-based Photodetectors.* Nano letters, vol. 17, no. 8, pages 4951–4957, 2017. (Cited on page 17.)

[Wang 2016] Dian Wang, Matthew Wright, Naveen Kumar Elumalai and Ashraf Uddin. *Stability of perovskite solar cells.* Solar Energy Materials and Solar Cells, vol. 147, pages 255–275, 2016. (Cited on page 15.)

[Wehrenfennig 2014] Christian Wehrenfennig, Mingzhen Liu, Henry J Snaith, Michael B Johnston and Laura M Herz. *Charge carrier recombination channels in the low-temperature phase of organic-inorganic lead halide perovskite thin films.* APL Materials, vol. 2, no. 8, page 081513, 2014. (Cited on pages 9 and 61.)

[Wenk 2016] Hans-Rudolf Wenk and Andrey Bulakh. Minerals: their constitution and origin. Cambridge University Press, 2016. (Cited on pages 1 and 83.)

[Whitfield 2016] PS Whitfield, N Herron, WE Guise, K Page, YQ Cheng, I Milas and MK Crawford. *Structures, Phase Transitions and Tricritical Behavior of the Hybrid Perovskite Methyl Ammonium Lead Iodide.* Scientific reports, vol. 6, page 35685, 2016. (Cited on pages 7 and 10.)

[Wu 1987] Maw-Kuen Wu, Jo R Ashburn, CJ Torng, Ph H Hor, Rl L Meng, Lo Gao, Z Jo Huang, YQ Wang and CW Chu. *Superconductivity at 93 K in a new mixed-phase Y-Ba-Cu-O compound system at ambient pressure.* Physical Review Letters, vol. 58, no. 9, page 908, 1987. (Cited on pages 1 and 83.)

[Wu 2014] Kewei Wu, Ashok Bera, Chun Ma, Yuanmin Du, Yang Yang, Liang Li and Tom Wu. *Temperature-dependent excitonic photoluminescence of hybrid organometal halide perovskite films.* Physical Chemistry Chemical Physics, vol. 16, no. 41, pages 22476–22481, 2014. (Cited on pages 63 and 94.)

[Xiao 2014] Zhengguo Xiao, Qingfeng Dong, Cheng Bi, Yuchuan Shao, Yongbo Yuan and Jinsong Huang. *Solvent annealing of perovskite-induced crystal growth for photovoltaic-device efficiency enhancement.* Advanced Materials, vol. 26, no. 37, pages 6503–6509, 2014. (Cited on page 9.)

[Xing 2014] Guichuan Xing, Nripan Mathews, Swee Sien Lim, Natalia Yantara, Xinfeng Liu, Dharani Sabba, Michael Grätzel, Subodh Mhaisalkar and Tze Chien Sum. *Low-temperature solution-processed wavelength-tunable perovskites for lasing.* Nature materials, vol. 13, no. 5, pages 476–480, 2014. (Cited on pages 3 and 84.)

[Yamada 2015] Yasuhiro Yamada, Toru Nakamura, Masaru Endo, Atsushi Wakamiya and Yoshihiko Kanemitsu. *Photoelectronic Responses in Solution-Processed Perovskite $CH_3NH_3PbI_3$ Solar Cells Studied by Photoluminescence and Photoabsorption Spectroscopy.* IEEE Journal of Photovoltaics, vol. 5, no. 1, pages 401–405, 2015. (Cited on pages 8, 63 and 94.)

[Yang 2015a] Jinli Yang, Braden D Siempelkamp, Dianyi Liu and Timothy L Kelly. *Investigation of $CH_3NH_3PbI_3$ degradation rates and mechanisms in controlled humidity environments using in situ techniques.* ACS nano, vol. 9, no. 2, pages 1955–1963, 2015. (Cited on page 84.)

[Yang 2015b] Woon Seok Yang, Jun Hong Noh, Nam Joong Jeon, Young Chan Kim, Seungchan Ryu, Jangwon Seo and Sang Il Seok. *High-performance photovoltaic perovskite layers fabricated through intramolecular exchange.* Science, vol. 348, no. 6240, pages 1234–1237, 2015. (Cited on page 3.)

[Yang 2017a] Woon Seok Yang, Byung-Wook Park, Eui Hyuk Jung, Nam Joong Jeon, Young Chan Kim, Dong Uk Lee, Seong Sik Shin, Jangwon Seo, Eun Kyu Kim, Jun Hong Noh*et al. Iodide management in formamidinium-lead-halide–based perovskite layers for efficient solar cells.* Science, vol. 356, no. 6345, pages 1376–1379, 2017. (Cited on page 20.)

[Yang 2017b] Zhuo Yang, Alessandro Surrente, Krzysztof Galkowski, Nicolas Bruyant, Duncan K Maude, Amir Abbas Haghighirad, Henry J Snaith, Paulina Plochocka and Robin J Nicholas. *Unraveling the exciton binding*

energy and the dielectric constant in single crystal methylammonium lead triiodide perovskite. arXiv preprint arXiv:1701.05081, 2017. (Cited on page 78.)

[Zhao 2017] Baodan Zhao, Mojtaba Abdi-Jalebi, Maxim Tabachnyk, Hugh Glass, Varun S Kamboj, Wanyi Nie, Andrew J Pearson, Yuttapoom Puttisong, Karl C Gödel, Harvey E Beere*et al. High Open-Circuit Voltages in Tin-Rich Low-Bandgap Perovskite-Based Planar Heterojunction Photovoltaics.* Advanced Materials, vol. 29, no. 2, 2017. (Cited on pages 3, 5 and 84.)